

**COMPUTER SIMULATION OF GTL  
AND VARIOUS PROBLEMS IN THERMODYNAMICS**

A Dissertation

by

XIAONIAN WANG

Submitted to the Office of Graduate Studies of  
Texas A&M University  
in partial fulfillment of the requirements for the degree of

DOCTOR OF PHILOSOPHY

May 2004

Major Subject: Chemical Engineering

**COMPUTER SIMULATION OF GTL  
AND VARIOUS PROBLEMS IN THERMODYNAMICS**

A Dissertation

by

XIAONIAN WANG

Submitted to Texas A&M University  
in partial fulfillment of the requirements  
for the degree of

DOCTOR OF PHILOSOPHY

Approved as to style and content by:

---

Philip T. Eubank  
(Chair of Committee)

---

Kenneth R. Hall  
(Member)

---

David M. Ford  
(Member)

---

Maria A. Barrufet  
(Member)

---

Kenneth R. Hall  
(Head of Department)

May 2004

Major Subject: Chemical Engineering

## ABSTRACT

Computer Simulation of GTL and Various Problems in Thermodynamics.

(May 2004)

Xiaonian Wang, B.S., Zhejiang University, Hangzhou, China

Chair of Advisory Committee: Dr. Philip T. Eubank

This dissertation intends to provide new tuning techniques for several simple cubic equations of state (EOS) to improve their accuracy in calculating fluid phase equilibrium. It also provides graphical tools to predict some phase equilibrium phenomena from activity coefficient models. Finally, it presents simulation results for a new gas-to-liquids process.

Saturation Properties for Fluids: By deriving a new identity linking the heat of vaporization for pure components to the EOS, we are able to find new expressions for the two constants  $a$  &  $b$  in the EOS. These new expressions then allow tuning of both constants  $a$  and  $b$  to experimental saturation properties at subcritical temperatures. These new tuning procedures prove effective to the point where the simpler Redlich-Kwong EOS provides better results with our procedure than does the usually superior Peng-Robinson EOS with conventional procedures.

Activity Coefficient Models: This dissertation shows the flexibility of four activity coefficient models in the prediction of three fluid phase equilibrium phenomena. From these models we successfully developed new graphs that allow one to identify the

presence of any of the three phenomena by visual inspection without performing a complex calculation as seen in current texts.

Remote Natural Gas: This dissertation presents simulation results of a new gas-to-liquids process which converts natural gas to liquid transportation fuels.

Based on the assumption of adiabatic reactions, our simulation results show that methane conversion increases with higher reaction temperature and longer residence times. Hydrogen can both inhibit methane decomposition and reduce coke formation. The rich components in the natural gas are found to decompose very fast and they have a vast quenching effect on the whole reactions. Recycling of unreacted methane also increases overall methane conversion. Finally, our simulator provides very close prediction of the experimental results from a pilot plant. Thus, we conclude that the simulation work is basically successful in fulfilling the goal of this research.

*To my parents,  
my wife,  
and my beloved son, Eric*

## ACKNOWLEDGMENTS

I would like to thank my committee chair and advisor, Dr. Philip T. Eubank for his guidance, patience and encouragement during the course of this research. I wish to express my deep gratitude to him for sharing his knowledge and experience both academically and socially during the years of my study here at Texas A&M University.

I would also like to thank Drs. Kenneth R. Hall, David M. Ford and Maria A. Barrufet for serving on my committee and providing great support and input to my research.

I also want to express my gratitude to Synfuels International, Inc. for providing valuable pilot plant experimental data to test the validity of my simulator developed for the simulation of the remote natural gas conversion process.

My thanks also goes to all the staff at the Department of Chemical Engineering for their excellent support during my study and research at this university.

Finally, I sincerely thank all my friends who have provided me with so much help to make this work possible.

## TABLE OF CONTENTS

	Page
ABSTRACT .....	iii
ACKNOWLEDGMENTS .....	vi
TABLE OF CONTENTS .....	vii
LIST OF FIGURES .....	ix
LIST OF TABLES .....	xiii
CHAPTER	
I INTRODUCTION .....	1
II SATURATION PROPERTIES FROM EQUATIONS OF STATE.....	14
Derivation of a New Identity .....	14
Tuning of EOS Constants to Saturation Properties.....	16
Tuning Simple Cubic EOS to the Vapor Pressure and Heat of Vaporization .....	18
An Example of Tuning to Different Saturation Properties .....	22
The <i>Volume</i> Problem.....	32
Inclusion of $a'$ and $b'$ Terms .....	32
III CHARACTERISTICS OF ACTIVITY COEFFICIENT MODELS FOR LIQUID SOLUTIONS.....	37
Homogeneous Azeotropes at Low Pressures.....	37
Symmetric Solution Model.....	38
Margules (two-constant) Model.....	42
Extrema and Inflection Points.....	42
Liquid-liquid Phase Splitting .....	46
Homogeneous Azeotropes .....	49
Van Laar Model .....	52
Extrema and Inflection Points.....	53
Liquid-liquid Phase Splitting .....	55
Homogeneous Azeotropes .....	57
NRTL Model.....	58
Extrema and Inflection Points.....	58
Liquid-liquid Phase Splitting .....	60
Homogeneous Azeotropes .....	63

CHAPTER	Page
IV PYROLYSIS OF NATURAL GAS: REVIEW AND METHODOLOGY FOR KINETIC SIMULATION .....	64
Current Technologies of Converting Natural Gas to Liquids .....	64
Direct Conversion .....	65
Partial Oxidation to Methanol .....	66
Oxidative Coupling to Ethylene .....	67
Oxyhydrochlorination .....	67
Indirect Conversion of Methane .....	68
Steam Reforming .....	68
Autothermal Reforming .....	70
Catalytic Partial Oxidation (CPO) .....	71
High-temperature Pyrolysis .....	74
Methodology for Kinetic Simulation .....	76
V KINETIC SIMULATION OF NATURAL GAS PYROLYSIS UNDER ADIABATIC CONDITIONS .....	86
Pure Methane Feed .....	86
Effect of Hydrogen Dilution .....	99
Rich Gas Feed .....	105
Pure Methane Feed with a Combustion Zone .....	111
Effect of Methane Recycling .....	116
Simulation of Experimental Data from a Pilot Plant .....	121
Simulation of Experimental Data from a Pilot Plant – Trying One New Reaction .....	129
VI CONCLUSIONS AND RECOMMENDATIONS FOR FUTURE RESEARCH .....	134
LITERATURE CITED .....	141
VITA .....	147



## LIST OF FIGURES

FIGURE	Page
I.1 The world's natural gas consumption, 1970-2025.....	10
III.1 Graph of $\ln\gamma_1$ and of $\ln\gamma_2$ vs $x_1$ showing the mirror-image symmetry about $x_1 = 0.5$ for the symmetric solution model.....	39
III.2 Schematic diagram of parameter $A$ vs temperature $T$ in one-constant Margules Model.....	41
III.3a Graph of $\ln\gamma_1$ and of $\ln\gamma_2$ vs $x_1$ for the Margules model with $A_{12} = 1.8$ and $A_{21} = 0.6$ .....	44
III.3b Insert of region of Fig. III.3a.....	45
III.4 Margules (two-constant) locus lines for extrema and inflection points on $\ln\gamma_i$ vs $x_1$ graphs with $A_{12} > A_{21}$ .....	45
III.5 Curve of function $g$ vs $x_1$ by Margules two-constant model: (a) $A_{12} = 3.5$ and $A_{21} = -1$ which show an immiscibility gap bound by the two tangent points and outside the two inflection points; (b) $A_{12} = 2.1$ , $A_{21} = 1$ which does not show any inflection point thus no phase splitting.....	48
III.6 Margules (two-constant) locus lines for liquid-liquid phase splitting with $A_{12} > A_{21}$ .....	49
III.7 Margules (two-constants) regions for the formation of single and double azeotropes with $A_{12} > A_{21}$ .....	51
III.8 van Laar locus lines for inflection points on $\ln\gamma_i$ vs $x_1$ graphs with $\alpha > \beta$ .....	54
III.9 van Laar locus for liquid-liquid phase splitting with $\alpha > \beta$ .....	56
III.10 van Laar regions for the formation of single, homogeneous azeotropes with $\alpha > \beta$ .....	57
III.11a NRTL locus for liquid-liquid phase splitting with $\tau_{12} > 0$ and $\tau_{21} < 0$ .....	62
III.11b NRTL locus for liquid-liquid phase splitting with $\tau_{12} > 0$ and $\tau_{21} > 0$ .....	63

FIGURE	Page
IV.1 Block diagram for conventional steam reforming: CH <sub>4</sub> and excess H <sub>2</sub> O are reacted in a primary reformer over Ni/Al <sub>2</sub> O <sub>3</sub> at 900 °C .....	69
IV.2 Schematic representation of autothermal reforming: CH <sub>4</sub> is reacted with O <sub>2</sub> in a flame and the products of homogeneous partial oxidation are then reformed by H <sub>2</sub> O in the feed over a Ni catalyst bed .....	70
IV.3 Flow scheme for natural gas-based low temperature Fischer – Tropsch process..	74
IV.4 Standard free energy of formation ( $\Delta G_f^\circ$ ) of some hydrocarbons as function of temperature (K).....	80
IV.5 Schematic diagram to show the reference substance and energy changes for energy balance calculation .....	83
IV.6 Block diagram of the reaction system used in the current simulation work.....	85
V.1a Amount of components in the product gas stream at various inlet temperatures. Resident time = 1 ms. $n_{\text{CH}_4}^0 = 1 \text{ mol}$ , P = 1atm .....	89
V.1b Amount of components in the product gas stream at various inlet temperatures. Resident time = 2 ms. $n_{\text{CH}_4}^0 = 1 \text{ mol}$ , P = 1atm .....	89
V.1c Amount of components in the product gas stream at various inlet temperatures. Resident time = 4 ms. $n_{\text{CH}_4}^0 = 1 \text{ mol}$ , P = 1atm .....	90
V.1d Amount of components in the product gas stream at various inlet temperatures. Resident time = 6 ms. $n_{\text{CH}_4}^0 = 1 \text{ mol}$ , P = 1atm .....	90
V.1e Amount of components in the product gas stream at various inlet temperatures. Resident time = 8 ms. $n_{\text{CH}_4}^0 = 1 \text{ mol}$ , P = 1atm .....	91
V.1f Amount of components in the product gas stream at various inlet temperatures. Resident time = 12 ms. $n_{\text{CH}_4}^0 = 1 \text{ mol}$ , P = 1atm .....	91
V.1g Amount of components in the product gas stream at various inlet temperatures. Resident time = 16 ms. $n_{\text{CH}_4}^0 = 1 \text{ mol}$ , P = 1atm .....	92
V.1h Amount of components in the product gas stream at various inlet temperatures. Resident time = 20 ms. $n_{\text{CH}_4}^0 = 1 \text{ mol}$ , P = 1atm .....	92

FIGURE	Page
V.2a Conversion of methane versus temperature at various residence times. $n_{\text{CH}_4}^0 = 1 \text{ mol}, P = 1 \text{ atm}$ .....	93
V.2b Conversion of methane versus residence times at selected inlet temperatures. $n_{\text{CH}_4}^0 = 1 \text{ mol}, P = 1 \text{ atm}$ .....	93
V.3a Amount of three main products at various inlet temperatures. Resident time = 1 ms. $n_{\text{CH}_4}^0 = 1 \text{ mol}, P = 1 \text{ atm}$ .....	94
V.3b Amount of three main products at various inlet temperature. Resident time = 4 ms. $n_{\text{CH}_4}^0 = 1 \text{ mol}, P = 1 \text{ atm}$ .....	94
V.3c Amount of three main products at various inlet temperature. Resident time = 8 ms. $n_{\text{CH}_4}^0 = 1 \text{ mol}, P = 1 \text{ atm}$ .....	95
V.3d Amount of three main products at various inlet temperatures. Resident time = 12 ms. $n_{\text{CH}_4}^0 = 1 \text{ mol}, P = 1 \text{ atm}$ .....	95
V.3e Amount of three main products at various inlet temperatures. Resident time = 20 ms. $n_{\text{CH}_4}^0 = 1 \text{ mol}, P = 1 \text{ atm}$ .....	96
V.4a Yield of three main products versus residence times at $T_{\text{in}} = 1600 \text{ K}$ . $n_{\text{CH}_4}^0 = 1 \text{ mol}, P = 1 \text{ atm}$ .....	96
V.4b Yield of three main products versus residence times at $T_{\text{in}} = 1800 \text{ K}$ . $n_{\text{CH}_4}^0 = 1 \text{ mol}, P = 1 \text{ atm}$ .....	97
V.4c Yield of three main products versus residence times at $T_{\text{in}} = 2000 \text{ K}$ . $n_{\text{CH}_4}^0 = 1 \text{ mol}, P = 1 \text{ atm}$ .....	97
V.5a Outlet temperature profile of the thermal cracker versus residence times at various inlet temperatures. $t = 0 \sim 1 \text{ ms}$ .....	98
V.5b Outlet temperature profile of the thermal cracker versus residence times at various inlet temperatures. $t = 1 \sim 20 \text{ ms}$ .....	98
V.6a Amount of components in the product gas stream at various inlet temperatures. Residence time = 1 ms. $\text{CH}_4:\text{H}_2 = 1 \text{ mol} : 1 \text{ mol}, P = 1 \text{ atm}$ .....	101

FIGURE	Page
V.6b Amount of components in the product gas stream at various inlet temperatures. Residence time = 4 ms. CH <sub>4</sub> :H <sub>2</sub> = 1 mol : 1 mol, P = 1 atm.....	102
V.6c Amount of components in the product gas stream at various inlet temperatures. Residence time = 8 ms. CH <sub>4</sub> :H <sub>2</sub> = 1 mol : 1 mol, P = 1 atm.....	102
V.7a Comparison of methane conversion at various inlet temperatures. Residence time = 1 ms. CH <sub>4</sub> :H <sub>2</sub> = 1 mol : 1 mol for the mixture feed case, P = 1 atm.....	103
V.7b Comparison of methane conversion at various inlet temperatures. Residence time = 4 ms. CH <sub>4</sub> :H <sub>2</sub> = 1 mol : 1 mol for the mixture feed case, P = 1 atm.....	103
V.8a Comparison of carbon formation at various inlet temperatures. Resident time = 1 ms. CH <sub>4</sub> :H <sub>2</sub> = 1 mol : 1 mol for the mixture feed case, P = 1 atm.....	104
V.8b Comparison of carbon formation at various inlet temperatures. Resident time = 4 ms. CH <sub>4</sub> :H <sub>2</sub> = 1 mol : 1 mol for the mixture feed case, P = 1 atm.....	104
V.9a Amount of components in the product gas stream at various inlet temperatures. Residence time = 4 ms. P = 1 atm.....	109
V.9b Amount of components in the product gas stream at various inlet temperatures. Residence time = 8 ms. P = 1 atm.....	109
V.10a Conversion of methane at various inlet temperatures. Residence time = 4 ms. P = 1 atm.....	110
V.10b Conversion of methane at various inlet temperatures. Residence time = 8 ms. P = 1 atm.....	110
V.11a Amount of components in the product gas stream at various inlet temperatures. Residence time = 4 ms. P = 1 atm, reflux ratio R = 1.....	119
V.11b Amount of components in the product gas stream at various inlet temperatures. Residence time = 4 ms. P = 1 atm, reflux ratio R = 2.....	119
V.11c Amount of components in the product gas stream at various inlet temperatures. Residence time = 4 ms. P = 1 atm, reflux ratio R = 3.....	120
V.12 Methane conversion versus temperature at various reflux ratios (t = 4 ms). The two dashed lines (R = 0 and R = ∞) are boundaries of the conversion curves ....	120
V.13 Schematic diagram of reaction system for simulation of the pilot plant data.....	121

## LIST OF TABLES

TABLE	Page
I.1	Various Thermophysical Properties Consistent with the Various Cubic Equations of State .....5
I.2	World Natural Gas Reserves by Country (Top 12) as of January 1, 2003 .....13
I.3	Typical Constituents of Natural Gas.....13
II.1	Results for Methanol and for Benzene Using the R-K/EOS.....26
II.2	Results for Methanol and for Benzene Using the R-K/EOS with Eqs. II.15c/d/e together with Estimated Values of the Experimental Saturation Volumes.....31
II.3	Results for Methanol and for Benzene Using the R-K/EOS with Inclusion of the <i>a'</i> and <i>b'</i> Terms for the Heat of Vaporization.....36
V.1	Excess Heat of Combustion of CH <sub>4</sub> and H <sub>2</sub> at Selected Initial and Final Temperatures.....112
V.2	Sensible Heat Required to Heat One Mole of Natural Gas (Lean or Rich) from Selected Initial and Final Temperatures.....113
V.3	Amount of H <sub>2</sub> or CH <sub>4</sub> Fuel Required to Heat One Mole of Natural Gas (Lean or Rich) from Selected Initial and Final Temperatures .....113
V.4	Results of Natural Gas Pyrolysis with Energy Provided from A Burner .....115
V.5	Compositions of Feedstock and Product Gas Streams of a Pilot Run .....122
V.6	Compositions of Process Streams Based on 1 mol Rich Gas Feed .....123
V.7	Results of Simulating Pilot Plant Data (Residence time = 4 ms) .....129
V.8	Comparison of Compositions of Inlet and Outlet Process Streams to the Cracker .....130
V.9	Results of Simulating Pilot Plant Data – One New Reaction Added (Residence time = 4 ms) .....132

# CHAPTER I

## INTRODUCTION

Vapor-liquid, liquid-liquid and vapor-liquid-liquid mixtures represent three important categories of phase equilibria. The calculation of these equilibria has very important application both in scientific research work and in industrial production. Generally speaking, there are two methods to calculate the above phase equilibria, i.e. the  $\Phi - \Phi$  method using Equation of States (EOS) of the mixture and the  $\gamma - \Phi$  method using the activity coefficient models (Smith et al., 2001; Sandler, 1999).

The  $\Phi - \Phi$  method is good for phase equilibria calculation only when an equation of state is available to describe each phase of the mixture. This often requires the mixture to have low nonideality. Indeed, for relatively simple mixtures such as those of hydrocarbons or hydrocarbons with inorganic gases, simple cubic equations of state with the van der Waals one-fluid mixing rules are applicable at all densities and temperatures. Thus the fugacity coefficients and fugacities can be easily calculated using formulas provided in current thermodynamic textbooks, leading to relatively straightforward approach for phase equilibria calculation.

However, highly nonideal solution mixtures such as those containing polar organic chemicals can not be described by any equation of state currently available. They are often described by the excess Gibbs free energy or activity coefficient models. As the parameters in these models are very temperature-dependent, these models are not applicable to expanded liquids (liquids at very high temperatures) or to the vapor phase.

Furthermore, it is very difficult to define a hypothetical standard state and the standard state properties for a component that exists as a gas in the pure component state at the temperature and pressure of the mixture, especially if the component is above its critical temperature. Also the absence of a valid gas-phase model for polar organic compounds has resulted in difficulties in describing the vapor-liquid equilibrium of polar mixtures at high temperatures and pressures, and for describing supercritical extraction processes.

From the above analysis it is obviously seen that equations of states and activity coefficient models both have their respective grounds in the calculation of fluid phase equilibria. Thus, studies and deep understanding of every bit of the nature of these two types of models are necessary for their better and proper application to a certain mixture. In the following we will focus on the studies of how the saturation properties – such as saturation vapor pressure and volumes combining with heat of vaporization – can be used to tune the constants in several equations of states (Eubank and Wang, 2003) so that these EOS are more accurate in describing the systems of interest. We will use the pure component EOS for a simpler treatment. The study can then be extended to the EOS for mixtures together with appropriate mixing rules. Latter, we will study the characteristics of several typical activity coefficient models for liquid solutions and try to find easier ways of using these models. Our new mathematical methods will lead to new graphs (Eubank and Wang, 2003) which allow the reader to identify phenomena such as phase splitting and homogeneous azeotropes, etc. without performing detailed calculations such as a Gibbs energy minimization for liquid phase splitting.

Saturation Properties for Fluids: For pure components, the Maxwell Equal-Area-Rule (MEAR) is a well-known thermodynamic identity for vapor-liquid equilibria (VLE):

$$P^\sigma (V_V^\sigma - V_L^\sigma) = \int_{V_L^\sigma}^{V_V^\sigma} P^{\text{EOS}}(dV)_T \quad (\text{I.1})$$

Eq. I.1 provides universal vapor pressure curves in reduced coordinates for simple cubic equations of state (EOS) such as those of van der Waals and of Redlich-Kwong and further for the Soave-Redlich-Kwong and Peng-Robinson EOS for fixed acentric factors  $\omega$  when, in all cases, the two constants  $a$  &  $b$  are set by the critical point constraints (Barrufet and Eubank, 1989), which require the following two conditions to hold for isotherms at critical points:

$$\left( \frac{\partial P}{\partial V} \right)_{T^c}^{\text{CP}} \equiv 0 \quad \text{and} \quad \left( \frac{\partial^2 P}{\partial V^2} \right)_{T^c}^{\text{CP}} \equiv 0 \quad (\text{I.2})$$

We summarize the results from these four cubic EOS below where the values of the two constants  $a$  &  $b$  are given for pure components from the critical isotherm constraints as shown in Eq. I.2.

I. van der Waals (vdW) (1873):  $P = \frac{RT}{V-b} - \frac{a}{V^2}$

$$a = \frac{27R^2 T_c^2}{64P^c}; \quad b = \frac{RT_c}{8P^c}$$

II. Redlich-Kwong (R-K) (1949):  $P = \frac{RT}{V-b} - \frac{a}{\sqrt{T}V(V+b)}$

$$a = \frac{0.4274R^2 T_c^{2.5}}{P^c}; \quad b = \frac{0.08664RT_c}{P^c}$$

III. Soave's modification of R-K equation (SRK) (1972):  $P = \frac{RT}{V-b} - \frac{a}{V(V+b)}$

$$a = \frac{0.4274R^2 T_c^2 s^2}{P^c}; \quad b = \frac{0.08664RT_c}{P^c}; \quad s = 1 - (1 - \sqrt{T_r})f_s; \quad T_r \equiv T/T_c;$$



$$f_s \equiv 0.480 + 1.574\omega - 0.176\omega^2; \quad \omega \equiv \text{Pitzer's acentric factor} \equiv -1 - \log_{10} P_r^\sigma \Big|_{T_r=0.7}$$

$$\text{IV. Peng-Robinson (P-R) (1976): } P = \frac{RT}{V-b} - \frac{a}{V^2 + 2bV - b^2}$$

$$a = \frac{0.45724R^2 T_c^2 t^2}{P^c}; \quad b = \frac{0.07780RT_c}{P^c}; \quad t \equiv (1 - \sqrt{T_r})f_t; \quad T_r \equiv T/T_c;$$

$$f_t \equiv 0.37464 + 1.54226\omega - 0.2699\omega^2;$$

$$\omega \equiv \text{Pitzer's acentric factor} \equiv -1 - \log_{10} P_r^\sigma \Big|_{T_r=0.7}$$

Additional relations for various properties from these cubic EOS are given in Table I.1, where  $Z^c \equiv P^c V^c / RT^c$  is the critical compressibility factor,  $\psi^c$  is the Riedel factor defined as  $(T^c/P^c)(\partial P/\partial T)_V^{CP}$  with the slope of the critical isochore at the critical point  $((\partial P/\partial T)_V^{CP})$  being identical to the vapor pressure slope at the same point,  $B(T)$  is the second virial coefficient in the density expansion,  $C(T)$  is the third virial coefficient in the density expansion,  $(P^c B^c / RT^c)$  is the reduced second virial coefficient at the critical temperature (which is  $-0.34 \pm 0.01$  for all compounds measured),  $(\partial^2 P/\partial T^2)_V^\sigma \Big|_{\text{liq}}$  is the second derivative of liquid isochors as they emerge from the vapor pressure curve on a  $P \sim T$  diagram (positive from experiment) and, similarly,  $(\partial^2 P/\partial T^2)_V^\sigma \Big|_{\text{vap}}$  is the second derivative of vapor isochors (negative from experiment).

**Table I.1 Various Thermophysical Properties Consistent with the Various Cubic Equations of State**

Properties of EOS	vdW	R-K	S-R-K	P-R
$P^c$	$a/27b^2$	$\left[ (0.08664/b)^5 (a/0.42747)^2 \right]^{1/3}$	$0.017563a/b^2$	$0.013238a/b^2$
$T^c$	$8a/27bR$	$(0.20268a/bR)^{2/3}$	$0.20271a/bR$	$0.17015a/bR$
$V^c$	$3b$	$3.847b$	$3.847b$	$3.9512b$
$Z^c$	$3/8$	$1/3$	$1/3$	$0.30740$
$\psi^c$	$4$	$5.5804$	$5.4822$ ( $\omega = 0$ )	$5.6229$ ( $\omega = 0$ )
$B(T)$	$b - a/RT$	$b - a/RT^{3/2}$	$b - a/RT$	$b - a/RT$
$C(T)$	$b^2$	$b^2 + ab/RT^{3/2}$	$b^2 + ab/RT$	$b^2 + 2ab/RT$
$V^c/b$	$3$	$3.847$	$3.847$	$3.9512$
$-[P^c B^c / RT^c]$	$0.2969$	$0.3408$	$0.3408$	$0.3749$
$\left( \partial^2 P / \partial T^2 \right)_V^{\sigma} \Big _{\text{liq}}$	$0$	$< 0$	$< 0$	$< 0$
$\left( \partial^2 P / \partial T^2 \right)_V^{\sigma} \Big _{\text{vap}}$	$0$	$< 0$	$< 0$	$< 0$

Conversely, in commercial practice, Eq. I.1 allows for the attraction constant  $a$  to be tuned to experimental vapor pressures when these EOS are used with only the repulsion constant  $b$  taken from the critical point constraints. The EOS is often cubic in the volume  $V$  but must be pressure explicit or  $P^{\text{EOS}}(T, V)$  in order to capture both the saturated liquid volume  $V_L^{\sigma}$  as well as the saturated vapor volume  $V_V^{\sigma}$ . Mathematical poles in the EOS written in the pressure explicit form can be eliminated by multiplication of the entire equation by the product of the various denominators revealing the true cubic nature of the equation (Deiters, 2002).

Activity Coefficient Models: Liquid-phase activity coefficient ( $\gamma_i$ ) models (or excess Gibbs energy models,  $G^E/RT$ ) with three or less adjustable parameters, dependent upon temperature  $T$ , are often sufficient to model the phase equilibria calculations of the vapor-liquid mixtures or vapor-liquid-liquid mixtures (Gmehling and Onken, 1990). These models provide us with the flexibility to correlate experimental data and to predict: 1) extremum and inflection points on the popular  $\ln \gamma_i$  vs  $x_1$  diagram for binary solutions, 2) liquid-liquid phase splitting for binary solutions, and 3) homogeneous azeotropes for low pressures where the gas phase can be approximately assumed to be in perfect state. Four such models are investigated here: (a) the symmetric solution model (Porter's model or one-constant Margules model), (b) the two-constant Margules model, (c) the van Laar model, and (d) the three-constant Non-Random-Two-Liquid (NRTL) model (Smith et al., 2001; Sandler, 1999). First we will present the well known properties for the symmetric solution model with only one constant, then we introduce new mathematical approaches to derive some new equations and graphs which allow the easy identification of the above three phenomena for the two-constant Margules and van Laar models and the three-constant NRTL model. The graphical results are invaluable as they prove to be very convenient to use in determining say whether a liquid-liquid phase splitting exists for a given set of Margules, van Laar or NRTL constants without the need to perform complex and time-consuming calculations according to the original equations.

The above models must be used together with the Gibbs-Duhem equation. In terms of the activity coefficients ( $\gamma_i$ ), the liquid-phase Gibbs-Duhem identity for a binary system can be expressed as below:

$$x_1 d\ln\gamma_1 + x_2 d\ln\gamma_2 = [V^E/RT]dP - [H^E/RT^2]dT \quad (I.3)$$

where  $V^E$  and  $H^E$  are the excess volume and enthalpy, respectively, for the liquid solution. According to the Gibbs phase rule

$$F = C - P + 2 - C.C. - R - S \quad (I.4)$$

where  $F$  is the degree of freedom,  $C$  is the number of chemical components,  $P$  is the number of coexisting phases at equilibrium,  $C.C.$  is the number of critical point constraints,  $R$  is the number of independent chemical reactions and  $S$  is the number of special stoichiometric constraints. Assume a binary solution with  $C.C. = R = S = 0$ , the phase rule becomes  $F = C - P + 2 = 4 - P$ . Then for a single-phase liquid solution, three independent variables ( $x_1$ ,  $T$ ,  $P$ ) are required to fix the state. If we hold the temperature and pressure to be constant and vary only  $x_1$  then the Gibbs-Duhem equation I.3 will lead to

$$x_1(\partial \ln \gamma_1 / \partial x_1)_{P,T} = -x_2(\partial \ln \gamma_2 / \partial x_1)_{P,T} \quad (I.5)$$

This equation requires that the graphs of  $\ln \gamma_1$  and  $\ln \gamma_2$  to have opposite signs for their slopes. Any reasonable ( $G^E/RT$ ) model of uniform continuity and zero at the pure end points obeys Eq. I.5 at constant temperature and pressure --- for a single liquid phase because  $\ln \gamma_i = \bar{G}_i^E/RT$ . The *constants* in the model are truly constant here as  $T$  &  $P$  are fixed.

Most often, liquid activity coefficients are measured by total pressure experiment which uses the modified Raoult's Law as below:

$$\gamma_i = y_i P / (x_i P_i^\sigma) \quad (I.6)$$

In such a vapor-liquid equilibrium experiment the system has a freedom of  $F = C - P + 2 = 2$ , thus there are only two intensive variables to be independent. We can either

isothermally vary the total pressure and  $x_1$  or isobarically vary the temperature and  $x_1$ . When the experiment is conducted at constant temperature, the graphs of  $\ln\gamma_1$  and of  $\ln\gamma_2$  vs  $x_1$  (or of  $G^E/RT$  vs  $x_1$ ) are not for constant pressure and the Gibbs-Duhem identity of Eq.I.3 becomes

$$x_1(\partial\ln\gamma_1/\partial x_1)_T = -x_2(\partial\ln\gamma_2/\partial x_1)_T + [V^E/RT](\partial P/\partial x_1)_T \quad (I.7)$$

In the graph of  $V^E$  vs  $x_1$  the excess liquid volume is zero at the two end points of pure components but can change sign in between, and the slope of the bubble-point curve  $(\partial P/\partial x_1)$  can also switch sign if an azeotrope is present in the middle of the phase diagram, then the last term in Eq. I.7 can be either positive, zero or negative. Thus the two slopes of the activity coefficients  $(\partial\ln\gamma_i/\partial x_i)$  can be of the same sign, but not necessarily be of opposite signs as people normally think. This phenomenon is occasionally observed in experimental data, independent of any activity coefficient model, as discussed recently in detail (Eubank et al., 2000). Thus a problem arises when we try to fit the activity coefficients measured from the total pressure experiment with a model equation (e.g., Margules two-constant equation) because the measured activity coefficients actually vary with the total pressure while people normally think that the constants in those activity coefficient models are only functions of temperature. Eq. I.7 leaves us with its final term being zero which is only true at the pure end points and at azeotrope points, if they exist. This problem can be solved if we assume the model constants to be dependent on both temperature and pressure. When the data are isobaric, the problem is the same but more widely recognized as it is commonly assumed that the model constants vary with temperature.

In this dissertation we adhere to the notion of a single liquid solution allowing for Eq. I.5. However, it should be noted that additional problems will arise when these models are applied to data from a vapor-liquid equilibrium experiment.

Remote Natural Gas: In the past century the world has been relying heavily on petroleum as its primary source of energy supply. However, the oil crisis in the 1970's showed the world some potential threats of relying too heavily on petroleum as the major source of energy supply. Natural gas, with its abundance and global reserves, fell into people's horizon as a potential substitute for petroleum to meeting the world's energy needs.

The growth rate of natural gas consumption in the past decade has topped those for petroleum and coal both worldwide and in the United States, and this trend appears to be advancing into the future. From 1987 through 1996, natural gas consumption grew 25% worldwide and 27% in the United States. According to the *International Energy Outlook 2003 (IEO2003)*,(www.doe.gov), natural gas is expected to be the fastest growing component of world primary energy consumption in the next two decades. Consumption of natural gas worldwide is projected to increase by an average of 2.8 percent annually from 2001 to 2025, compared with projected annual growth rates of 1.8 percent for oil consumption and 1.5 percent for coal. Natural gas consumption in 2025, at 176 trillion cubic feet, is projected to be nearly double the 2001 total of 90 trillion cubic feet as seen in Figure I.1. The natural gas share of total energy consumption is projected to increase from 23 percent in 2001 to 28 percent in 2025 (IEO2003).

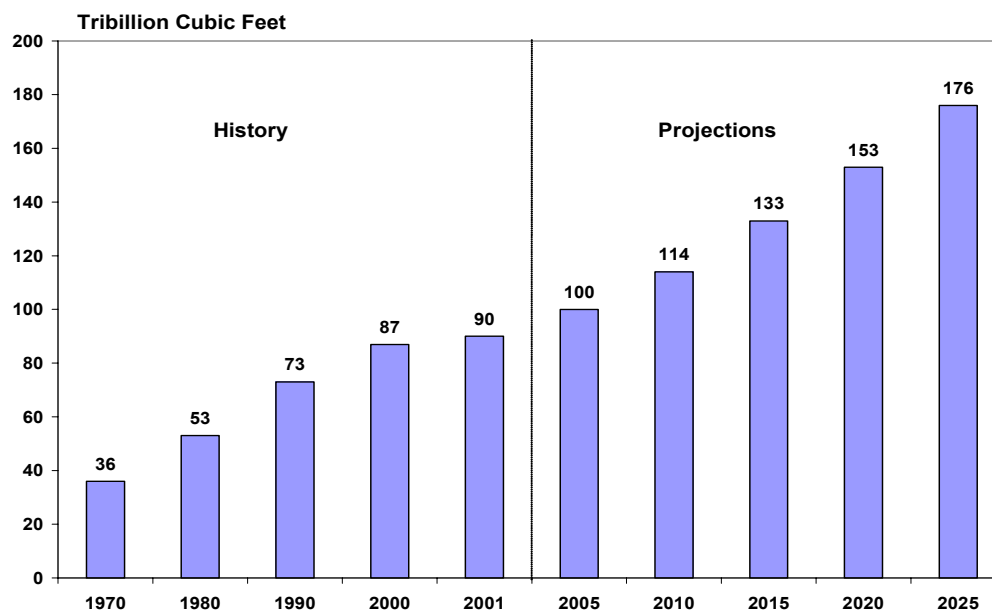


**Figure I.1. The world's natural gas consumption, 1970-2025. Sources: [www.eia.doe.gov](http://www.eia.doe.gov)**

The U.S. consumes over 25% the total world natural gas consumption ([www.altenergy.org](http://www.altenergy.org)). The natural gas supplies about 23% of the primary energy consumption and its demand is expected to rise by 1.8% annually in this country. These figures show that natural gas is playing a more and more important role as a major source of primary energy for the country.

There are several primary reasons that make natural gas a favorite source of energy supply. First of all, the world's proven gas reserve has been increasing steadily. Second, natural gas reserves are widely spread over many countries, including Russia, the Middle East, the US and some Asian countries as shown in Table I.2. This ensures that supply of natural gas can not be controlled by some few countries as is the case of petroleum. Third, the prices of natural gas have been kept steadily low ever since,

compared with the sharp fluctuation of the price of petroleum. Finally, natural gas is an environmentally good choice of fuel. In comparison with electricity-utilizing homes, natural-gas-utilizing homes release 99% less sulphur dioxide, 95% less particulate matter and 40~50% less carbon monoxide.

So what is natural gas? Natural gas is simply a colorless, odorless naturally occurring mixture of combustible hydrocarbon gases and impurities. Its major component is methane ( $\text{CH}_4$ ). Other than this, natural gas also contains two types of non-hydrocarbon impurities – one type is diluents such as nitrogen, carbon dioxide, water vapor, and the other type is contaminants such as  $\text{H}_2\text{S}$  and other sulfur compounds. Typical composition of natural gas components is shown in Table I.3.

The diluent components consume horse power and pipelining capacity during transport, and the contaminant gases are detrimental to production and transport equipment. Therefore both types of impurities need to be removed from the natural gas before the gas is supplied to end users. Gas coming out of a reservoir must first be separated with the entrained liquids (free water, well inhibitors, lube oil, scrubber oil, heavier-end hydrocarbons, etc.) and solid matter (“pipeline trash”, such as sand, pipe scale, and dirt), then dehydrated to remove water vapor, and then desulfurized to remove  $\text{H}_2\text{S}$  (sweetening process). After these pretreatments, natural gas will mainly contain methane, with small amounts of other hydrocarbons and impurities going through the transportation and storage systems before reaching the end customers (Kumar, 1987; Arnold and Stewart, 1999).

As a major source of energy, natural gas has a lot of advantages compared with petroleum and coal. However, the benefits of increased consumption of natural gas does



not come without a price. A lot of the world's natural gas reserves are in remote areas which are not accessible by current pipeline networks (Kennedy, 1993). Also, many remote oil wells produce natural gases which are not of sufficient capacity to warrant commercial production. Industrial figures show that approximately 15.5 trillion cubic feet of stranded natural gas – equivalent to 1.5 billion barrels of fuel – is flared directly to the air every year ([www.synfuels.com](http://www.synfuels.com)). In 1996 20% of total CO<sub>2</sub> emissions from fossil fuels came from consuming and flaring natural gas. Natural gas emissions increased 26.9% from 1987 to 1996, with the U.S. and Russia accounting for a whopping 42% of the world total (Collins, 2003). In order to solve these problems, it is urgent to develop technologies which can be used to convert remote natural gas to liquid fuels for convenient and economic transportation to end customers.

**Table I.2. World Natural Gas Reserves by Country (Top 12) as of January 1, 2003.**  
**Source: *International Energy Outlook 2003***

Country	Reserves (Trillion Cubic Feet)	Percent of World Total
World	5,501	100.0
Russia	1,680	30.5
Iran	812	14.8
Qatar	509	9.2
Saudi Arabia	224	4.1
United Arab Emirates	212	3.9
United States	183	3.3
Algeria	160	2.9
Venezuela	148	2.7
Nigeria	124	2.3
Iraq	110	2.0
Indonesia	93	1.7
Australia	90	1.6

**Table I.3. Typical Constituents of Natural Gas (Kumar, 1987)**

Category	Component	Amounts, %
Paraffinic HC's	CH <sub>4</sub>	70 – 98%
	C <sub>2</sub> H <sub>6</sub>	1 – 10%
	C <sub>3</sub> H <sub>8</sub>	Trace – 5%
	C <sub>4</sub> H <sub>10</sub>	Trace – 2%
	C <sub>5</sub> H <sub>12</sub>	Trace – 1%
	C <sub>6</sub> H <sub>14</sub>	Trace – 0.5%
	C <sub>7</sub> +	None – trace
Cyclic HC's	C <sub>3</sub> H <sub>6</sub> (Cyclopropane)	Traces
	C <sub>6</sub> H <sub>12</sub> (Cyclohexane)	Traces
Aromatic HC's	C <sub>6</sub> H <sub>6</sub>	Traces
Non-hydrocarbon	N <sub>2</sub>	Trace – 15%
	CO <sub>2</sub>	Trace – 1%
	H <sub>2</sub> S	Trace occasionally
	He	Trace – 5%
	Other sulfur and nitrogen compounds	Trace occasionally
	H <sub>2</sub> O	Trace – 5%

## CHAPTER II

### SATURATION PROPERTIES FROM EQUATIONS OF STATE

#### Derivation of a New Identity

Differentiation of MEAR (Eq. I.1) with respect to temperature (T) with use of Leibnitz's rule for derivatives of integrals with variable limits provides

$$\begin{aligned} & P^\sigma \left[ \left( \frac{dV_V^\sigma}{dT} \right) - \left( \frac{dV_L^\sigma}{dT} \right) \right] + (V_V^\sigma - V_L^\sigma) \left( \frac{dP^\sigma}{dT} \right) \\ &= P^\sigma \left( \frac{dV_V^\sigma}{dT} \right) - P^\sigma \left( \frac{dV_L^\sigma}{dT} \right) + \int_{V_L^\sigma}^{V_V^\sigma} \left( \frac{\partial P^{\text{EOS}}}{\partial T} \right)_V (dV)_T . \end{aligned}$$

A cancellation of terms of the form  $P^\sigma \left[ \left( \frac{dV_V^\sigma}{dT} \right) - \left( \frac{dV_L^\sigma}{dT} \right) \right]$  yields

$$\left( \frac{dP^\sigma}{dT} \right) (V_V^\sigma - V_L^\sigma) = \int_{V_L^\sigma}^{V_V^\sigma} \left( \frac{\partial P^{\text{EOS}}}{\partial T} \right)_V (dV)_T . \quad (\text{II.1})$$

Further, application of the Clapeyron identity,

$$\left( \frac{dP^\sigma}{dT} \right) (V_V^\sigma - V_L^\sigma) = \lambda / T \quad (\text{II.2})$$

provides an interesting, new identity

$$\lambda = T \int_{V_L^\sigma}^{V_V^\sigma} \left( \frac{\partial P^{\text{EOS}}}{\partial T} \right)_V (dV)_T , \quad (\text{II.3})$$

where  $\lambda$  is the heat of vaporization, a measurable quantity from calorimetry. While the new identity, Eq. II.3, has been derived by differentiation of Eq. I.1 together with use of Eq. II.2, it is mathematically independent of each of these equations. The integrand of Eq. II.3 is the isochoric slope predicted by the EOS. Eq. II.3 is very different from equations for the heat of vaporization used by Adachi & Sugie (1987a & b) which do not use either

MEAR nor the Clapeyron equation, fail to eliminate the vapor pressure itself from the integral and contain two terms rather than one on the right-hand side of the equation.

For the van der Waals EOS, if we assume that the two constants  $a$  and  $b$  are temperature-independent, then the isochoric slope is

$$\left(\frac{\partial P^{\text{EOS}}}{\partial T}\right)_V = \frac{R}{V-b}. \quad (\text{II.4})$$

Substituting the above expression into Eq. II.3 for integration to provide

$$\frac{\lambda}{RT} = \ln\left(\frac{V_V^\sigma - b}{V_L^\sigma - b}\right) \quad (\text{II.5})$$

Similarly, for Redlich-Kwong EOS we assume that constants  $a$  and  $b$  are temperature-independent, and the isochoric slope is

$$\left(\frac{\partial P^{\text{EOS}}}{\partial T}\right)_V = \frac{R}{V-b} + \frac{a}{2V(V+b)T^{3/2}} \quad (\text{II.6})$$

Substitution of Eq. II.6 into Eq. II.3 and integrate it to provide

$$\frac{\lambda}{RT} = \ln\left(\frac{V_V^\sigma - b}{V_L^\sigma - b}\right) - \left(\frac{a}{2bRT^{3/2}}\right) \ln\left[\frac{V_L^\sigma(V_V^\sigma + b)}{V_V^\sigma(V_L^\sigma + b)}\right]. \quad (\text{II.7})$$

Because both the Soave-Redlich-Kwong and the Peng-Robinson EOS have  $a$ -parameter with temperature dependence, their equations for  $\lambda$  are somewhat more complicated but can be easily derived. For Soave-Redlich-Kwong the isochoric slope is

$$\left(\frac{\partial P^{\text{EOS}}}{\partial T}\right)_V = \frac{R}{V-b} + \frac{0.4274R^2 T^c s f_s}{P^c \sqrt{T_r} V(V+b)} \quad (\text{II.8})$$

so the heat of vaporization is

$$\frac{\lambda}{RT} = \ln\left(\frac{V_V^\sigma - b}{V_L^\sigma - b}\right) - \left(\frac{0.4274RT^c s f_s}{bP^c \sqrt{T_r}}\right) \ln\left[\frac{V_L^\sigma(V_V^\sigma + b)}{V_V^\sigma(V_L^\sigma + b)}\right]. \quad (\text{II.9})$$

Likewise, for Peng-Robinson, the isochoric slope is

$$\left(\frac{\partial P^{\text{EOS}}}{\partial T}\right)_V = \frac{R}{V-b} + \frac{0.45724R^2 T^c t f_t}{P^c \sqrt{T_r} (V^2 + 2bV - b^2)} \quad (\text{II.10})$$

and the heat of vaporization is

$$\frac{\lambda}{RT} = \ln\left(\frac{V_V^\sigma - b}{V_L^\sigma - b}\right) + \left(\frac{0.16166RT^c t f_t}{bP^c \sqrt{T_r}}\right) \ln\left[\frac{(V_V^\sigma - 0.41421b)(V_L^\sigma + 2.41421b)}{(V_L^\sigma - 0.41421b)(V_V^\sigma + 2.41421b)}\right]. \quad (\text{II.11})$$

All of the above results assume that  $a$  &  $b$  are independent of temperature except for Eqs. II.9 & II.11 which assume that  $a$  varies with temperature by a set equation for subcritical temperatures and then  $a$  equals the value from the critical constraints for temperatures that are critical or higher.

### Tuning of EOS Constants to Saturation Properties

As indicated in the S-R-K and P-R equations of state, the two constants  $a$  and  $b$  are functions of temperature. To tune these constants to the saturation properties, we first disregard the temperature dependencies associated with these two EOS through the  $s$  and  $t$  terms, respectively. Later improvements of these generalized correction, such as that of Stryjek & Vera (1986) for the P-R equation and, more recently, Hernandez-Garduza et al. (2002) for the same EOS, are also not used here as our objective is to tune directly onto the experimental database of vapor pressure  $P^\sigma$ , saturated liquid volume  $V_L^\sigma$ , saturated vapor volume  $V_V^\sigma$  and heat of vaporization  $\lambda$  for a specific compound while maintaining their interrelation through the Clapeyron identity. With only two parameters  $a(T)$  and  $b(T)$  available from these simple cubic EOS and with the Clapeyron equation reducing  $P^\sigma(T)$ ,

$V_L^\sigma(T)$ ,  $V_V^\sigma(T)$  and  $\lambda$  to three properties, we obviously have a choice in which properties are deemed most important in our application of the EOS simulator.

Many thermodynamists have had negative experiences when tuning the repulsive parameter  $b(T)$  to saturation properties such as liquid volumes. For example, Salim & Trebble (1991) found such tuning of their EOS caused negative isobaric heat capacities at high pressures in the compressed liquid. While disturbing, these pressures are far above critical and have no bearing upon the present saturation properties for phase equilibria simulators. Care has been taken here to preserve thermodynamic consistency of the saturation properties through the Clapeyron equation so all the results below are consistent in the two-phase region.

The tools for the tuning here are Eq. I.1 for the vapor pressure, Eq. II.3 for the heat of vaporization, and direct tuning of the EOS for the saturation volumes. The latter can be achieved by either direct use of experimental saturation volumes or by use of simplified equations such as the Rackett equation for computing the saturated liquid volume and a virial-type equation for computing the saturated vapor volume. For saturated liquid volumes  $V_L^\sigma$ , the equation of Rackett (1970) is

$$V_L^\sigma = (RT^c/P^c) Z_c^{1+(1-T_r)^{2.7}} \quad (\text{II.12})$$

where the experimental values of the critical temperature and critical pressure apply but the critical compressibility factor should be consistent with the EOS used as given in Table I.1. This usually causes a distortion of all the values of  $V_L^\sigma$  compared to experimental results.

For densities approaching one-half of the critical density (or volumes above twice the critical volume), the Leiden expansion truncated after the third virial coefficient

generally provides saturated vapor volumes accurate to about 1% for reduced temperatures below 0.95 for simple molecules like methane (Setzmann & Wagner, 1991) whereas this accuracy is only achieved below  $T_r = 0.86$  (Kruggel-Emden, 2002) for steam. The Leiden expansion to be used here is

$$P^\sigma V_v^\sigma / RT = 1 + B/V_v^\sigma + C/(V_v^\sigma)^2 \quad (\text{II.13})$$

where  $B(T)$  and  $C(T)$  are the second and third virial coefficients ( Dymond et al., 1980). Given the temperature and vapor pressure, the cubic Eq. II.13 can be solved numerically for  $V_v^\sigma$ .

### **Tuning Simple Cubic EOS to the Vapor Pressure and Heat of Vaporization**

In the design of distillation towers for the separation of mixtures it is important to have the computer simulation forecast the correct vapor pressure and heat of vaporization of the pure components. The first property is important for the phase equilibrium calculations and the second property is important for estimation of the energy requirements, which involve mixture heats of vaporization (Vuddagiri & Eubank, 1998). As is usually the case for mixtures, these mixture heats of vaporization start with accurate values for the constituent pure components. It is also well understood that the saturated liquid and vapor volumes are only used in tray design and tray spacing for distillation towers and thus high accuracy is not necessary.

Following the previous section, we tune the various cubic EOS given here onto the experimental vapor pressures and heats of vaporization using Eqs. I.1 & II.3. In application of Eq. II.3 we again ignore the variation of constants  $a$  and  $b$  with temperature.

For van der Waals equation of state, we have derived Eq. II.5 from Eq. I.1 & II.3.

Let

$$\eta = \frac{\lambda}{RT} = \ln\left(\frac{V_V^\sigma - b}{V_L^\sigma - b}\right) \quad (\text{II.14a})$$

Solving this equation we get the expression of  $b$ :

$$b = \frac{V_V^\sigma - V_L^\sigma e^\eta}{1 - e^\eta}. \quad (\text{II.14b})$$

Apply the vdW/EOS to Eq. I.1 for integration:

$$\begin{aligned} P^\sigma (V_V^\sigma - V_L^\sigma) &= \int_{V_L^\sigma}^{V_V^\sigma} P^{\text{EOS}} (dV)_T \\ &= \int_{V_L^\sigma}^{V_V^\sigma} \left( \frac{RT}{V-b} - \frac{a}{V^2} \right) (dV)_T \\ &= RT \ln\left(\frac{V_V^\sigma - b}{V_L^\sigma - b}\right) + a \left( \frac{1}{V_V^\sigma} - \frac{1}{V_L^\sigma} \right) \end{aligned} \quad (\text{II.14c})$$

Substituting it into Eq. II.14a and let  $\Delta V^\sigma = V_V^\sigma - V_L^\sigma$  in the above equation, after simplification we get

$$a = \left( \frac{\lambda}{\Delta V^\sigma} - P^\sigma \right) V_V^\sigma V_L^\sigma. \quad (\text{II.14d})$$

For Redlich-Kwong EOS, the procedures for deriving the expressions of  $a$  and  $b$  are similar but a bit more complicated. First, by rearranging Eq. II.7 we get

$$\lambda = RT \ln\left(\frac{V_V^\sigma - b}{V_L^\sigma - b}\right) + \frac{a}{2b\sqrt{T}} \ln\left[\frac{V_V^\sigma (V_L^\sigma + b)}{V_L^\sigma (V_V^\sigma + b)}\right]. \quad (\text{II.15a})$$

Second, substituting the R-K/EOS into Eq. I.1 and integrate it to get



$$\begin{aligned}
P^\sigma (V_V^\sigma - V_L^\sigma) &= \int_{V_L^\sigma}^{V_V^\sigma} P^{\text{EOS}}(dV)_T \\
&= RT \ln \left( \frac{V_V^\sigma - b}{V_L^\sigma - b} \right) - \frac{a}{b\sqrt{T}} \ln \left[ \frac{V_V^\sigma (V_L^\sigma + b)}{V_L^\sigma (V_V^\sigma + b)} \right].
\end{aligned} \tag{II.15b}$$

By solving the above two equations jointly we get the following results:

$$b = \frac{V_V^\sigma - V_L^\sigma e^\eta}{1 - e^\eta} \tag{II.15c}$$

$$\eta = \frac{2\lambda + P^\sigma \Delta V^\sigma}{3RT} \tag{II.15d}$$

$$a = \frac{(P^\sigma \Delta V^\sigma / RT - \lambda / RT)(2bRT^{3/2}/3)}{\ln \left[ \frac{V_L^\sigma (V_V^\sigma + b)}{V_V^\sigma (V_L^\sigma + b)} \right]}. \tag{II.15e}$$

Apply the above procedures to S-R-K EOS we can obtain the results below:

$$b = \frac{V_V^\sigma - V_L^\sigma e^\eta}{1 - e^\eta} \tag{II.16a}$$

$$\eta = \frac{\lambda}{RT} \tag{II.16b}$$

$$a = \frac{(P^\sigma \Delta V^\sigma / RT - \lambda / RT)(bRT)}{\ln \left[ \frac{V_L^\sigma (V_V^\sigma + b)}{V_V^\sigma (V_L^\sigma + b)} \right]}. \tag{II.16c}$$

Here we do not use the usual expression of  $a(T)$  prescribed by S-R-K EOS.

Similarly, for P-R EOS we can derive the following results by the same procedures:

$$b = \frac{V_V^\sigma - V_L^\sigma e^\eta}{1 - e^\eta} \tag{II.17a}$$

$$\eta = \frac{\lambda}{RT} \tag{II.17b}$$

$$a = \frac{(P^\sigma \Delta V^\sigma / RT - \lambda / RT)(2\sqrt{2}bRT)}{\ln \left[ \frac{(V_L^\sigma + b(1 - \sqrt{2}))(V_V^\sigma + b(1 + \sqrt{2}))}{(V_V^\sigma + b(1 - \sqrt{2}))(V_L^\sigma + b(1 + \sqrt{2}))} \right]}. \quad (\text{II.17c})$$

In all the above equations,  $\Delta V^\sigma = V_V^\sigma - V_L^\sigma$ , as taken in the Clapeyron equation. Ignoring for the moment contributions from  $a'(\equiv da/dT)$  and  $b'(\equiv db/dT)$ , use of these equations over a range of subcritical temperatures ensures further the tuning of the vapor pressure slope,  $dP^\sigma/dT$  (obtained from differentiation of respective equation of states), and thus of  $\Delta V^\sigma$  through the Clapeyron equation. However, it does not ensure the behavior of the separate saturation volumes  $V_V^\sigma$  and  $V_L^\sigma$ , meaning that these two volumes will have the same positive or negative errors from their experimental values if any error exists while the value of  $\Delta V^\sigma$  will keep almost unchanged. This will be demonstrated in the forthcoming example.

When experimental heat of vaporization data are only available at selected temperatures, such as the normal boiling point (where  $T_r = 0.64 \pm 0.08$  for most compounds), several empirical equations exist for tuning onto these data. First, near the critical temperature, the equation

$$\lambda/RT^c = k_L(1 - T_r)^{\beta'} \quad (\text{II.18})$$

with  $\beta' = 0.38 \pm 0.03$  is closely followed from the critical point down to reduced temperatures of about 0.8 as discussed by Hall & Eubank (1976). For correlations that must go below this reduced temperature, the equation of Majer & Svoboda (1985) is recommended for the entire temperature range:

$$\lambda = A(1 - T_r)^B \exp(-\alpha T_r), \quad (\text{II.19})$$

where the parameters  $A$ ,  $B$  and  $\alpha$  require a minimum of three data points to correlate. While Eq. II.19 has the same limiting properties at the critical point as does Eq. II.18 with  $\beta' = B$ , from fitting data well outside the critical region with Eq. II.19, will not usually fall within the limits prescribed above for  $\beta'$ .

### An Example of Tuning to Different Saturation Properties

Following the derivations in the above two sections, we show here an example of how to tune the two constants  $a$  and  $b$  in an EOS to the saturation properties of two pure components methanol (1) and benzene (2) at different subcritical temperatures. The equation of state used here is Redlich-Kwong EOS. Three cases were tested for the tuning procedures.

*Case I:* Given  $P^\sigma$  and constant  $b$ , find  $V_V^\sigma$ ,  $V_L^\sigma$ , constant  $a$  and  $\lambda$ .

We set  $b$  equal to  $b^c$ , the value from the critical constraints, i.e.  $b = b^c = 0.08664RT^c/P^c$ . Then, use the Wagner vapor pressure equation

$$\ln(P_i^\sigma/P_i^c) = (1 - \tau)^{-1} (W_1\tau + W_2\tau^{1.5} + W_3\tau^3 + W_4\tau^6); \quad \tau \equiv 1 - T/T_i^c \quad (\text{II.20})$$

to solve for the saturation pressure of the component at the given temperature. Then, substitute the saturation pressure into R-K/EOS and Eq. I.1 (MEAR) and neglect the terms of  $a' = da/dT$  and  $b' = db/dT$  we get the following two equations:

$$P^\sigma = \frac{RT}{V_V^\sigma - b} - \frac{a}{\sqrt{T}V_V^\sigma(V_V^\sigma + b)} \quad (\text{II.21})$$

and

$$P^\sigma(V_V^\sigma - V_L^\sigma) = RT \ln \left[ \frac{V_L^\sigma - b}{V_V^\sigma - b} \right] - \frac{a}{b\sqrt{T}} \ln \left[ \frac{V_V^\sigma(V_L^\sigma + b)}{V_L^\sigma(V_V^\sigma + b)} \right] \quad (\text{II.22})$$

It should be noted that  $V_L^\sigma$  should not be applied to the EOS since saturation liquid behavior normally deviates greatly from that equation. With actually three unknowns  $a$ ,  $V_V^\sigma$  and  $V_L^\sigma$  in the above two equations it seems a little tricky to obtain the solutions. Here we have to apply the iteration method to solve Eqs. II.21 & II.22. We start with the experimental values of  $V_V^\sigma$  and  $V_L^\sigma$ , substitute them into Eq. II.22 to solve for a value of  $a$ , then substitute this value of  $a$  into Eq. II.21 to solve for a new set of  $V_V^\sigma$  and  $V_L^\sigma$ . If the obtained results are far away from their experimental values, then repeat the above iterative steps again, until their values in two consecutive iterations fall within the acceptable tolerances. The value of  $a$  will be the correct one to the level of the calculative precision.

Once having obtained the final values of  $V_V^\sigma$ ,  $V_L^\sigma$  and  $a$ , we can use the Clapeyron equation or, alternatively directly use Eq. II.7 to calculate the heat of vaporization. To this point, we have finished all tuning procedures in this case.

The critical constants as well as the four Wagnerian constants  $W_i$  in the above Wagner equation are found in Poling et al. (2001) for each component as listed below:

For methanol:  $T^c = 512.6$  K,  $P^c = 80.9$  bar;

$$W_1 = -8.54796, W_2 = 0.76982, W_3 = -3.10850, W_4 = 1.54481.$$

For benzene:  $T^c = 562.2$  K,  $P^c = 48.9$  bar;

$$W_1 = -6.98273, W_2 = 1.33213, W_3 = -2.62863, W_4 = -3.33399.$$

The values of  $W_i$  in the Wagner equation provide an accurate representation of the experimental data from the triple point to the critical point. The experimental values

of  $P^\sigma$ ,  $V_V^\sigma$ ,  $V_L^\sigma$  and  $\lambda$  are taken from Eubank (1970) for methanol and from Goodwin (1988) for benzene.

*Case II:* Given  $P^\sigma$  and  $V_L^\sigma$ , find  $V_V^\sigma$ , constant  $a$  &  $b$  and  $\lambda$ .

In this case we use the Wagner equation above to calculate the saturation vapor pressure; the saturation liquid volume is calculated from the Racket equation given in Eq. II.12. With these two parameters known, we then substitute them into Eq. I.1 to obtain one equation while substitute  $V_V^\sigma$  for  $V$  in the R-K/EOS to obtain another equation. Now we have three unknowns  $V_V^\sigma$ , constant  $a$  &  $b$  in two equations. Again, we can apply the iteration method starting with the calculated value of  $V_L^\sigma$  and the experimental value of  $V_V^\sigma$  to solve the two equations. When the value of  $V_L^\sigma$  converges the iteration process ends. Final values of constants  $a$  &  $b$  and heat of vaporization  $\lambda$  can then be solved by the same method as in Case I.

*Case III:* Given  $P^\sigma$  and  $\lambda$ , find  $V_V^\sigma$ ,  $V_L^\sigma$ , constant  $a$  &  $b$ .

Similar to the above two cases, we first use the Wagner equation above to calculate the saturation vapor pressure; then use Eq. II.18 & (II.19 given in the previous section to calculate the heat of vaporization with no correction for  $a'$  and  $b'$ . Next, we substitute  $P^\sigma$ ,  $\lambda$ , the experimental values of  $V_V^\sigma$  and  $V_L^\sigma$  into Eq. II.15 c/d/e to calculate the values of  $a$  &  $b$ . Then we substitute these values of  $a$  and  $b$  into the R-K EOS and solve the equation for new values of  $V_V^\sigma$  and  $V_L^\sigma$ . It is these saturation volumes that are reported in Table II.1 under Case III. Recycling these R-K saturation volumes back through Eq. 15 c/d/e to update  $a$  and  $b$  followed by recalculation of the R-K saturation volumes by cubic root solver, etc. only leads to divergence in the examples that we have

tested for benzene and methanol. The reason here is that we are tuning onto both the experimental vapor pressure curve as well as the heat of vaporization so that the Clapeyron identity, Eq. II.2, fixes the saturation volume difference  $\Delta V^\sigma$ . However, the R-K EOS provides its own value of  $\Delta V^\sigma$ , which is not consistent with that of experiment due mainly to the well-known problem of cubic EOS being unable to provide good estimation of liquid saturation volumes.

Alternatively, we can substitute  $P^\sigma$  into Eq. I.1 and  $\lambda$  into Eq. II.7 to get two equations. Another equation can be obtained by substituting  $V_V^\sigma$  for  $V$  in the R-K/EOS. Thus we have three equations and four unknowns  $V_V^\sigma$ ,  $V_L^\sigma$ , constant  $a$  &  $b$ . Apply the iteration procedures to solve the three equations starting with the experimental values of  $V_V^\sigma$  and  $V_L^\sigma$ . The iteration stops until the values of  $V_V^\sigma$  and  $V_L^\sigma$  converge. Final values of constants  $a$  &  $b$  can be calculated by solving the three equations. By this way we should be able to find similar solutions of the unknowns in Case III.

Results of the above three cases for pure components methanol and benzene were given in Table II.1 for the subcritical temperatures of 298.15, 373.15, 413.15 and 493.15 K bearing in mind that the critical temperature of methanol is 512.6 K whereas it is 562.2 K for benzene. The results of the “Not Tuned” case were obtained by first calculating the values of constants  $a$  &  $b$  directly from the critical constraints of the R-K/EOS; then solve the EOS itself to get the values of  $V_V^\sigma$  and  $V_L^\sigma$ ; finally we use Eq. II.7 to solve for the heat of vaporization  $\lambda$ .

**Table II.1. Results for Methanol and for Benzene Using the R-K/EOS**Units:  $a$  --- bar  $K^{1/2}-(\text{cm}^3/\text{mol})^2 \times 10^6$  $b$  ---  $\text{cm}^3/\text{mol}$  $P^\sigma$  --- bar $V_L^\sigma$  ---  $\text{cm}^3/\text{mol}$  $V_V^\sigma$  ---  $\text{cm}^3/\text{mol} \times 10^3$  $\lambda$  --- kJ/mol

<b>Methanol</b>	Not Tuned					
Temp./K	$a$	$b$	$P^\sigma$	$V_L^\sigma$	$V_V^\sigma$	$\lambda$
298.15	217	45.6	1.192	57.2	20.51	26.6
373.15	217	45.6	9.802	65.6	2.845	21.6
413.15	217	45.6	20.989	72.9	1.324	18.5
493.15	217	45.6	64.937	110.6	0.335	8.45

<b>Methanol</b>	Case I ( $P^\sigma$ tuned)					
Temp./K	$a$	$b$	$P^\sigma$	$V_L^\sigma$	$V_V^\sigma$	$\lambda$
298.15	280	45.6	0.170	53.8	145.5	37.9
373.15	264	45.6	3.538	60.0	8.354	34.3
413.15	250	45.6	10.901	66.2	2.632	29.3
493.15	225	45.6	58.080	100.4	0.414	15.8

<b>Methanol</b>	Case II ( $P^\sigma$ & $V_L^\sigma$ tuned)					
Temp./K	$a$	$b$	$P^\sigma$	$V_L^\sigma$	$V_V^\sigma$	$\lambda$
298.15	371	62.7	0.170	74.6	145.3	37.8
373.15	337	61.3	3.539	82.3	8.240	33.9
413.15	309	59.2	10.905	88.3	2.718	29.8
493.15	236	48.9	58.081	114.1	0.391	13.9

<b>Methanol</b>	Case III ( $P^\sigma$ & $\lambda$ tuned)					
Temp./K	$a$	$b$	$P^\sigma$	$V_L^\sigma$	$V_V^\sigma$	$\lambda$
298.15	229	36.3	0.170	42.5	145.3	37.4
373.15	243	39.7	3.519	51.1	8.435	32.7
413.15	249	41.9	10.880	58.2	2.810	29.5
493.15	238	46.4	57.968	92.1	0.346	15.4

**Table II.1. (Continued)**

<b>Methanol</b>	Experiment			
Temp./K	$P^\sigma$	$V_L^\sigma$	$V_V^\sigma$	$\lambda$
298.15	0.170	40.7	143.2	37.4
373.15	3.519	44.9	7.953	32.7
413.15	10.880	48.4	2.643	29.5
493.15	57.968	69.7	0.375	15.4

<b>Methanol</b>	P-R/EOS ( $\omega = 0.565$ ) (Not Tuned)					
Temp./K	$a$	$b$	$P^\sigma$	$V_L^\sigma$	$V_V^\sigma$	$\lambda$
298.15	16.7	41.0	0.167	47.8	168.0	40.6
373.15	14.1	41.0	3.695	53.2	8.350	34.8
413.15	12.8	41.0	11.296	58.5	2.741	30.7
493.15	10.7	41.0	58.572	90.5	0.410	15.0

<b>Benzene</b>	Not Tuned					
Temp./K	$a$	$b$	$P^\sigma$	$V_L^\sigma$	$V_V^\sigma$	$\lambda$
298.15	453	82.8	0.246	100.1	105.0	31.0
373.15	453	82.8	2.695	111.4	10.91	26.2
413.15	453	82.8	6.381	120.2	4.799	23.4
493.15	453	82.8	22.380	151.6	1.298	16.4

<b>Benzene</b>	Case I ( $P^\sigma$ tuned)					
Temp./K	$a$	$b$	$P^\sigma$	$V_L^\sigma$	$V_V^\sigma$	$\lambda$
298.15	490	82.8	0.127	98.4	194.7	34.0
373.15	486	82.8	1.796	108.2	16.51	29.9
413.15	482	82.8	4.711	116.1	6.633	27.4
493.15	470	82.8	19.528	144.7	1.556	20.2



Table II.1. (Continued)

<b>Benzene</b>	Case II ( $P^\sigma$ & $V_L^\sigma$ tuned)					
Temp./K	$a$	$b$	$P^\sigma$	$V_L^\sigma$	$V_V^\sigma$	$\lambda$
298.15	628	109.9	0.126	131.5	194.5	33.8
373.15	601	107.1	1.796	142.5	16.33	29.4
413.15	579	104.4	4.711	150.2	6.464	26.5
493.15	520	95.1	19.529	174.3	1.485	18.7

<b>Benzene</b>	Case III ( $P^\sigma$ & $\lambda$ tuned)					
Temp./K	$a$	$b$	$P^\sigma$	$V_L^\sigma$	$V_V^\sigma$	$\lambda$
298.15	442	73.6	0.127	87.2	194.2	33.8
373.15	465	78.3	1.803	102.0	16.48	29.6
413.15	469	79.6	4.727	111.1	6.628	27.0
493.15	460	80.0	19.605	137.8	1.561	19.9

<b>Benzene</b>	Experiment				
Temp./K	$P^\sigma$	$V_L^\sigma$	$V_V^\sigma$	$\lambda$	
298.15	0.127	89.3	193.8	33.8	
373.15	1.803	98.8	16.34	29.6	
413.15	4.727	105.1	6.533	27.0	
493.15	19.605	125.2	1.513	19.9	

<b>Benzene</b>	P-R/EOS ( $\omega = 0.565$ ) (Not Tuned)					
Temp./K	$a$	$b$	$P^\sigma$	$V_L^\sigma$	$V_V^\sigma$	$\lambda$
298.15	26.9	74.4	0.142	87.5	196.8	32.6
373.15	24.3	74.4	1.817	95.8	16.77	29.4
413.15	23.0	74.4	4.714	102.6	6.727	27.1
493.15	20.8	74.4	19.569	128.4	1.527	20.1

By comparing the results of the different cases with the experimental values in Table II.1, we can draw the following conclusions. These conclusions are all generally consistent with those for the components of other azeotropic binary systems with which Eubank et al. (1995) have worked.

First, by comparing the results of the “Not Tuned” case with the experimental values, it is easy to find that the R-K EOS does not provide accurate saturation properties for pure components when its constants are fixed by the critical constraints. The deviations are less severe for benzene as compared to methanol because benzene does not have the strong polar effects, including hydrogen bonding. These deviations are nevertheless significant even for simple hydrocarbons and inert gases (Barrufet & Eubank, 1989).

Second, by comparing the results of Case I and the experimental values, we see that by tuning only the  $a$  constant to experimental vapor pressures, through the Wagner equation, Eq. II.20, using the Maxwell Equal-Area-Rule, Eq. I.1, the values under Case I are significantly improved compared to experiment. The calculated values of the saturation vapor volumes and the heat of vaporization are in good agreement with the experimental results. The saturation liquid volumes are somewhat improved by tuning  $a$  but remain poor.

Third, in Case II we further tuned constant  $b$  to match the liquid volumes of the Rackett equation with  $Z_c = 1/3$ . This only makes the liquid saturation volumes worse compared with the situation in Case I. An alternative here is to use the experimental values of  $Z_c$  (0.224 for methanol and 0.268 for benzene) which creates a very good match for the liquid saturation volumes with other properties remaining close to

experimental values. But this creates an inconsistency problem since the cubic equations of states are not supposed to be applicable for liquids.

Fourth, in Case III we combined the tuning of constants  $a$  and  $b$  with Eq. II.15  $c/d/e$  to match the saturation vapor pressure and the heat of vaporization. This provides the best set of saturation properties for both methanol and benzene.

Finally, we show the results from the classic Peng-Robinson EOS, with the formulas presented in Chapter I with the experimental acentric factors but no tuning to actual saturation properties. The results are superior to the R-K EOS' Not Tuned case but about the same as either Case I or Case III for saturation vapor volumes. It is superior to Case I for liquid volumes and even Case III for benzene but not for methanol; it is not as good as Case I for heats of vaporization, with a few exceptions occurring where both predictions are very close to experimental values. We acknowledge the well-known fact that the Peng-Robinson EOS is generally superior to the simpler Redlich-Kwong EOS; what we have shown in Tables II.1 & II.2 is that the R-K EOS can be made to work as well as P-R EOS when it has been tuned to saturation vapor pressure and heat of vaporization data whereas P-R EOS has none. The main point here is to show that very simple EOS can be made to work well in commercial simulators when considerable tuning has been performed.

**Table II.2. Results for Methanol and for Benzene Using the R-K/EOS with Eqs. II.15c/d/e together with Estimated Values of the Experimental Saturation Volumes**

Units:  $a$  --- bar  $K^{1/2}-(\text{cm}^3/\text{mol})^2 \times 10^6$ ,  $b$  ---  $\text{cm}^3/\text{mol}$

$P^\sigma$  --- bar

$V_L^\sigma$  ---  $\text{cm}^3/\text{mol}$

$V_V^\sigma$  ---  $\text{cm}^3/\text{mol} \times 10^3$

$\lambda$  --- kJ/mol

<b>Methanol</b>	Case III ( $P^\sigma$ & $\lambda$ tuned)					
Temp./K	$a$	$b$	$P^\sigma$	$V_L^\sigma$	$V_V^\sigma$	$\lambda$
298.15	206	32.4	0.170	37.9	145.4	37.4
373.15	227	36.9	3.519	47.4	8.461	32.7
413.15	238	39.8	10.880	55.1	2.828	29.5
493.15	219	42.3	57.968	83.3	0.416	15.4

<b>Methanol</b>	Experiment				
Temp./K	$P^\sigma$	$V_L^\sigma$	$V_V^\sigma$	$\lambda$	
298.15	0.170	40.7	143.2	37.4	
373.15	3.519	44.9	7.953	32.7	
413.15	10.880	48.4	2.643	29.5	
493.15	57.968	69.7	0.375	15.4	

<b>Benzene</b>	Case III ( $P^\sigma$ & $\lambda$ tuned)					
Temp./K	$a$	$b$	$P^\sigma$	$V_L^\sigma$	$V_V^\sigma$	$\lambda$
298.15	439	73.0	0.127	86.4	194.2	33.8
373.15	459	77.1	1.803	100.4	16.49	29.6
413.15	463	78.6	4.727	109.5	6.636	27.0
493.15	456	79.1	19.605	135.9	1.567	19.9

<b>Benzene</b>	Experiment				
Temp./K	$P^\sigma$	$V_L^\sigma$	$V_V^\sigma$	$\lambda$	
298.15	0.127	89.3	193.8	33.8	
373.15	1.803	98.8	16.34	29.6	
413.15	4.727	105.1	6.533	27.0	
493.15	19.605	125.2	1.513	19.9	

### The Volume Problem

To follow the procedure of Case III in the above section, experimental saturation volumes are necessary. However, these values are often not available. The solution to this problem is to make suitable estimates as detailed in the following procedure:

1. Estimate the saturated liquid volumes from the Rackett equation, Eq. II.12, taking care to use the experimental value of the critical compressibility factor  $Z_c$ .
2. Differentiate the Wagner vapor pressure equation, Eq. II.20, for the vapor pressure slope and apply to the Clapeyron identity, Eq. II.2, together with experimental heats of vaporization, using Eq. II.19 when data points are limited. Calculate the saturation volume difference  $\Delta V^\circ$  from the Clapeyron identity and add to the saturated liquid volume to get the saturated vapor volume.
3. Calculate constants  $a$  and  $b$  at each temperature using the form of Eq. II.15 to match your particular cubic EOS. If you wish to include the secondary terms  $a'(\equiv da/dT)$  and  $b'(\equiv db/dT)$ , use the procedure below instead of Eq. II.15.

As an example of this procedure as applied to benzene and to methanol, Table II.2 contains results similar to those of Case III in Table II.1. In comparison to the experimental values, these results are not particularly better or worse than those of Case III, indicating that although the constants  $a$  and  $b$  in the R-K EOS should be deemed as functions of temperature, the effect of temperature-dependence is limited.

### Inclusion of $a'$ and $b'$ Terms

As shown in the previous section, the constants  $a'$  and  $b'$  in the cubic equations of states are somewhat dependent on temperature. Thus Eqs. II.5, II.7, II.9 & II.11 are not

complete as the identity of Eq. II.3 has been integrated without regard for secondary contributions from  $a'(\equiv da/dT)$  and  $b'(\equiv db/dT)$ . Taking these temperature-dependent terms into account, we need to re-derive the expressions of the heats of vaporization as follows.

For van der Waals EOS, the new isochoric slope with the  $a'$  and  $b'$  terms becomes

$$\left(\partial P^{\text{EOS}}/\partial T\right)_V = \frac{R}{V-b} + \frac{RTb'}{(V-b)^2} - \frac{a'}{V^2}. \quad (\text{II.23})$$

Substitute it into Eq. II.3 for integration, rearrange the result to obtain the new dimensionless term of heat of vaporization:

$$\frac{\lambda}{RT} = \ln\left(\frac{V_V^\sigma - b}{V_L^\sigma - b}\right) + \frac{b'T(\Delta V^\sigma)}{(V_V^\sigma - b)(V_L^\sigma - b)} - \frac{a'(\Delta V^\sigma)}{RV_V^\sigma V_L^\sigma} \quad (\text{II.24})$$

For Redlich-Kwong EOS, the new isochoric slope with the  $a'$  and  $b'$  terms is

$$\left(\partial P^{\text{EOS}}/\partial T\right)_V = \frac{R}{V-b} + \frac{a}{2V(V+b)T^{3/2}} - \frac{a'}{\sqrt{TV}(V+b)} + \frac{RTb'}{(V-b)^2} + \frac{ab'}{\sqrt{TV}(V+b)^2} \quad (\text{II.25})$$

Substitution of Eq. II.25 into Eq. II.3, after integration and rearrangement we get the corrected heat of vaporization:

$$\begin{aligned} \frac{\lambda}{RT} = & \ln\left(\frac{V_V^\sigma - b}{V_L^\sigma - b}\right) - \left(\frac{a}{2bRT^{3/2}}\right) \ln\left[\frac{V_L^\sigma(V_V^\sigma + b)}{V_V^\sigma(V_L^\sigma + b)}\right] \\ & + \frac{b'T(\Delta V^\sigma)}{(V_V^\sigma - b)(V_L^\sigma - b)} - \frac{ab'}{Rb\sqrt{T}} \frac{\Delta V^\sigma}{(V_V^\sigma + b)(V_L^\sigma + b)} \\ & + \frac{a' - a(b'/b)}{Rb\sqrt{T}} \ln\left[\frac{(V_V^\sigma + b)V_L^\sigma}{(V_L^\sigma + b)V_V^\sigma}\right] \end{aligned} \quad (\text{II.26})$$

Similarly, for Soave-Redlich-Kwong EOS, if we do not use the usual expression for constant  $a(T)$  prescribed by the EOS itself, the new isochoric slope will become:

$$\left(\frac{\partial P^{\text{EOS}}}{\partial T}\right)_V = \frac{R}{V-b} + \frac{RTb'}{(V-b)^2} - \frac{a'}{V(V+b)} + \frac{ab'}{V(V+b)^2} \quad (\text{II.27})$$

Substitution of it into Eq. II.3 for integration, after proper simplification and rearrangement we get:

$$\begin{aligned} \frac{\lambda}{RT} = & \ln\left(\frac{V_V^\sigma - b}{V_L^\sigma - b}\right) + \frac{b'T(\Delta V^\sigma)}{(V_V^\sigma - b)(V_L^\sigma - b)} - \frac{ab'}{Rb} \frac{\Delta V^\sigma}{(V_V^\sigma + b)(V_L^\sigma + b)} \\ & + \frac{a' - a(b'/b)}{Rb} \ln\left[\frac{(V_V^\sigma + b)V_L^\sigma}{(V_L^\sigma + b)V_V^\sigma}\right] \end{aligned} \quad (\text{II.28})$$

Finally, for Peng-Robinson EOS, the new isochoric slope is

$$\left(\frac{\partial P^{\text{EOS}}}{\partial T}\right)_V = \frac{R}{V-b} + \frac{RTb'}{(V-b)^2} - \frac{a'}{V^2 + 2bV - b^2} + \frac{2ab'(V-b)}{(V^2 + 2bV - b^2)^2}. \quad (\text{II.29})$$

Substitute the above expression into Eq. II.3. Again we do not use the usual expression for constant  $a(T)$  prescribed by the EOS itself. After complicated integration and simplification we obtain:

$$\begin{aligned} \frac{\lambda}{RT} = & \ln\left(\frac{V_V^\sigma - b}{V_L^\sigma - b}\right) + \frac{b'T(\Delta^\sigma)}{(V_V^\sigma - b)(V_L^\sigma - b)} + \left(\frac{ab'}{b}\right) \frac{V_V^\sigma[(V_L^\sigma)^2 + 2bV_L^\sigma - b^2]}{V_L^\sigma[(V_V^\sigma)^2 + 2bV_V^\sigma - b^2]} \\ & + \frac{a' - a(b'/b)}{2\sqrt{2}Rb} \ln\left[\frac{[V_V^\sigma + b(1-\sqrt{2})][V_L^\sigma + b(1+\sqrt{2})]}{[V_L^\sigma + b(1-\sqrt{2})][V_V^\sigma + b(1+\sqrt{2})]}\right] \end{aligned} \quad (\text{II.30})$$

Combination of the above corrected expressions for heats of vaporization with those from Eq. I.1 for the same EOS results in a set of equations. Then solve these equations using iterative methods similar to those used in the three cases in the previous

section. We start the iteration with the experimental values of  $V_V^\sigma$  and  $V_L^\sigma$  until convergence of constants  $a$  &  $b$  over the entire temperature range. The final converged result is then consistent with the Clapeyron equation. Table II.3 shows our updated results for Case III in Table II.1 when this detailed correction procedure is followed. The R-K saturation volumes given in Table II.3 are again from the cubic root solver. Because constants  $a$  &  $b$  do not change greatly with temperature, simple numerical techniques such as Newton backward method, etc. can be employed to calculate the terms  $a'(\equiv da/dT)$  and  $b'(\equiv db/dT)$ , without the need to correlate any mathematical relations between  $a$  &  $b$  versus temperature, thus greatly reducing the amount of work to calculate the correctional terms incurred from  $a'$  and  $b'$ .

The results in Table II.3 differ only marginally from those of Case III appearing in Table II.1. Generally, the saturated liquid volumes are closer to experimental values but the improvement is minor. This correction procedure for  $a'$  and  $b'$  runs well except in the region near the critical temperature where the heat of vaporization approaches zero. Because of the added complexity, we do not recommend this correction for commercial applications. However, it should be kept in mind that in using Eqs. II.14 ~ II.17, the neglect of  $a'$  &  $b'$  will lead to minor inconsistencies with the Clapeyron identity. These inconsistencies should not be confused with those inflicted by use of the volumes of the equations of state.



**Table II.3. Results for Methanol and for Benzene Using the R-K/EOS with Inclusion of the  $a'$  and  $b'$  Terms for the Heat of Vaporization**

Units:  $a$  --- bar K<sup>1/2</sup>-(cm<sup>3</sup>/mol)<sup>2</sup> x 10<sup>6</sup>

$b$  --- cm<sup>3</sup>/mol

$P^\sigma$  --- bar

$V_L^\sigma$  --- cm<sup>3</sup>/mol

$V_V^\sigma$  --- cm<sup>3</sup>/mol x 10<sup>3</sup>

$\lambda$  --- kJ/mol

<b>Methanol</b>	Corrected Values ( $P^\sigma$ & $\lambda$ tuned)					
Temp./K	$a$	$b$	$P^\sigma$	$V_L^\sigma$	$V_V^\sigma$	$\lambda$
298.15	227	35.9	0.170	42.1	145.3	37.4
373.15	236	38.8	3.519	50.1	8.448	32.7
413.15	238	40.5	10.880	56.6	2.829	29.5
493.15	216	42.2	57.968	85.0	0.428	15.4

<b>Benzene</b>	Corrected Values ( $P^\sigma$ & $\lambda$ tuned)					
Temp./K	$a$	$b$	$P^\sigma$	$V_L^\sigma$	$V_V^\sigma$	$\lambda$
298.15	443	73.8	0.127	87.4	194.2	33.8
373.15	462	77.8	1.803	101.4	16.49	29.6
413.15	465	78.9	4.727	110.0	6.634	27.0
493.15	452	78.4	19.605	134.7	1.572	19.9

## CHAPTER III

### CHARACTERISTICS OF ACTIVITY COEFFICIENT MODELS FOR LIQUID SOLUTIONS

#### Homogeneous Azeotropes at Low Pressures

In a vapor-liquid equilibrium system the bubble-point curve of pressure vs  $x_1$  at constant temperature (or in the bubble-point curve of temperature vs  $x_1$  at constant pressure) should obey the following identity:

$$y_i \hat{\phi}_i^V P^{BP} = \sum_{i=1}^2 x_i \gamma_i P_i^\sigma \exp\left(\frac{1}{RT} \int_{P_i^\sigma}^{P^{BP}} V_i^L dP\right), \quad i = 1, 2 \quad (\text{III.1})$$

If the vapor phase is at low pressure and the liquid phase is not too non-ideal, then both vapor-phase imperfections and the Poynting correction terms may be neglected. Then, by adding up the two identities from Eq. III.1 with  $i = 1, 2$  we obtain

$$P^{BP} = x_1 \gamma_1 P_1^\sigma + x_2 \gamma_2 P_2^\sigma \quad (\text{III.2})$$

To find a homogeneous azeotrope at constant temperature we differentiate Eq. III.2 with respect to  $x_1$  and set the derivative to zero. Eq. I.7 is the Gibbs-Duhem form that applies for VLE and here we ignore the  $V^E$  term for simplicity. Combination of this short form of the Gibbs-Duhem equation with the differentiated form of Eq. III.2 results in the azeotropic condition:

$$\nu = P_1^\sigma / P_2^\sigma = (\gamma_2 / \gamma_1)^{AZ}, \quad \text{or} \quad \nu = \ln \gamma_2 - \ln \gamma_1 \quad (\text{III.3})$$

At the pure end point when  $x_1 \rightarrow 0$  we have  $\gamma_2 = 1.0$ , then the derivative of Eq. III.2 will become

$$(\partial P^{\text{BP}}/\partial x_1)_T \Big|_{x_1 \rightarrow 0} = \gamma_1 P_1^\sigma - P_2^\sigma = P_2^\sigma (v\gamma_1^\infty - 1) \quad (\text{III.4})$$

and likewise for the slope as  $x_1$  approaches unity by interchanging the subscripts between the two components. Eq. III.4 is valuable as the sign of this slope at  $x_1 = 0$  versus its sign at  $x_1 = 1$  provides information about whether an azeotrope exists and whether the azeotrope is positive or negative. That is, if  $(\partial P^{\text{BP}}/\partial x_1)_T$  is positive at  $x_1 = 0$  but negative at  $x_1 = 1$  then we know that a positive azeotrope exists. On the other hand, if  $(\partial P^{\text{BP}}/\partial x_1)_T$  is negative at  $x_1 = 0$  but positive at  $x_1 = 1$  then a negative azeotrope must exist.

### Symmetric Solution Model

For a binary solution this model is expressed as

$$G^E/RT = Ax_1x_2 \quad (\text{III.5})$$

and the activity coefficients can be derived from  $\ln \gamma_i = \overline{G}_i^E/RT$  which results in

$$\ln \gamma_1 = Ax_2^2; \quad \ln \gamma_2 = Ax_1^2; \quad \ln \gamma_1^\infty = A = \ln \gamma_2^\infty \quad (\text{III.6})$$

where  $A$  is a constant but varies with temperature. Figure III.1 is a typical graph of  $\ln \gamma_1$  and of  $\ln \gamma_2$  vs  $x_1$  showing the mirror-image symmetry about  $x_1 = 0.5$ . As for all the models considered here, the Gibbs-Duhem equation is obeyed but this simple model is usually not followed in the nature of highly non-ideal liquid solutions. From Eq. III.6 it is easy to find that the slopes of the two curves of Figure III.1 are  $-2Ax_2$  and  $2Ax_1$ , respectively, and the second derivatives are both  $2A$ . Since  $A \neq 0$  there can be no

inflection points nor local extremum except that required of all the models by the Gibbs-Duhem equation for  $\ln\gamma_1$  at  $x_1 = 1$  and also for  $\ln\gamma_2$  at  $x_1 = 0$ .

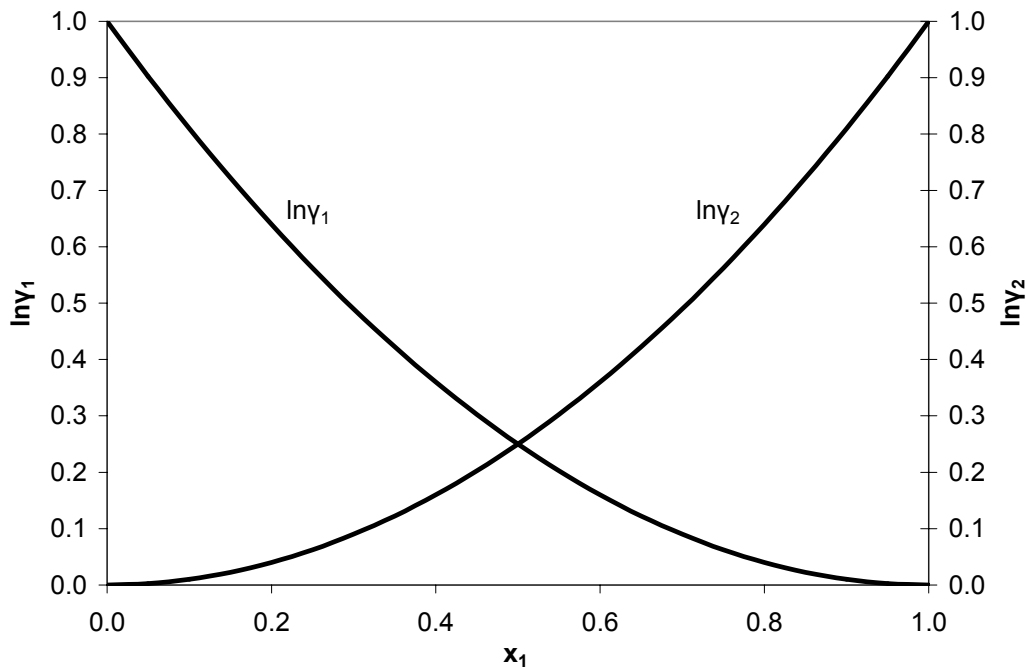


**Figure III.1. Graph of  $\ln\gamma_1$  and of  $\ln\gamma_2$  vs  $x_1$  showing the mirror-image symmetry about  $x_1 = 0.5$  for the symmetric solution model. Here the constant  $A$  has been set to unity to avoid liquid-liquid phase splitting (for  $A > 2$ ).**

To see if the liquid solution will split into two phases, we need to examine the curve of the Gibbs energy of mixing ( $\Delta_m G/RT$ ) vs  $x_1$  at constant temperature and pressure. Let us define

$$g = \Delta_m G/RT = x_1 \ln x_1 + x_2 \ln x_2 + G^E/RT \quad (\text{III.7})$$

The phase stability criterion requires that the second derivative of  $g$  vs  $x_1$  must remain positive for all  $x_1$  if the liquid solution is to maintain single-phase stability for all

values of the overall mole fraction  $z_1$  representing one or more liquid phases. See Tester and Modell (1997) for an excellent discussion of the difference between equilibrium and phase stability. Differentiating Eq. III.7 vs  $x_1$  twice we get the following equations:

$$g' = \partial(\Delta_m G/RT)/\partial x_1 = \ln(x_1/x_2) + A(x_2^2 - x_1^2) \quad (\text{III.8a})$$

and

$$g'' = \partial^2(\Delta_m G/RT)/\partial x_1^2 = (x_1 x_2)^{-1} - 2A \quad (\text{III.8b})$$

From Eq. III.8a it is obvious that  $g' = 0$  at  $x_1 = 0.5$  so that there is a local extremum at this point. Single-phase stability is maintained when  $(x_1 x_2)^{-1} > 2A$  from Eq. III.8b. As the term  $(x_1 x_2)^{-1}$  is  $+\infty$  at the pure end-points falling to a minimum of 4 at  $x_1 = 0.5$ , liquid-liquid phase splitting is only possible when  $A > 2$  and local minima is given by  $\ln(x_2/x_1) = A(x_2^2 - x_1^2) = A(1 - 2x_1)$  for the composition of the two liquid phases  $x_1^I = (0.5 + \varepsilon)$  and  $x_1^{II} = (0.5 - \varepsilon)$  (Eubank and Barrufet, 1998). Any result for this model that assumes a single liquid phase is invalidated when the result falls in the liquid-liquid immiscibility gap of  $x_1 \in (x_1^{II}, x_1^I)$ .

As indicated above, constant  $A$  of Eq. III.5) varies somewhat with temperature. Assuming the following  $T$  dependence of  $A$  (Smith et al., 2001):

$$A = \frac{a}{T} + b - c \ln T \quad (\text{III.9})$$

where  $a$ ,  $b$  and  $c$  are constants. Then through some mathematical manipulations we can obtain

$$\frac{dA}{dT} = -\frac{1}{T^2}(a + cT) = -\frac{H^E}{x_1 x_2 RT^2} \quad (\text{III.10})$$

in which  $H^E$  is the excess enthalpy. Thus for an endothermic system (positive  $H^E$ )  $dA/dT < 0$  and for an exothermic system (negative  $H^E$ )  $dA/dT > 0$ . The curve of  $A$  vs  $T$  is shown in Figure III.2 below:

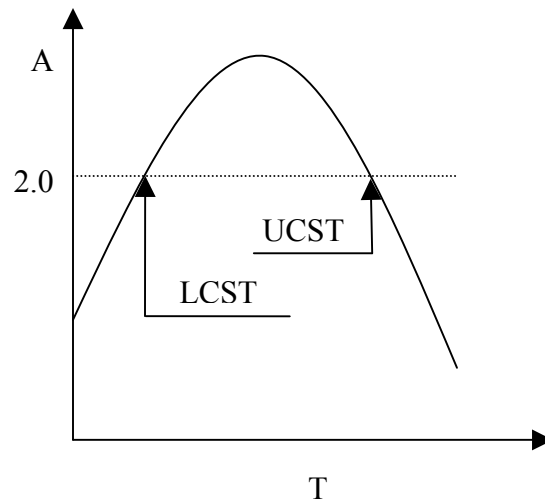


**Figure III.2. Schematic diagram of parameter  $A$  vs temperature  $T$  in one-constant Margules model.**

From the above graph it is seen that  $dA/dT > 0$  at a consolute point ( $A = 2$ ) implies a *lower critical solution temperature* (LCST), whereas  $dA/dT < 0$  at a consolute point implies an *upper critical solution temperature* (UCST) (Prausnitz et al., 1999).

By solving Eqs. III.3 and III.6 we get the condition under which a homogeneous azeotrope exists as

$$\ln v = A(2x_1 - 1) \text{ or } 0 \leq \left| \frac{\ln v}{A} \right| \leq 1; \text{ with } x_1^{AZ} = \frac{1}{2} \left[ 1 + \frac{\ln(P_1^\sigma/P_2^\sigma)}{A} \right] \quad (\text{III.11})$$

However, any homogeneous azeotrope forecast by the above equation will not occur when  $x_1^{AZ}$  falls into the liquid-liquid immiscibility gap provided above.

In summary, the symmetric solution model can provide homogeneous azeotropes for VLE and also liquid-liquid phase splitting which allows it to be used for VLLE calculations involving both homogeneous and heterogeneous azeotropes. Thus it has some versatility in qualitative reproduction of reasonably complex phase behavior.

### **Margules (two-constant) Model**

This model is expressed as

$$G^E/RT = x_1x_2(A_{21}x_1 + A_{12}x_2) \quad (\text{III.12})$$

with the activity coefficients shown below:

$$\ln\gamma_1 = x_2^2[A_{12} + 2(A_{21} - A_{12})x_1] \quad (\text{III.13a})$$

$$\ln\gamma_2 = x_1^2[A_{21} + 2(A_{12} - A_{21})x_2], \quad (\text{III.13b})$$

$$\ln\gamma_1^\infty = A_{12}; \quad \ln\gamma_2^\infty = A_{21} \quad (\text{III.13c})$$

For two-constant models we arbitrarily choose the first component in the binary solution to be the one for which  $A_{12} \geq A_{21}$  in Margules model or  $\alpha \geq \beta$  in the van Laar model below. We make this choice in order to define a new parameter  $r \equiv A_{12}/A_{21}$  in Margules and  $r \equiv \alpha/\beta$  in van Laar such that (1)  $r > 1$  when both constants are positive, (2)  $0 < r < 1$  when both constants are negative and (3)  $r < 0$  only when the first constant is positive and the second is negative. Then all three phenomena listed in Chapter I can be described and forecast in terms of  $r$ .

### ***Extrema and Inflection Points***

For the Margules model, Figure III.3a shows a somewhat atypical graph of  $\ln\gamma_1$  and of  $\ln\gamma_2$  vs  $x_1$  corresponding to  $r = 3$ . In Figure III.3a,  $\ln\gamma_2$  has an inflection point at

$x_1 = 0.42$  then has a maximum at  $x_1 = 0.83$  before falling back to  $A_{21}$  at  $x_1 = 1$ . In keeping with Eq. I.5,  $\ln\gamma_1$  is zero at  $x_1 = 0.75$  falling to its minimum at  $x_1 = 0.83$  and then an inflection point at  $x_1 = 0.92$  as better seen on Figure III.3b, a magnification of Figure III.3a. To find the general equations that forecast such behavior for any value of the ratio of Margules constants  $r$ , we first take the first and second derivatives of Eq. III.13 a&b as follows:

$$\frac{\partial \ln\gamma_1}{\partial x_1} = -2x_2[A_{12} + 2(A_{21} - A_{12})x_1] + 2x_2^2(A_{21} - A_{12}) \quad (\text{III.14a})$$

$$\frac{\partial \ln\gamma_2}{\partial x_1} = 2x_1[A_{21} + 2(A_{12} - A_{21})x_2] + 2x_1^2(A_{21} - A_{12}) \quad (\text{III.14b})$$

$$\frac{\partial^2 \ln\gamma_1}{\partial x_1^2} = 2A_{12} + 4(A_{21} - A_{12})x_1 - 8x_2(A_{21} - A_{12}) \quad (\text{III.14c})$$

$$\frac{\partial^2 \ln\gamma_2}{\partial x_1^2} = 2A_{21} + 4(A_{12} - A_{21})x_2 + 8x_1(A_{21} - A_{12}) \quad (\text{III.14d})$$

Now set the derivatives in Eq. III.14a&b to zero then we obtain the maximum/minimum or extrema condition for  $\ln\gamma_1$  and for  $\ln\gamma_2$ :

$$x_1^M = \frac{2r-1}{3(r-1)} \quad (\text{III.15})$$

Similarly, set the derivatives in Eq. III.14c&d to zero then we obtain the conditions for inflection point of  $\ln\gamma_1$  and for  $\ln\gamma_2$ , respectively:

$$x_1^{\text{IP1}} = \frac{5r-4}{6(r-1)} \text{ for } \ln\gamma_1, \text{ and } x_1^{\text{IP2}} = \frac{2r-1}{6(r-1)} \text{ for } \ln\gamma_2 \quad (\text{III.16})$$

Figure III.3 is a graph of these special values of  $x_1$  vs  $r$  reflecting that  $x_1 \in (0, 1)$ . By imposing the restriction of  $0 \leq x_1 \leq 1$  onto Eqs. III.15 & III.16 it is found that  $\ln\gamma_1$



and  $\ln\gamma_2$  do not have extrema when  $r \in (0.5, 2)$ , whereas  $\ln\gamma_1$  does not have inflection points when  $r \in (0.8, 2)$  and  $\ln\gamma_2$  does not have inflection points when  $r \in (0.5, 1.25)$ . These results and those below for the formation of a homogeneous azeotrope are independent but both are invalid in a region of  $x_1$  where the single liquid phase splits into two liquid phases as given in the third section for the Margules model. Figure III.4 is a graphical representation of Eqs. III.15 & III.16. It demonstrates part of the versatility of the Margules model and that it can provide *qualitatively* most of the general behavioral patterns of real solutions --- or at least those given in Abbott and Prausnitz (1994) and the most recent edition of Smith et al., 2001.

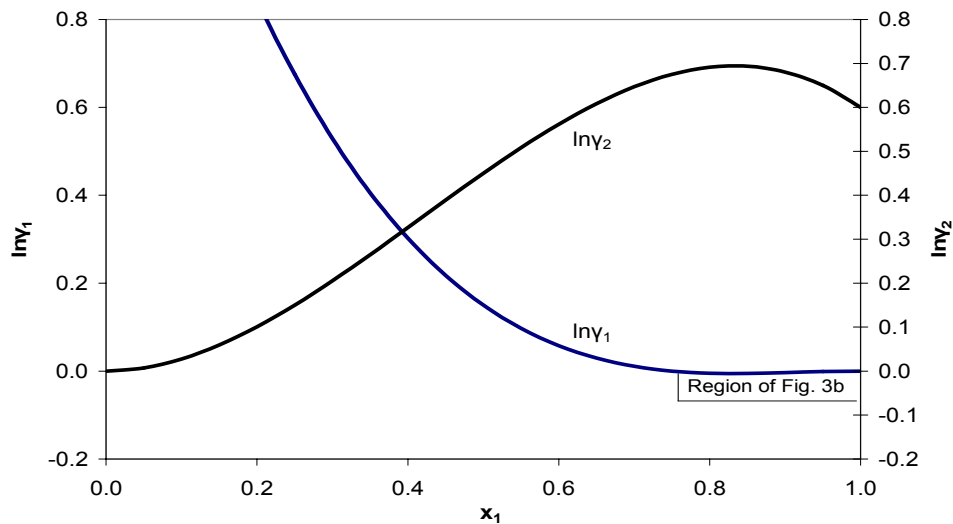


**Figure III.3a. Graph of  $\ln\gamma_1$  and of  $\ln\gamma_2$  vs  $x_1$  for the Margules model with  $A_{12} = 1.8$  and  $A_{21} = 0.6$ . In keeping with Eq. III.15),  $\ln\gamma_1$  has a minimum of near  $-0.0055$  at  $x_1 = 0.83$  with  $\ln\gamma_2$  having a maximum at the same mole fraction as dictated by Eq. III.15). From Eq. III.16),  $\ln\gamma_2$  has an inflection point at  $x_1 = 0.42$  and  $\ln\gamma_1$  has an inflection point at  $x_1 = 0.92$ .**

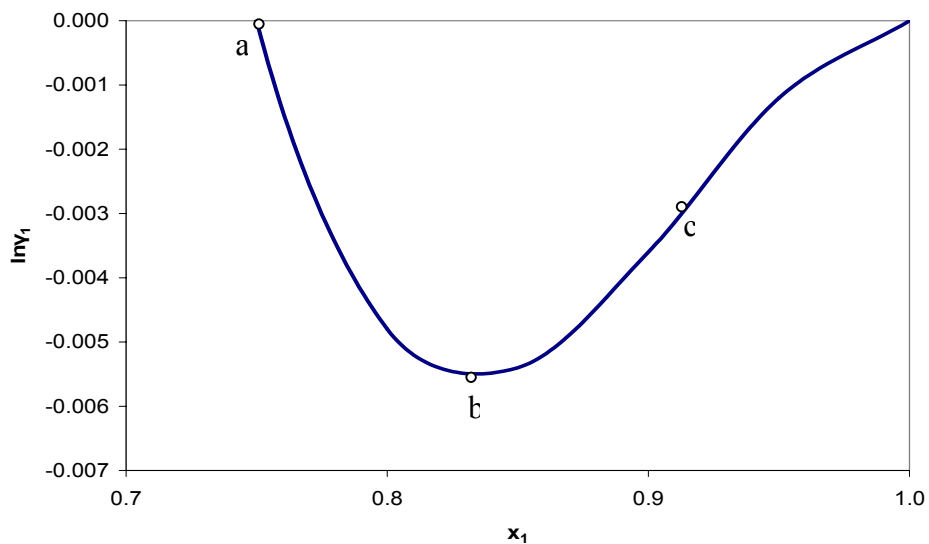


**Figure III.3b.** Insert of region of Fig. III.3a. Here  $\ln\gamma_1$  : (a) passes through zero, (b) reaches its minimum value near  $x_1 = 0.83$  and (c) has an inflection point at  $x_1 = 0.92$ .

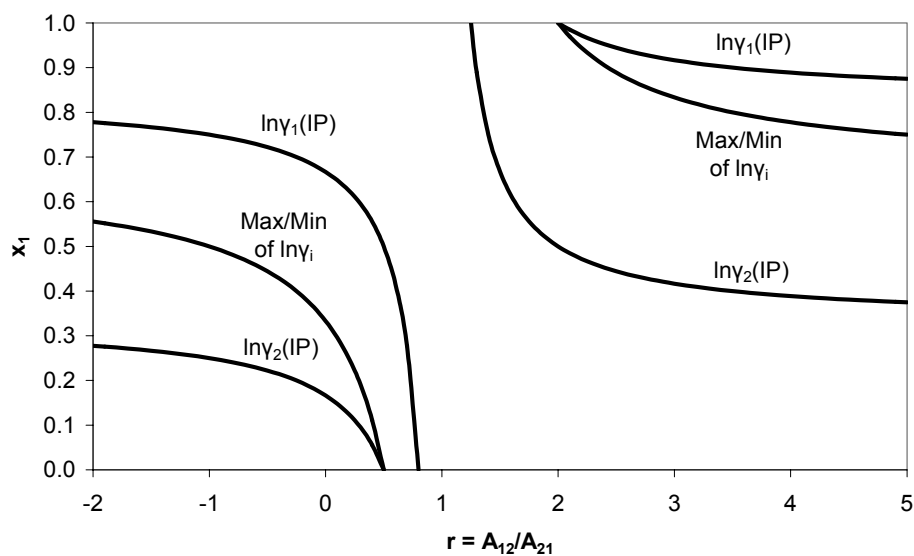


**Figure III.4.** Margules (two-constant) locus lines for extrema and inflection points on  $\ln\gamma_i$  vs  $x_1$  graphs with  $A_{12} > A_{21}$ .

### ***Liquid-liquid Phase Splitting***

As with the symmetric solution model, we examine the graph of function  $g = \Delta_m G/RT = x_1 \ln x_1 + x_2 \ln x_2 + G^E/RT$  vs  $x_1$  checking for inflection points, which occur as pairs, with the liquid-liquid immiscibility gap of  $(x_1^{\text{II}}, x_1^{\text{I}})$  appearing outside the two inflection points. Typical graphs of  $g$  vs  $x_1$  are shown in Figure III.5 for the Margules two-constant model. Simple, unsymmetrical models such as Margules and van Laar require preparation of this graph to check the liquid phase stability when one or both of the model constants exceed two. When one constant exceeds two and the other constant is less than two, the liquid phase may or may not exhibit phase splitting as shown in Figure III.5. When both constants exceed two, phase splitting will occur but it is necessary to find the liquid-liquid immiscibility gap of  $(x_1^{\text{II}}, x_1^{\text{I}})$  in order to know if a system of known overall composition falls inside this gap (L-L equilibria) or outside the gap (single liquid phase).

With the Margules model the inflection points appear for a binary solution when

$$g'' = \frac{1}{x_1 x_2} - 2x_1 A_{21} - 2x_2 A_{12} - 2(x_1 - x_2)(A_{21} - A_{12}) \leq 0$$

which is simplified to

$$f(x_1) = 2x_1 x_2 [3x_1(1-r) + (2r-1)] \geq (A_{21})^{-1}. \quad (\text{III.17})$$

For a given value of  $A_{21}$ , the *onset* of phase splitting occurs where the two inflection points first appear at the same point or at the point of  $x_1$  where  $f(x_1)$  has the maximum value or  $g''' = 0$ . Solving this equation we get

$$x_1^{\text{onset}} = \frac{(5r-4) - \sqrt{7-13r+7r^2}}{9(r-1)} \quad (\text{III.18})$$

Insertion of this value of  $x_1$  into Eq. III.17 used as an equality and solving for  $r = r_{\text{MIN}}$  as a function of  $A_{21}$  yields the left-ordinate of Figure III.6 as  $A_{12}(\text{min}) = A_{21}r_{\text{MIN}}$ . This value of  $r_{\text{MIN}}$  then provides  $x_1^{\text{onset}}$  from Eq. III.18 for the right-ordinate curve of Figure III.6.

A mathematical analysis reveals that  $\lim_{r \rightarrow 1} x_1^{\text{onset}} = 0.5$  and  $x_1^{\text{onset}}$  monotonically decreases when  $r$  increases. Thus all values of  $x_1^{\text{onset}}$  are less than 0.5 as  $A_{12} > A_{21}$ . For  $A_{21} < 0.5$ , Figure III.6 allows the reader to (i) determine if phase splitting occurs --- the condition of  $A_{12} > A_{12}(\text{min})$  for a given value of  $A_{21}$  must be met for phase splitting to occur, and (ii) when it does occur to know roughly that the liquid-liquid immiscibility gap of  $(x_1^{\text{II}}, x_1^{\text{I}})$  is centered near  $x_1^{\text{onset}}$  with the magnitude of the gap increasing when  $[A_{12} - A_{12}(\text{min})]$  increases. However, it must be reminded that the specific values of the two end-points of the immiscibility gap can not be read out from Figure III.6 directly.

The above procedure works well when  $A_{21} < 2$  and  $A_{12} > 2$ , but it fails when both Margules constants exceed two. To find the equilibrium values of  $x_1^{\text{II}}$  and  $x_1^{\text{I}}$  it is necessary to examine the graph of  $g$  vs  $x_1$  and apply the tangent line method or, alternatively, apply the equal-area-rule (Eubank and Hall, 1995) to the graph of  $g' = dg/dx_1$  vs  $x_1$ . While such procedures provide back the previous results for the symmetric solution model, they provide complicated results for asymmetric models that are amenable to computer solutions but not the simplified graphs as shown here.

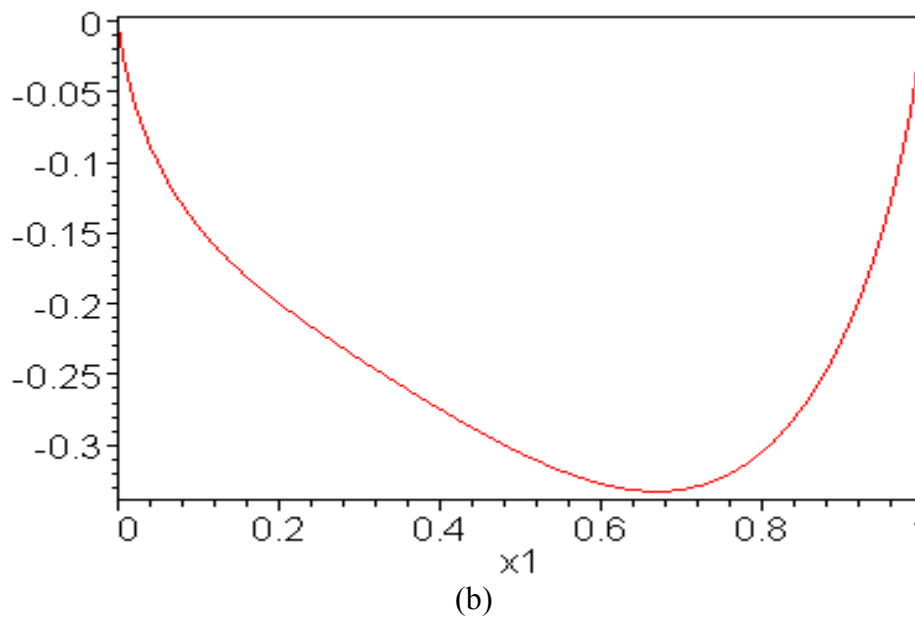
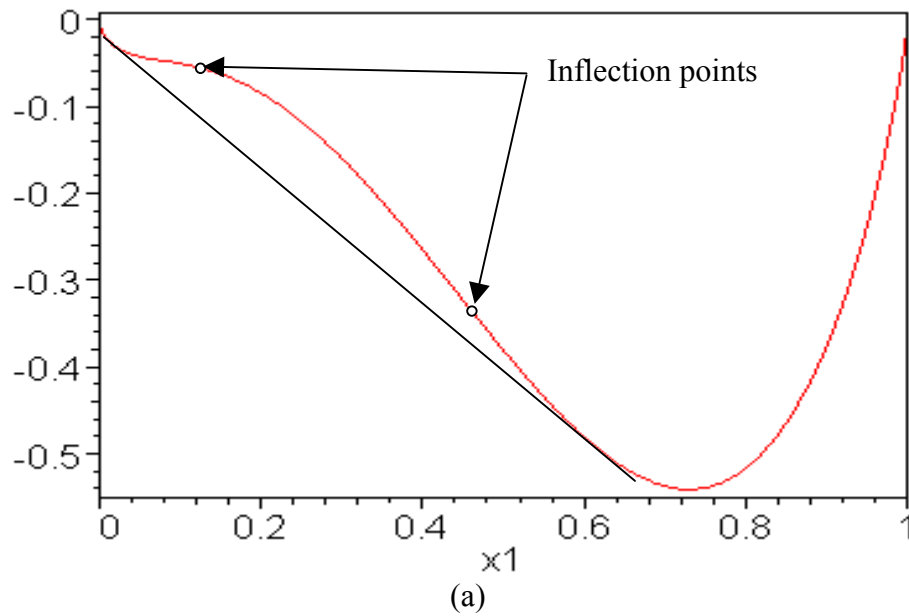


**Figure III.5. Curve of function  $g$  vs  $x_1$  by Margules two-constant model: (a)  $A_{12} = 3.5$  and  $A_{21} = -1$  which show an immiscibility gap bound by the two tangent points and outside the two inflection points; (b)  $A_{12} = 2.1$ ,  $A_{21} = 1$  which does not show any inflection point thus no phase splitting.**

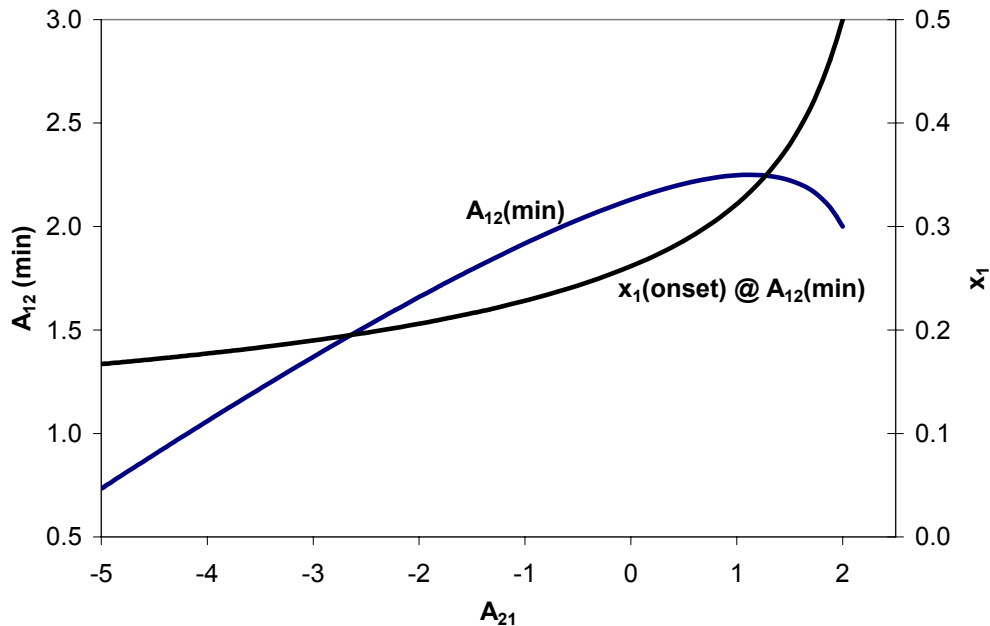


**Figure III.6. Margules (two-constant) locus lines for liquid-liquid phase splitting with  $A_{12} > A_{21}$ .  $A_{12}(\text{min})$  is the minimum value of  $A_{12}$  for which the single-phase liquid splits into two liquid phases for a given value of  $A_{21}$ .  $x_1(\text{onset})$  is the mole fraction at which this splitting first occurs at  $A_{12}(\text{min})$ .**

### *Homogeneous Azeotropes*

Eq. III.3 applied to Eq. III.13 results in the following quadratic equation:

$$3(r-1)x_1^2 - 2(2r-1)x_1 + (\tau + r) = 0 \quad (\text{III.19})$$

where  $x_1 = x_1^{\text{AZ}}$  and  $\tau \equiv \ln(P_1^\sigma/P_2^\sigma)/A_{21}$ .

The new parameter  $\tau$  is the ratio seen in Eq. III.11 for the simplified case of the two Margules constants being the same which collapses into the Symmetric Solution Model at  $A_{12} = A_{21} = A$ . We arbitrarily chose to divide by the lower value of  $A_{21}$  rather than  $A_{12}$  for consistency with our definition of  $r$ . Some combined parameter of this type

is required if the results are to be presented on two-dimensional graphs with  $r$  and  $\tau$  as the coordinates. Note that the vapor pressure of the first component may be higher or lower than that of the second component as we are selecting component 1 so that  $A_{12} > A_{21}$ .

A close examination of the solution of Eq. III.19) reveals that  $\tau = \tau_{\text{MIN}} = -r$  when  $x_1 = 0$  and  $\tau = \tau_{\text{MAX}} = 1$  when  $x_1 = 1$ . These results may be compared with Eq. III.11 where  $-1 \leq \tau \leq 1$  for the symmetric solution where  $r = 1$ . The solution of Eq. III.19 is complex when  $[-2(2r-1)]^2 - 4[3(r-1)](\tau+r) < 0$  or  $3(r-1)(\tau+r) > (2r-1)^2$ . Solving this inequality we obtain

$$\tau_M = \frac{r^2 - r + 1}{3(r-1)} \quad (\text{III.20})$$

To see if a homogeneous azeotrope occurs and the characteristics of the azeotrope, we need to solve Eq. III.19 for real solutions of  $x_1$  which meets the condition of  $0 < x_1 < 1$ . Alternatively, by substituting the expressions of  $\gamma_i$  from Eq. III.13 into Eq. III.2 to get

$$\begin{aligned} P^{\text{BP}} = & P_1^\sigma x_1 \exp\{x_2^2 [A_{12} + 2(A_{21} - A_{12})x_1]\} \\ & + P_2^\sigma x_2 \exp\{x_1^2 [A_{21} + 2(A_{12} - A_{21})x_2]\} \end{aligned} \quad (\text{III.21})$$

and then substitute for  $A_{21} = \ln(P_1^\sigma/P_2^\sigma)/\tau$  and  $A_{12} = A_{21}r$ , we can plot the graph of  $P^{\text{BP}}$  vs  $x_1$  to check the change of the bubble-point pressure vs the variations of  $r$  and  $\tau$ . This can also tell us if an azeotrope exists and how it looks like. Here we plot the curves of  $\tau = -r$ ,  $\tau = 1$  and Eq. III.20 on the  $\tau$  vs  $r$  graph as shown on Figure III.7 as below. Combining this figure with Eq. III.21 we find that between the straight lines of  $\tau = -r$  and  $\tau = 1$   $P^{\text{BP}}$  has a maximum for  $r < -1$  and a minimum for  $-1 < r < 1$  and again a

maximum for  $r > 1$  as better seen on the figure. These correspond (Rowlinson and Swinton, 1982) to positive azeotropes (minimum boiling-point azeotropes) followed by negative azeotropes (maximum boiling-point azeotropes) followed again by positive azeotropes. The regions outside these lines on Figure III.7 are more complicated and interesting. In Eq. III.20  $\tau_M$  is the maximum value of  $\tau$  for  $r < 1$  but its minimum value for  $r > 1$  each defining a region of complex solutions of Eq. III.19 as shown on Figure III.7. If we set the values of  $r$  and  $\tau$  to fall into these regions and plot the graph of  $P^{\text{BP}}$  vs  $x_1$ , we find these complex solution regions contain no azeotropes.

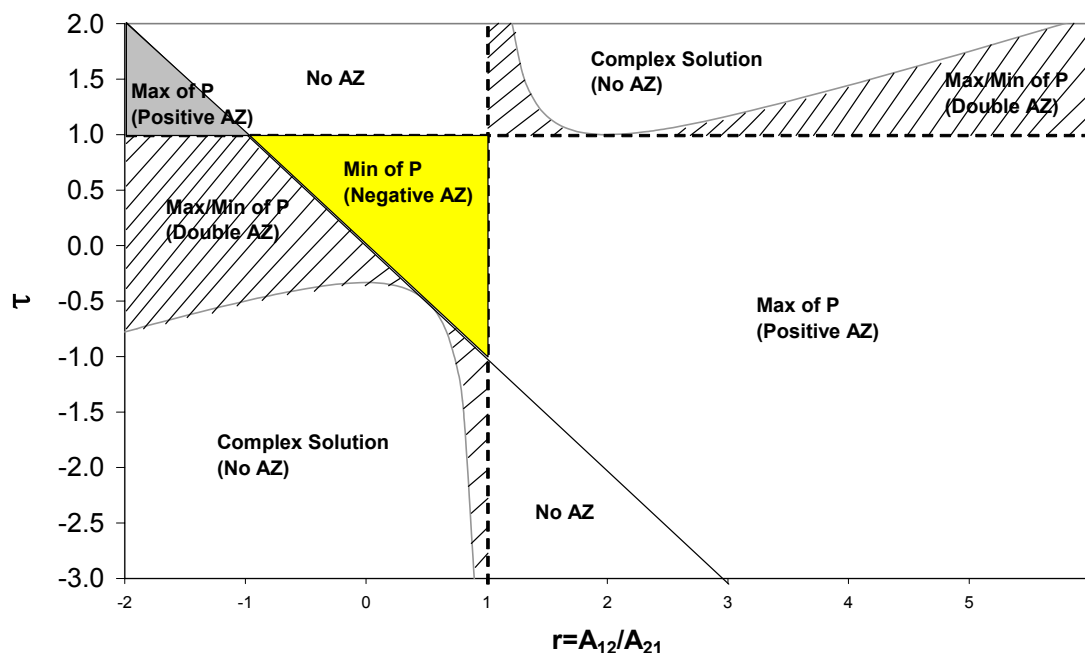


**Figure III.7. Margules (two-constants) regions for the formation of single and double azeotropes with  $A_{12} > A_{21}$ . Here  $\tau \equiv \ln(P_1^\sigma/P_2^\sigma)/A_{21}$ . The regions where double azeotropes occur are hatched.**



Likewise, there are no azeotrope in the regions marked *No AZ* on Figure III.7 but there are two regions where double azeotrope occur marked *Max/Min of P* (Positive/Negative Azeotrope) depending on which azeotrope appears first with increasing  $x_1$ . Double azeotropy is rare in nature usually occurring near a Bancroft point (where the pure-component vapor pressure curves cross or, here, where  $\tau$  is zero). The Margules model is forecasting a Positive/Negative azeotrope for  $r < 0.5$  depending on  $\tau$ . When  $\tau$  is near zero,  $r$  is less than zero or  $A_{21} < 0$  while  $A_{12} > 0$ ; thus Margules constants of opposite signs can lead to a double-azeotrope forecast whenever  $\tau$  is roughly in the range of ( $\sim -0.4, 1$ ). Likewise, when both Margules constants are positive with  $r > 2$ , a Positive/Negative azeotrope is forecast when  $\tau$  is slightly above unity as seen better on Figure III.7. See Rowlinson and Swinton (1982) and, especially, van Konynenburg (1968) for more details about double azeotropy.

### Van Laar Model

This model is expressed as

$$G^E/RT = \frac{x_1 x_2}{x_1/\beta + x_2/\alpha} \quad (\text{III.22})$$

with the activity coefficients shown below:

$$\ln \gamma_1 = \alpha \left[ \frac{x_2}{x_2 + (\alpha/\beta)x_1} \right]^2 \quad (\text{III.23a})$$

$$\ln \gamma_2 = \beta \left[ \frac{x_1}{x_1 + (\beta/\alpha)x_2} \right]^2, \quad (\text{III.23b})$$

$$\ln \gamma_1^\infty = \alpha; \quad \ln \gamma_2^\infty = \beta \quad (\text{III.23c})$$

Consistent with the Margules analysis above, we choose the first component to be the one for which  $\alpha \geq \beta$  in the van Laar model. This defines a parameter  $r \equiv \alpha/\beta$  such that (1)  $r > 1$  when both constants  $\alpha$  and  $\beta$  are positive, (2)  $0 < r < 1$  when both constants are negative and (3)  $r < 0$  only when the first constant is positive and the second is negative. Again all three phenomena listed in Chapter I can be described and forecast in terms of  $r$ . Details presented in the Margules section are not repeated here where we concentrate on what is different between Margules and van Laar. The results follow exactly the sequence of the previous Margules analysis.

### ***Extrema and Inflection Points***

The first and second derivatives of  $\ln\gamma_i$  of Eq. III.23 vs  $x_1$  are shown as below:

$$\frac{\partial \ln\gamma_1}{\partial x_1} = \frac{-2\alpha x_2}{[x_2 + (\alpha/\beta)x_1]^2} - \frac{2\alpha x_2^2(-1 + \alpha/\beta)}{[x_2 + (\alpha/\beta)x_1]^3} \quad (\text{III.24a})$$

$$\frac{\partial \ln\gamma_2}{\partial x_1} = \frac{2\beta x_1}{[x_1 + (\beta/\alpha)x_2]^2} - \frac{2\beta x_1^2(1 - \beta/\alpha)}{[x_1 + (\beta/\alpha)x_2]^3} \quad (\text{III.24b})$$

and

$$\frac{\partial^2 \ln\gamma_1}{\partial x_1^2} = \frac{2\alpha}{[x_2 + (\alpha/\beta)x_1]^2} + \frac{8\alpha x_2(-1 + \alpha/\beta)}{[x_2 + (\alpha/\beta)x_1]^3} + \frac{6\alpha x_2^2(-1 + \alpha/\beta)^2}{[x_2 + (\alpha/\beta)x_1]^4} \quad (\text{III.24c})$$

$$\frac{\partial^2 \ln\gamma_2}{\partial x_1^2} = \frac{2\beta}{[x_1 + (\beta/\alpha)x_2]^2} - \frac{8\beta x_1(1 - \beta/\alpha)}{[x_1 + (\beta/\alpha)x_2]^3} + \frac{6\beta x_1^2(1 - \beta/\alpha)^2}{[x_1 + (\beta/\alpha)x_2]^4} \quad (\text{III.24d})$$

By setting Eqs. III.24 a & b above to zero and solving them we find that there is only one trivial solution  $x_1 = 1$  for  $\partial \ln\gamma_1/\partial x_1 = 0$  and one trivial solution  $x_1 = 0$  for  $\partial \ln\gamma_2/\partial x_1 = 0$ . That means that the van Laar model provides no extrema for  $\ln\gamma_1$  and

$\ln\gamma_2$  vs  $x_1$  except the trivial cases required by Eq. I.5) for  $x_1 = 0$  (for  $\ln\gamma_2$ ) and for  $x_1 = 1$  (for  $\ln\gamma_1$ ).

To find the inflection points we let  $\partial \ln^2\gamma_1 / \partial x_1^2 = 0$  and  $\partial \ln^2\gamma_2 / \partial x_1^2 = 0$ . Solve these two equations and substitute for  $r = \alpha/\beta$  we obtain the inflection points for  $\ln\gamma_1$  and  $\ln\gamma_2$ , respectively, as follows:

$$x_1^{\text{IP1}} = \frac{3r-2}{2(r-1)} \text{ and } x_1^{\text{IP2}} = \frac{1}{2(r-1)} \quad (\text{III.25})$$

Subjecting Eq. III.25 to the restriction condition of  $0 < x_1 < 1$  we find that an inflection point can exist for  $\ln\gamma_1$  only when  $0 < r < 2/3$ . For  $\ln\gamma_2$  an inflection point only exists when  $r > 1.5$ . Graphs of  $x_1^{\text{IP1}}$  and  $x_1^{\text{IP2}}$  vs  $r$  are shown on Figure III.8.

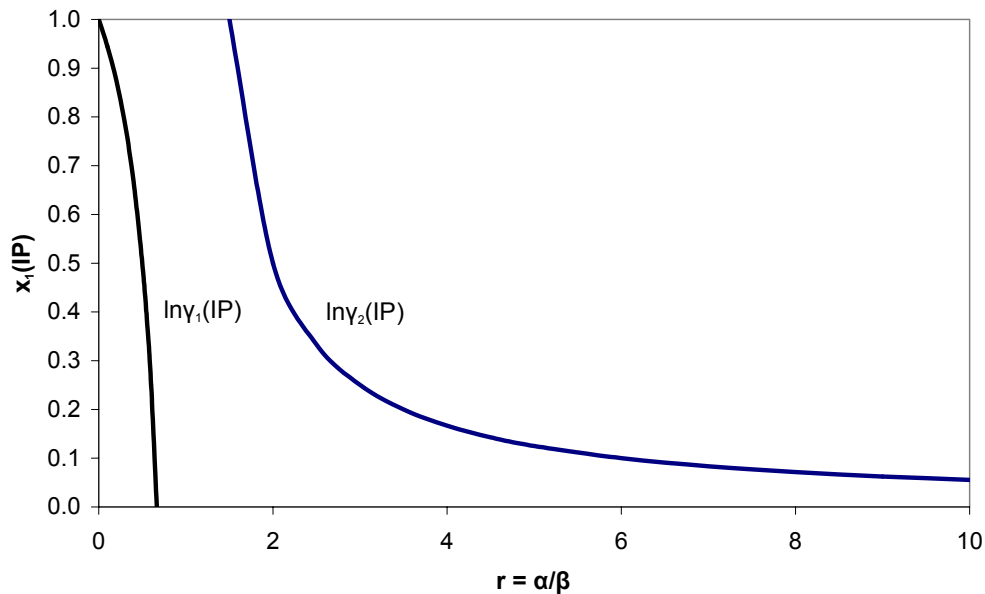


**Figure III.8.** van Laar locus lines for inflection points on  $\ln\gamma_i$  vs  $x_1$  graphs with  $\alpha > \beta$ .

### ***Liquid-liquid Phase Splitting***

Similar to the analysis for Margules two-constant model, the onset of phase splitting for van Laar model must also meet the criteria of  $g'' = 0$  and  $g''' = 0$ , where  $g = \Delta_m G/RT = x_1 \ln x_1 + x_2 \ln x_2 + G^E/RT$ . Take the second and third derivatives of  $g$  vs  $x_1$  and set them to zero we have:

$$g'' = \frac{1}{x_1 x_2} - \frac{2}{x_1/\beta + x_2/\alpha} + \frac{2(2x_1 - 1)(1/\beta - 1/\alpha)}{(x_1/\beta + x_2/\alpha)^2} + \frac{2x_1 x_2 (1/\beta - 1/\alpha)^2}{(x_1/\beta + x_2/\alpha)^3} = 0 \quad (\text{III.26a})$$

$$g''' = \frac{2x_1 - 1}{(x_1 x_2)^2} + \frac{6(1/\beta - 1/\alpha)}{(x_1/\beta + x_2/\alpha)^2} - \frac{6(2x_1 - 1)(1/\beta - 1/\alpha)^2}{(x_1/\beta + x_2/\alpha)^3} - \frac{6x_1 x_2 (1/\beta - 1/\alpha)^3}{(x_1/\beta + x_2/\alpha)^4} = 0 \quad (\text{III.26b})$$

Through proper manipulations we can obtain from the above equations

$$x_1(\text{onset}) = \frac{-r + \sqrt{r^2 - r + 1}}{(1 - r)} \quad (\text{III.27})$$

A close examination of  $x_1(\text{onset})$  reveals that it is a continuous and monotonically decreasing function versus variable  $r$ .  $x_1(\text{onset}) = 1$  at  $r = 0$  and  $\lim_{r \rightarrow 1} x_1(\text{onset}) = 0.5$ .  $x_1(\text{onset})$  approaches zero when  $r$  approach positive infinity. Thus we can plot the graph of  $x_1(\text{onset})$  vs  $r$  as shown on Figure III.9.

Substitute  $x_1(\text{onset})$  from Eq. III.27 and  $\beta = \alpha/r$  into Eq. III.26 to solve for  $\alpha = \alpha(\text{min})$  for a given value of  $r$  we obtain:

$$\alpha(\text{min}) = \frac{rx_1 + (1 - x_1)}{2x_1(1 - x_1)[1 + (1 - 2x_1)\psi - x_1(1 - x_1)\psi^2]} \quad (\text{III.28})$$

where

$$\psi = \frac{r-1}{1+(r-1)x_1} \text{ and } x_1 = x_1(\text{onset}).$$

The graph of  $\alpha(\text{min})$  vs  $r$  is also plotted on Figure III.9. From this figure it is easy to tell whether a liquid-liquid phase splitting occurs for a given set of values of  $\alpha$  and  $\beta$ . That is, for a certain value of  $r = \alpha/\beta$  the condition of  $\alpha \geq \alpha(\text{min})$  must be met for a liquid-liquid phase splitting to begin. Once it begins, the immiscibility gap should be within a region centered near  $x_1(\text{onset})$ . Again, the values of the two end-points of the immiscibility gap can be found by applying the tangent line method or, alternatively, the equal-area-rule method (Eubank and Hall, 1995) to the  $g' \equiv dg/dx_1$  vs  $x_1$ .

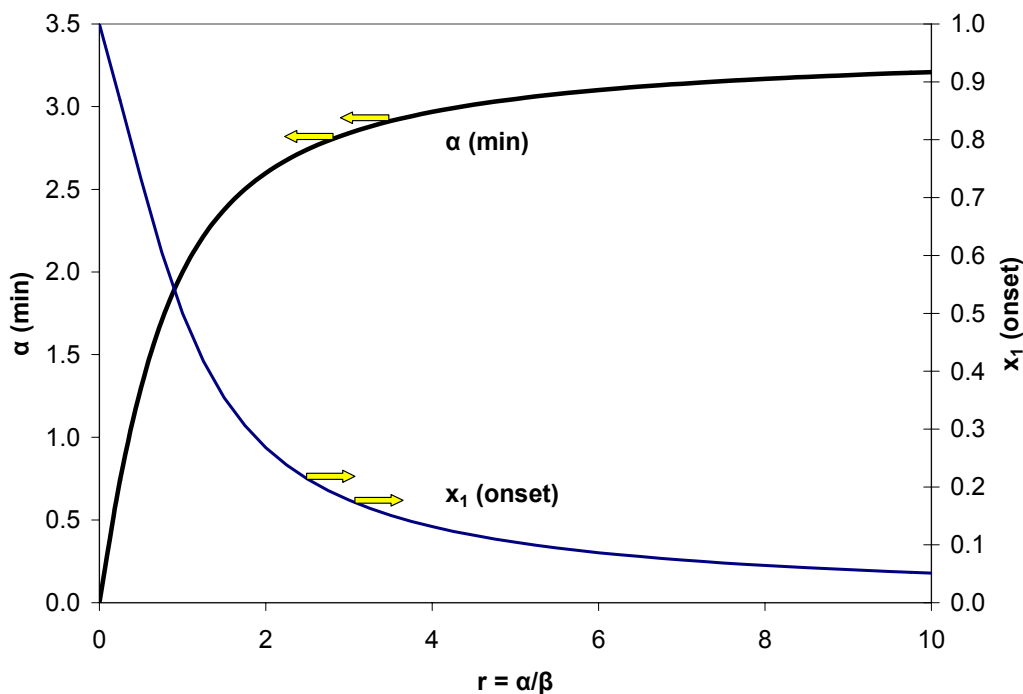


**Figure III.9.** van Laar locus for liquid-liquid phase splitting with  $\alpha > \beta$ .  $\alpha(\text{min})$  is the minimum value of  $\alpha$  for which the single-phase liquid splits into two liquid phases for a given value of  $\beta$ .  $x_1(\text{onset})$  is the mole fraction at which the splitting first occurs at  $\alpha(\text{min})$ .

### Homogeneous Azeotropes

Eq. III.3 applied to Eq. III.23 results in a quadratic equation as shown below:

$$\frac{(\tau + r)(1 - x_1)}{rx_1} = -\tau + \sqrt{(r-1)\tau - r} \quad (\text{III.29})$$

where  $x_1 = x_1^{AZ}$  and  $\tau \equiv \frac{\ln(P_1^\sigma/P_2^\sigma)}{\beta}$ .

The parameter  $\tau$  is analogous to that defined in the case for the Margules model. However, Figure III.10 shows that the results for van Laar are very different from those of Figure III.7 for Margules. While the major division line of  $\tau = -r$  is common, now any negative value of  $r$  produces a divergence of pressure on the  $P$  vs  $x_1$  diagram at  $x_1 = (1 - r)^{-1}$ . Further, there can be no homogeneous azeotropes for  $\tau > 1$ . Thus, Figure III.10 is bounded by  $r = 0$  and  $\tau = 1$  in the upper left corner.

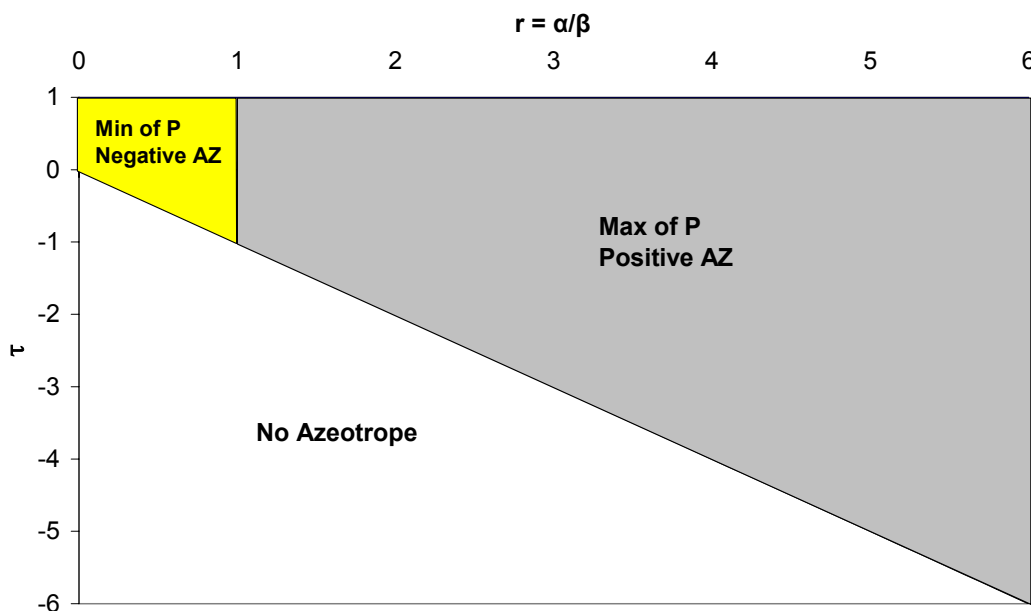


Figure III.10. van Laar regions for the formation of single, homogeneous azeotropes with  $\alpha > \beta$ . Here  $\tau = \ln(P_1^\sigma/P_2^\sigma)/\beta$ .

### NRTL Model

This *non-random, two-liquid* model originated with H. Renon as described by Prausnitz et al. (1999). The equation is:

$$\frac{G^E}{RT} = x_1 x_2 \left[ \frac{\tau_{21} \exp(-\alpha_{12} \tau_{21})}{x_1 + x_2 \exp(-\alpha_{12} \tau_{21})} + \frac{\tau_{12} \exp(-\alpha_{12} \tau_{12})}{x_2 + x_1 \exp(-\alpha_{12} \tau_{12})} \right] \quad (\text{III.30})$$

which results in activity coefficients as below:

$$\ln \gamma_1 = x_2^2 \left\{ \left[ \frac{\sqrt{\tau_{21}} \exp(-\alpha_{12} \tau_{21})}{x_1 + x_2 \exp(-\alpha_{12} \tau_{21})} \right]^2 + \frac{\tau_{12} \exp(-\alpha_{12} \tau_{12})}{[x_2 + x_1 \exp(-\alpha_{12} \tau_{12})]^2} \right\} \quad (\text{III.31a})$$

$$\ln \gamma_2 = x_1^2 \left\{ \left[ \frac{\sqrt{\tau_{12}} \exp(-\alpha_{12} \tau_{12})}{x_2 + x_1 \exp(-\alpha_{12} \tau_{12})} \right]^2 + \frac{\tau_{21} \exp(-\alpha_{12} \tau_{21})}{[x_1 + x_2 \exp(-\alpha_{12} \tau_{21})]^2} \right\} \quad (\text{III.31b})$$

As seen, the NRTL model has three parameters ( $\tau_{12}$ ,  $\tau_{21}$  and  $\alpha_{12}$ ), but  $\alpha_{12}$ , a measure of non-randomness of the mixture, is generally found to be between 0.2 and 0.47, with 0.3 as a typical value. When  $\alpha_{12} = 0$ , the model reduces to a symmetric model. This model is considered to be especially valuable for highly nonideal solutions that lead to phase splitting. Renon and Prausnitz (1969) provided graphs for determination of NRTL parameters from immiscibility data and from infinite dilution activity coefficients. Here we provide essentially the opposite result – given a set of NRTL parameters will one see phase splitting, homogeneous azeotropes plus extrema and inflection points for  $\ln \gamma_i$ ? Again we follow the same procedures as above for Margules and van Laar.

### *Extrema and Inflection Points*

By taking the first derivative of Eq. III.31 and set them to zero we obtain the extrema of  $\ln \gamma_1$  and  $\ln \gamma_2$  vs  $x_1$  for the NRTL model as below:

$$x_1^M = \frac{\exp[(2\alpha_{12}/3)(r-1)\tau_{21}] + r^{1/3}\exp(-\alpha_{12}\tau_{21})}{[-1 + \exp(-\alpha_{12}\tau_{21})]\{r^{1/3} - \exp[(2\alpha_{12}/3)(r-1)\tau_{21}]\}} \quad (\text{III.32})$$

where  $r \equiv \tau_{12}/\tau_{21}$  and  $\tau_{12} > \tau_{21}$ .

We hoped to provide graphs similar to Figure III.4 for several fixed values of  $\alpha_{12}$  but Eq. III.32 shows that use of  $r$  is not successful in elimination of the two parameters that make up its ratio as was the case in Margules and van Laar. Extensive tests on a graphing calculator with  $x_1^M$  vs  $r$  for different values of both  $\alpha_{12}$  and  $\tau_{21}$  revealed the following results: (1) there are no extrema for  $r > 0$ , (2) there are no multiple extrema, (3) for  $|\alpha_{12}\tau_{21}| < 0.1$  with  $\tau_{21} < 0$ , extrema tend to appear near  $r = -1$ , (4) for  $0.1 < |\alpha_{12}\tau_{21}| < 0.25$  with  $\tau_{21} < 0$ , extrema tend to appear over a range of  $r = (-11, -1)$  and (5) for  $|\alpha_{12}\tau_{21}| > 0.25$  the extrema disappear. These results are valid for  $\alpha_{12} = 0.3$  but are only approximations for deviations from this average value of  $\alpha_{12}$ . Eq. III.32 shows that the product  $\alpha_{12}\tau_{21}$  can be combined into a new parameter  $\eta = \alpha_{12}\tau_{21}$  so  $x_1^M$  is a function of  $(\eta, r)$ , but the range of  $\eta$  is far wider than of  $\alpha_{12}$ .

By taking the second derivatives of Eq. III.31 and set them to zero we obtain the equations for the inflection points. For  $\ln\gamma_1$  the equation is

$$\frac{2x_2[\exp(-\eta)-1]-1}{-2x_2+(2x_2+1)\exp(-\eta r)} = r \left[ \frac{x_1+x_2\exp(-\eta)}{x_2+x_1\exp(-\eta r)} \right]^4 \exp[-2(r-1)\eta]. \quad (\text{III.33})$$

and for  $\ln\gamma_2$  this is

$$\frac{2x_1[1-\exp(-\eta)]+\exp(-\eta)}{1+2x_1[1-\exp(-\eta r)]} = r \left[ \frac{x_1+x_2\exp(-\eta)}{x_2+x_1\exp(-\eta r)} \right]^4 \exp[-(2r-1)\eta]. \quad (\text{III.34})$$



Once again it is not practical to provide graphs for this result as was done for Margules and van Laar. Testing with a graphing calculator shows that NRTL can provide both single and double inflection points allowing considerable flexibility in tuning to experiment. While it can provide single points as shown in Figure III.3a, NRTL, unlike Margules and van Laar, can provide double inflection points on the same graph of  $\ln\gamma_1$  and  $\ln\gamma_2$  vs  $x_1$ . For example, when  $\eta = 1.1$  and  $r = 1.75$ , there are inflection points in  $\ln\gamma_1$  at  $x_1 = 0.6610$  and  $0.9082$  with all values of  $\gamma_1$  above unity.

### ***Liquid-liquid Phase Splitting***

As with the Margules and van Laar models, we examine the function  $g = \Delta_m G/RT = x_1 \ln x_1 + x_2 \ln x_2 + G^E/RT$  vs  $x_1$  for phase splitting. At the onset of phase splitting the condition of  $g'' = g''' = 0$  must be met. Differentiate  $g$  vs  $x_1$  and set the derivatives to zero we obtain the following equations:

$$\begin{aligned}
 g'' &= \frac{1}{x_1 x_2} - \frac{2\tau_{21} \exp(-\alpha_{12} \tau_{21})}{x_1 + x_2 \exp(-\alpha_{12} \tau_{21})} - \frac{2\tau_{12} \exp(-\alpha_{12} \tau_{12})}{x_2 + x_1 \exp(-\alpha_{12} \tau_{12})} \\
 &+ 2(1 - 2x_1) \left\{ -\frac{\tau_{21} \exp(-\alpha_{12} \tau_{21}) [1 - \exp(-\alpha_{12} \tau_{21})]}{[x_1 + x_2 \exp(-\alpha_{12} \tau_{21})]^2} - \frac{\tau_{12} \exp(-\alpha_{12} \tau_{12}) [-1 + \exp(-\alpha_{12} \tau_{12})]}{[x_2 + x_1 \exp(-\alpha_{12} \tau_{12})]^2} \right\} \\
 &+ x_1 x_2 \left\{ \frac{2\tau_{21} \exp(-\alpha_{12} \tau_{21}) [1 - \exp(-\alpha_{12} \tau_{21})]^2}{[x_1 + x_2 \exp(-\alpha_{12} \tau_{21})]^3} + \frac{2\tau_{12} \exp(-\alpha_{12} \tau_{12}) [-1 + \exp(-\alpha_{12} \tau_{12})]^2}{[x_2 + x_1 \exp(-\alpha_{12} \tau_{12})]^3} \right\} \\
 &= 0
 \end{aligned}$$

(III.35)

and

$$\begin{aligned}
g''' &= \frac{2x_1 - 1}{(x_1 x_2)^2} - \frac{6\tau_{21} \exp(-\alpha_{12} \tau_{21}) [1 - \exp(-\alpha_{12} \tau_{21})]}{[x_1 + x_2 \exp(-\alpha_{12} \tau_{21})]^2} - \frac{6\tau_{12} \exp(-\alpha_{12} \tau_{12}) [-1 + \exp(-\alpha_{12} \tau_{12})]}{[x_2 + x_1 \exp(-\alpha_{12} \tau_{12})]^2} \\
&+ 6(1 - 2x_1) \left\{ \frac{\tau_{21} \exp(-\alpha_{12} \tau_{21}) [1 - \exp(-\alpha_{12} \tau_{21})]^2}{[x_1 + x_2 \exp(-\alpha_{12} \tau_{21})]^3} + \frac{\tau_{12} \exp(-\alpha_{12} \tau_{12}) [-1 + \exp(-\alpha_{12} \tau_{12})]^2}{[x_2 + x_1 \exp(-\alpha_{12} \tau_{12})]^3} \right\} \\
&- 6x_1 x_2 \left\{ \frac{\tau_{21} \exp(-\alpha_{12} \tau_{21}) [1 - \exp(-\alpha_{12} \tau_{21})]^3}{[x_1 + x_2 \exp(-\alpha_{12} \tau_{21})]^4} + \frac{\tau_{12} \exp(-\alpha_{12} \tau_{12}) [-1 + \exp(-\alpha_{12} \tau_{12})]^3}{[x_2 + x_1 \exp(-\alpha_{12} \tau_{12})]^4} \right\} \\
&= 0
\end{aligned}
\tag{III.36}$$

A ratio of these two equations results in complex relations between the ratio  $r \equiv \tau_{12}/\tau_{21}$  and  $x_1$  (onset) for a fixed value of  $\alpha_{12}$ . While these relations are too complex to be shown here, the positive side is that  $r$  is successful in elimination of the two parameters that make up its ratio for the case of phase splitting. Thus graphs of  $\tau_{21}$  (max) vs  $r$  can be prepared with  $\alpha_{12}$  as parameter. Phase splitting does not occur for  $-2 < r < 1$  but can occur when both  $\tau_{12}$  and  $\tau_{21}$  are positive or when the first parameter ( $\tau_{12}$ ) is positive and the second ( $\tau_{21}$ ) negative. For the latter case, Figure (III.11a) shows the single and two liquid phase regions for  $r < -2$ . Here the value of  $\alpha_{12}$  has only a slight effect on phase splitting so a single curve is shown to represent both  $\alpha_{12} = 0.3$  and  $0.45$ . Generally speaking, a higher value of  $\alpha_{12}$  causes the curve of Figure III.11a to be lowered but for a given value of  $r$  the relation between  $\tau_{21}$  (max) and  $\alpha_{12}$  is not always monotonic. Except in rare examples, the reader will not be misled in using the curve of Figure III.11a for all values of  $\alpha_{12}$ .

When both  $\tau_{12}$  and  $\tau_{21}$  are positive, Figure III.11b shows that  $\alpha_{12}$  has a significant effect upon phase splitting. Here we have included a curve for  $\alpha_{12} = 0.6$ ,

although this value is higher than usually encountered. For  $\alpha_{12} = 0$  corresponding to the symmetric model, the curve follows  $(r+1)\tau_{21}(\max) = 2$  and thus passes through (1, 1), (3, 0.5) and (5, 1/3) for  $[r, \tau_{21}]$ . This will aid the reader in interpolation for  $0 < \alpha_{12} < 0.3$ .

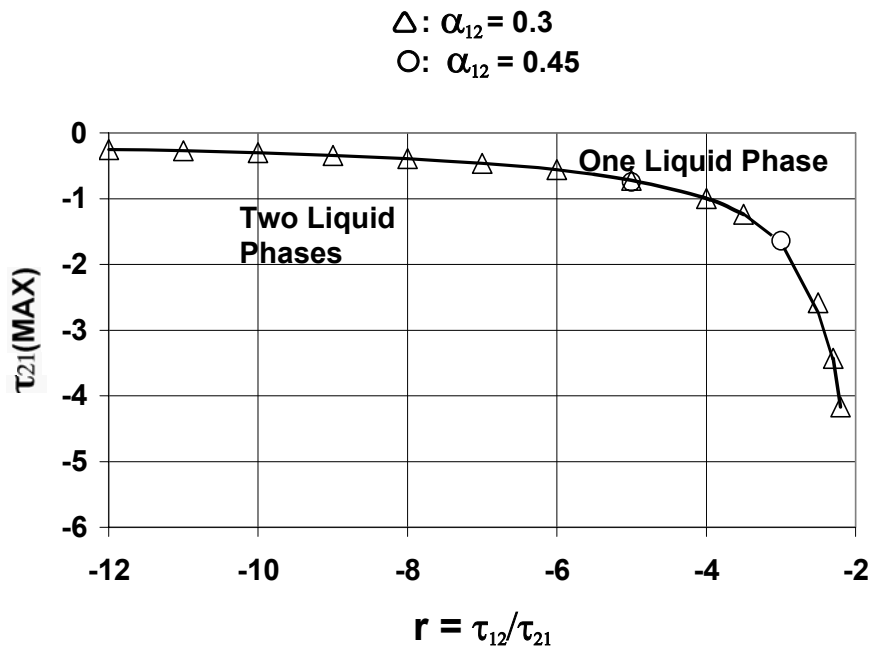


Figure III.11a. NRTL locus for liquid-liquid phase splitting with  $\tau_{12} > 0$  and  $\tau_{21} < 0$ .

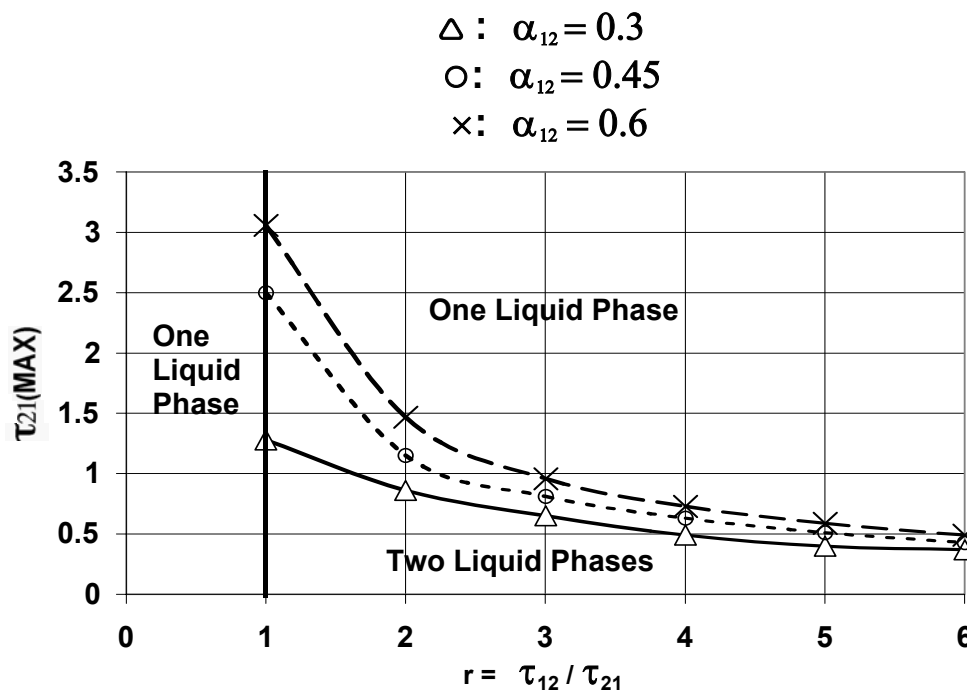


Figure III.11b. NRTL locus for liquid-liquid phase splitting with  $\tau_{12} > 0$  and  $\tau_{21} > 0$ .

### *Homogeneous Azeotropes*

Eq. III.3 applied to Eq. III.31 results in  $P$  vs  $x_1$  diagrams with parameters of  $r$ ,  $\eta$  and  $\tau$ . Previous Figures (III.7 & III.10) would now require another dimension  $\eta$ . Again with very complex equations we turn to the graphing calculator which shows a wealth of examples of homogeneous azeotropes, both positive and negative, for the NRTL model. Double azeotropes of both the Max/Min and Min/Max type are observed. Triple azeotropes can be found but these cases, as always, should be checked first for phase splitting, to make sure that the azeotropic composition does not fall in the liquid-liquid gap.

## CHAPTER IV

### PYROLYSIS OF NATURAL GAS:

#### REVIEW AND METHODOLOGY FOR KINETIC SIMULATION

##### **Current Technologies of Converting Natural Gas to Liquids**

Liquefaction is the most primary method of converting natural gas to liquid. It is a purely physical process. In this process, natural gas is liquefied by cooling to its boiling point of  $-161\text{ }^{\circ}\text{C}$  ( $-259\text{ }^{\circ}\text{F}$  or  $113\text{ }^{\circ}\text{K}$ ) at atmospheric pressure. Because the liquefied natural gas (LNG) occupies only 1/600th the volume of natural gas at atmospheric temperature and pressure and has much higher energy density, it can be readily transported and stored in refrigerated, double-walled and vacuum-insulated tankers. Upon arrival at the end customers, it is again converted back to gas state in revaporization terminals. Traditional liquefaction process requires rather sophisticated compression and refrigeration machinery. A typical modern, large liquefaction plant costs a billion dollars, liquefies  $10^9$  scfd, uses 10-15% of its throughput to power itself, and has substantial operating and maintenance costs (Parkyns et al., 1993). Thus scientists and engineers have never stopped the effort to seek smaller-scale, simpler and cheaper technologies to liquefy natural gas. Recently Wollan et al. (2002) reported using thermoacoustic heat engines and refrigerators for liquefaction of natural gas, which is the only current technology capable of producing refrigeration power at cryogenic temperatures with no moving parts. This process has such advantages as low manufacturing cost, high reliability, long life, and low maintenance. Another new technology was reported to have been invented by the Pacific Gas and Electric Company (PG&E) ([www.globaltechnoscan.com](http://www.globaltechnoscan.com)). Their new

small-scale natural gas liquefaction facility “is expected to revolutionize the liquefaction industry”, and can cut the cost of a standard LNG plant from about \$10 million to \$450,000 and makes it possible to shrink the size needed for such a facility from five or six acres to about 240 square feet.

In addition to physical liquefaction, natural gas can also be chemically converted to higher hydrocarbons through various direct or indirect methods. Direct methods converts methane directly into desired end products (Renesme et al., 1992), indirect methods first converts methane into intermediate products such as synthesis gas (or syngas,  $\text{CO} + \text{H}_2$ ), then converts syngas to final products through different chemical pathways. Below we will give a brief summary to the typical processes currently available.

### **Direct Conversion**

Methane can be directly converted into ethylene, acetylene, methanol (MeOH) or other liquid fuels through oxidation on highly selective catalysts. As direct conversion bypasses the costly production of synthesis gas, they are less costly than the indirect conversion approach. However, direct conversion is far from being technically feasible (Aasberg-Petersen et al., 2001). The direct conversion to methanol may reach high selectivity ( $\sim 80\%$ ), but its conversion per pass is so low that the yield per pass is only about 7%. This leads to large reflux ratio and difficult separation due to the low partial pressure of the product. Other factors in addition to the selectivity and conversion should also be considered. For example, the Catalytica process (Periana et al., 1998) for converting methane via methyl bi-sulphate into MeOH has the potential of achieving a

high selectivity of 95% at a conversion of 90%. However, the process requires a large sulphuric acid plant ( $\text{SO}_2:\text{MeOH} = 1:1$ ) and a unit for concentrating a large recycle of diluted acid. Thus very expensive equipment will be required to handle the highly corrosive sulphuric acid and the process was unlikely to become economic. The process was finally abandoned by Catalytica.

Mossaad (2002) gave a brief yet excellent review about these direct conversion methods in his Ph.D. dissertation. The major types of direct conversion of methane include partial oxidation, oxidative coupling and oxyhydrochlorination. These processes lead to different end products.

### ***Partial Oxidation to Methanol***

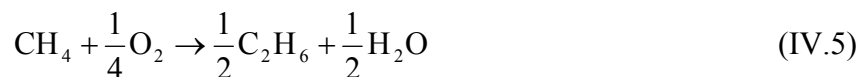
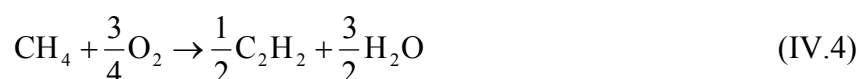
This process uses various oxidants such as air, pure oxygen or nitrous oxides  $\text{N}_x\text{O}_y$  to directly oxidize methane to methanol. Associated byproducts like  $\text{CO}_2$  may also exist due to complete oxidation of  $\text{CH}_4$ . Main reactions involved in this process are as follows (Foster, 1985; Okumoto et al., 2001):



Both the conversion (~10% maximum) and the selectivity are very low for this process. Further, use of pure oxygen requires costly production facility while use of air or nitrous oxides is cheap but will introduce large volume of nitrogen which is useless but will substantially need more equipment space and energy to handle it. Thus, this process is both technically and economically unfeasible (Stiegel, 1994).

### ***Oxidative Coupling to Ethylene***

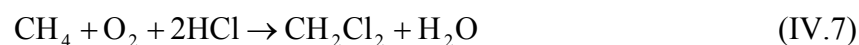
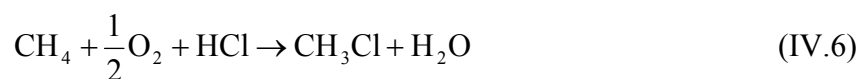
This process catalytically converts methane into ethylene and other hydrocarbons in an oxidative ambient environment. The reactions shown below are carried out at approximately 800 °C (Bistolfi et al., 1992). To avoid deep oxidation into CO and CO<sub>2</sub>, highly selective catalysts are required. Two types of catalysts are used for this purpose. The first type is some transition metal oxides, and the second type is catalysts of combined alkali and alkaline earth oxides.



Similar to the partial oxidation to methanol process, the conversion of this process is also very low (~10%). Together with the high cost of producing pure oxygen, these factors render the approach uneconomic.

### ***Oxyhydrochlorination***

This process directly converts methane into methyl chloride, which can then be used as a refrigerant and catalyst solvent in butyl rubber production, or be converted into aromatic-rich hydrocarbons with zeolite catalysts. The reactions are carried out by mixing methane, oxygen and hydrogen chloride at 250 °C with the existence of zeolite catalysts:



This method has better methane conversion and product selectivity than the previous two direct conversion methods. However, safety concerns and the special



requirements for equipment to handle the highly corrosive HCl prevents its commercial application. As with the previous two methods, lack of highly selectively catalysts is another major obstacle for the commercialization of the process.

### **Indirect Conversion of Methane**

The indirect conversion approach first converts methane to synthesis gas (CO + H<sub>2</sub>), this intermediate gas mixture is then converted to various liquid fuel products such as methanol, gasoline or other chemicals through the famous Fisher – Tropsch (F-T) process. The syngas routes are highly efficient but capital intensive (Aasberg-Petersen et al., 2001) because they involve huge amount of heat exchange in the reactors and heat recovery units. Currently there are three major types of indirect conversion, which are steam reforming, autothermal reforming and catalytic partial oxidation, respectively.

#### ***Steam Reforming***

Steam reforming (SMR) process was developed in 1926, and has received many improvements in its technology over the years since its first industrial application. A typical steam reforming process can be shown in Figure IV.1 (Satterfield, 1991; Twigg, 1989).

Here in the primary reformer, methane reacts with steam over a Ni/ Al<sub>2</sub>O<sub>3</sub> catalyst at a temperature of 900 °C and a pressure of 15-30 atm with a residence time of several seconds. The reaction is highly endothermic as shown below:



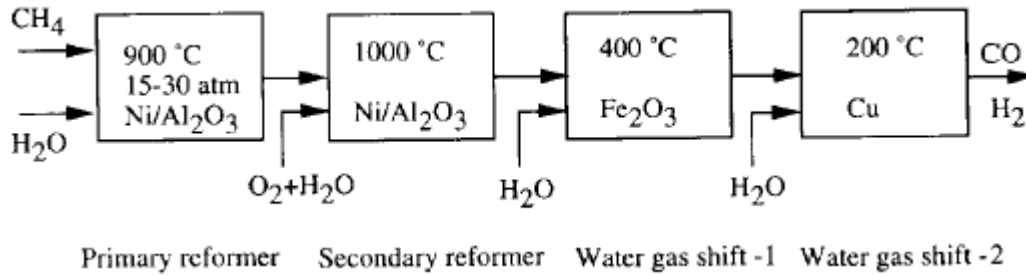


**Figure IV.1. Block diagram for conventional steam reforming:** CH<sub>4</sub> and excess H<sub>2</sub>O are reacted in a primary reformer over Ni/Al<sub>2</sub>O<sub>3</sub> at 900 °C. The unconverted CH<sub>4</sub> (8-10%) is reacted with O<sub>2</sub> and more H<sub>2</sub>O in a second reformer to give equilibrium CO and H<sub>2</sub>. The product H<sub>2</sub>/CO ratio is then modified in two water gas shift stages.

Excess steam (H<sub>2</sub>O:CH<sub>4</sub> = 2~6) is often used to prevent carbon formation. The methane conversion at the exit of the primary reformer is typically 90~92% (Bharadwaj et al., 1995).

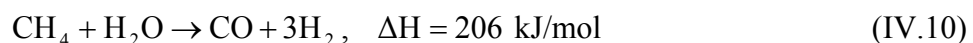
In the second reformer remaining CH<sub>4</sub> is reacted O<sub>2</sub>, producing CO<sub>2</sub> and water and evolving huge amount of heat. This heat is used to produce high pressure steam to drive the turbines for the syngas compressor or is directly used to supply energy to the primary reformer.

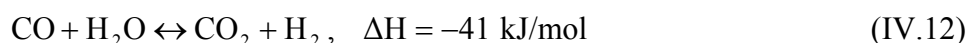
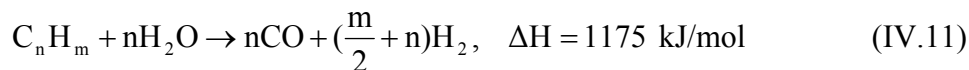
Two water shift reactions are usually applied to adjust the CO/H<sub>2</sub> ratio to its optimal value of 1:2 after the secondary reformer:



The first water shift reaction is carried out at a temperature of 400 °C over iron oxide/chromia catalyst, while the second reaction occurs at a much lower temperature of 200 °C on a copper-based catalyst to attain favorable equilibrium.

Overall reactions of the steam reforming process can be expressed as below:





Although the steam reforming process has seen much progress in recent years, it also has many constraints which limit its wide-spread application. First, thermodynamics require high exit temperatures to achieve relatively high conversion of methane, yet the activity of the catalysts decreases sharply at temperatures above 400°C. Second, the conventional reformer has an energy efficiency of only approximately 50%, which causes large amount of heat loss, making the process less economical. The energy efficiency can be increased to about 80% by using a heat exchanger reformer. However this new type of reactor will incur other problems (Aasberg-Petersen et al., 2001).

### *Autothermal Reforming*

Autothermal reforming (ATR) process is a combination of homogeneous partial oxidation and steam reforming and was first developed in the late 1970s with the aim of carrying out reforming in a single reactor. The process can be schematically shown in Figure IV.2 as below.

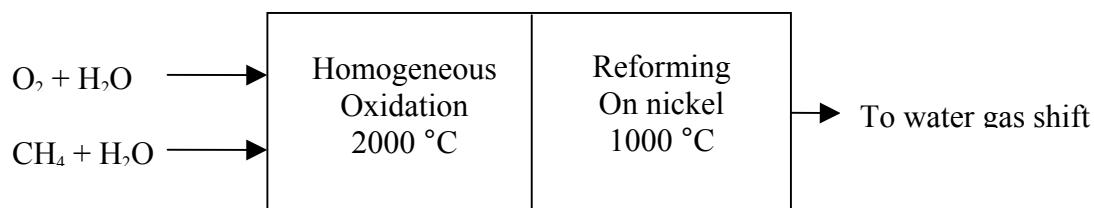
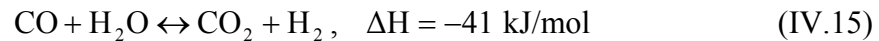
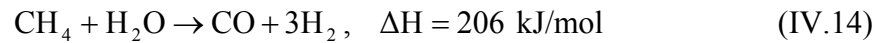
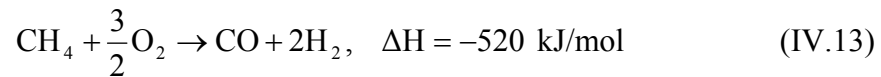


**Figure IV.2. Schematic representation of autothermal reforming: CH<sub>4</sub> is reacted with O<sub>2</sub> in a flame and the products of homogeneous partial oxidation are then reformed by H<sub>2</sub>O in the feed over a Ni catalyst bed. The product synthesis gas composition is then adjusted by water gas shift stages.**

Overall reactions of autothermal reforming process can be expressed as follows:

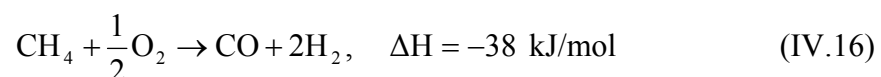


The preheated feed streams ( $\text{O}_2 + \text{H}_2\text{O}$  and  $\text{CH}_4 + \text{H}_2\text{O}$ ) are first mixed and combusted in a burner for partial oxidation at a temperature of around 2000 °C, then the gas stream goes through the nickel catalyst bed for reaction at around 1000 °C to further adjust the  $\text{CO}/\text{H}_2$  ratio. Again, steam is added to the feed streams to prevent carbon formation.

This process also has some problems with it. First, it requires pure oxygen as feed gas which is normally very expensive to produce. Second, carbon formation may occur in the extremely hot combustion leading to damage to both catalysts and equipment.

### ***Catalytic Partial Oxidation (CPO)***

The use of steam in the above two processes (SMR & ATR) brings forth some disadvantages such as (1) endothermic reactions, (2) causing product ratio of  $\text{CO}/\text{H}_2$  to be 1:3, which is away from the optimal ratio of 1:2, (3) steam corrosion problems, and (4) costs in handling excess  $\text{H}_2\text{O}$ . Due to these problems, recent technological trends have been to remove steam from the process systems and adopt some direct “dry” oxidation of methane. In this process,  $\text{CH}_4$  and  $\text{O}_2$  are catalytically converted to syngas according to the following reaction:



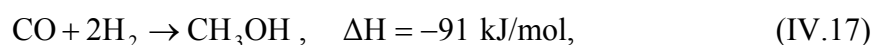
Since this reaction is slightly exothermic, it can occur in a single reactor without a burner, thus the process is much more energy efficient than the energy intensive steam reforming process. The oxidation reactions are also much faster than reforming reactions, leading to smaller reactors and higher throughput. In addition, this process provides the ideal CO/H<sub>2</sub> ratio with H<sub>2</sub> & CO selectivity and CH<sub>4</sub> conversion both above 90%.

However, this process involves the premixing of CH<sub>4</sub> & O<sub>2</sub> which can be flammable or even explosive within certain composition limits, thus it is very difficult to study the reactions. This, plus other problems such as catalyst coking and local hot spots in equipment lead to the fact that this process is very difficult to be commercialized.

From the above review, it is seen that indirect conversion methods have higher methane conversion and product selectivity than the direct conversion. In fact, several processes based on the indirect conversion pathway have been commercialized in the industry. They include Shell's Middle Distillates Synthesis (SMDS) process, Mobil's Methanol-to-Ethanol (MTG) process and the Sasol Slurry Phase Distillate (SSPD) process (Quinlan, 1997).

Shell's SMDS technology was first used in a plant in Bintulu, Malaysia in 1993 (Khoshnoodi et al., 1997). This is actually an improved Fischer – Tropsch process. It first converts syngas to heavy paraffins via the F-T reactions. These paraffins are then hydrotreated to produce liquid fuels such as gasoil, kerosene and naphtha, etc.

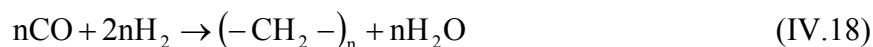
Mobil's MTG technology is not based on Fischer-Tropsch reactions. It first converts methane to syngas through steam reforming as mentioned above, the syngas is then converted to methanol according to the following reaction



finally methanol is converted to gasoline over zeolite catalysts. This technology was first applied in Mobil's plant in New Zealand.

Sasol's SSPD technology was first applied in its Moss gas-to-liquids facility in South Africa in 1992. This process converts methane into synthesis gas through the Fischer – Tropsch reactions and then converts the syngas to liquid fuels such as kerosene, diesel and naphtha, etc.

As seen above, the Fischer – Tropsch process is the essential part of most of the commercial indirect methane conversion technologies. The F-T process was first invented by Franz Fischer and Hans Tropsch in 1923. It was originally invented to produce olefins for the chemical industry. However, great demand for liquid fuels in the Second World War drove the Germans to use it to produce fuel products. Later this process has gone through continuous improvements to make it useful to produce paraffinic liquid fuels over catalysts containing Fe, Co, Ru and similar metals:



Final products rely heavily on the reaction temperature. If the reaction is carried out at relatively high temperature (603 – 623 K), then gasoline and olefins are the main products; however if the reaction is carried out at lower temperatures ( 453 – 523 K), then the main products will be diesel and waxes (Fouda, 1998). A typical flow scheme for natural gas-based low temperature F-T process is shown in Figure IV.3.

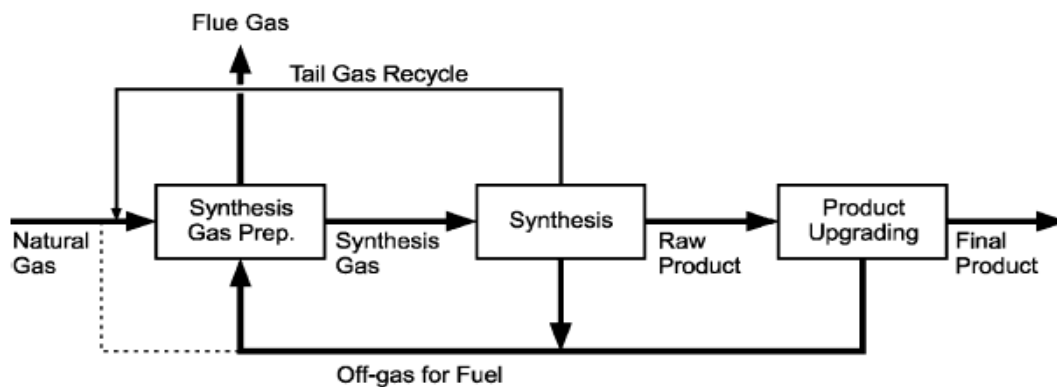
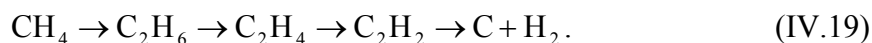


**Figure IV.3. Flow scheme for natural gas-based low temperature Fischer – Tropsch process (Rostrup-Nielsen et al., 2000).**

### High-temperature Pyrolysis

The common disadvantages of the above commercially available methane conversion technologies are that they all require huge natural gas reserves, colossal processing equipment and thus are highly capital intensive. Therefore these technologies are not suitable for smaller scale remote gas reservoirs. Due to this and other technical reasons as mentioned in the above sections, researchers have made continuous effort to search for better technical routes to convert natural gas to the desired products. Of these routes the most sought one is the pyrolysis of natural gas at elevated temperatures to directly produce higher hydrocarbons such as ethylene, acetylene, etc. Below is a brief review of the research work.

Kozlov and Knorre (1962) investigated the thermal decomposition. They studied the stepwise decomposition from methane to ethane to ethylene to acetylene and carbon as shown below



They conducted experiments in a single-pulse shock tube at a pressure of 4 atm and over a wide range of temperature (approximately 1100~2300 K). Their results showed that the overall reactions kinetic rate should be first order, and they determined the kinetic rate constants for each of the above decomposition reactions.

Gulyaev and Polak (1965) also found that the reaction rates to be first order, and they also observed “autoquenching” phenomenon of the decomposition of methane.

Palmer et al. (1968) studied the kinetics of methane’s thermal decomposition. They confirmed that the reaction rate to be first order in a flowing system, while in a static system it seemed to be in the second order. They also found that the main products were  $C_2H_4$  and  $C_2H_2$ , with less quantities of  $C_2H_6$ .  $H_2$  inhibits the decomposition, but ethane enhances it.

Holmen et al. (1976) also confirmed the kinetic rate to be first order.

Huff et al. (1998) found that methane pyrolysis is thermodynamically limited and requires high temperature ( $> 1100$  °C) for reasonable conversion. Addition of hydrogen significantly reduces coke formation. On the contrary,  $H_2$  also decreases methane pyrolysis rates as mentioned by Palmer et al. (1968).

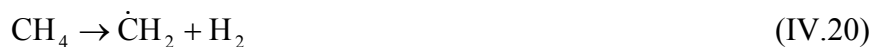
Aulia’s experiments (2000) and Mossaad’s kinetic simulation work (2002) confirmed the above results. Their work provided useful information for further exploration of the non-oxidative pyrolysis of methane toward achieving higher methane conversion and  $C_2$  selectivity.



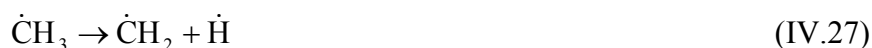
### Methodology for Kinetic Simulation

As mentioned previously, the major component of natural gas is methane, together with small amounts of higher hydrocarbons and other impurities. Therefore, our simulation will start with the case of pure methane pyrolysis. Later we will consider the effects caused by the existence of some other components, such as ethane, hydrogen, water (steam), etc.

Numerous researchers (Billaud, et al, 1992; Holmen, et al, 1994; Hidaka, et al, 1990 & 1999) have shown that the pyrolysis of methane is an extremely complicated process, which may include over one hundred elementary reactions. There are two major mechanisms (Gulyaev, et al, 1965) for these reactions raised by previous researchers. One was raised by Kassel, which presumes that molecular decomposition dominates the whole process as shown below:



Another mechanism of Wiener and Burton presumes that radical reactions dominate the whole process:





Each of the above steps contains many elementary steps making them very complicated to analyze. A simplified reaction model was raised by other researchers (Kozlov, et al, 1962; Holmen, et al, 1976). They assumed that methane was decomposed into higher hydrocarbons along a chain process as follows:

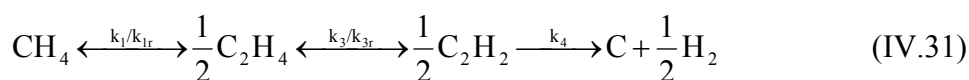


At a reaction temperature of 2000 °C, the heats of reaction are respectively 72 kJ/mol, 309 kJ/mol, -83 kJ/mol, -119 kJ/mol per 2 mol CH<sub>4</sub> for the above four stepwise reactions. The overall reaction heat is 89.3 kJ/mol per mol CH<sub>4</sub>. Thus the whole reaction of methane decomposition is quite endothermic and requires high temperature to move forward.

All of the above components are found in the product gas streams in the experiments by previous researchers. Stepwise, reactions IV.30a & IV.30c are reversible and relatively slow. However, the decomposition of ethane to ethylene in reaction IV.30b is very fast compared with reaction IV.30a, there is little ethane present in the product stream, thus we assume that methane is immediately converted to ethylene, and reaction IV.30b can be neglected in the following simulation work. Acetylene can be decomposed into carbon soot at relatively long residence times. Reaction IV.30d is irreversible but

much slower than reaction IV.30a, making it possible to obtain high yields of acetylene at proper reaction conditions (temperature and residence times, etc.).

Based upon the above analysis we can further simplify the reaction model as follows to fit our simulation purpose:



of which the subscript “r” indicates the rate constant is for the corresponding reverse reaction. Assuming all the above four stepwise reactions to be first order (Kozlov, et al, 1962), the rate constants can be expressed as below:

$$k_1 = 4.5 \times 10^{10} \exp(-45798/T), \text{ ms}^{-1}$$

$$k_3 = 2.57 \times 10^5 \exp(-20131/T), \text{ ms}^{-1}$$

Using the relation between thermodynamic equilibrium rate constant and the kinetic rate constant  $K_{\text{eq}} = k/k_r$ , and  $K_{\text{eq}} = \exp\left(-\frac{\Delta G_R^\circ}{RT}\right)_r$ , using the following Figure

IV.4 or the TRC tables, it is easy to find the rate constants for the reverse reactions to be

$$k_{1r} = 7.4956 \times 10^{11} \exp(-3.0161-41274/T), \text{ ms}^{-1}$$

$$k_{3r} = 7.3513 \times 10^4 \exp(2369/T-15), \text{ ms}^{-1}$$

After numerous studies we found that the above value of  $k_{1r}$  is too large to fit the experimental data from various sources. Thermodynamic and kinetic analysis of the relevant reactions showed that a factor of 1/10 should be applied to correct the above expression of  $k_{1r}$ . Thus in our simulation work below we will multiply the  $k_{1r}$  above by a correction factor of 1/10.

The last stepwise reaction from  $C_2H_2$  to carbon is extremely important for methane decomposition. In order to minimize the formation of carbon soot it is necessary to have an accurate value of its rate constant  $k_4$ . Kozlov and Knorre's result for  $k_4$  is

$$k_4 = 1.7 \times 10^3 \exp(-15098/T), \text{ ms}^{-1}$$

But Kunugi et al.'s (1961) experiments revealed that this kinetic rate constant should be

$$k_4 = 25 \exp(-15098/T), \text{ ms}^{-1}$$

Kozlov's results is 67 times greater than that of Kunugi's. This will result in great change in the formation of coke depending on which rate constant is used. Aulia (2000) carried out plasma experiments to measure this rate constant and found a value between Kozlov's and Kunugi's as below:

$$k_4 = 400 \exp(-15098/T), \text{ ms}^{-1}$$

In the simulation work that follows we will use this expression of  $k_4$ .

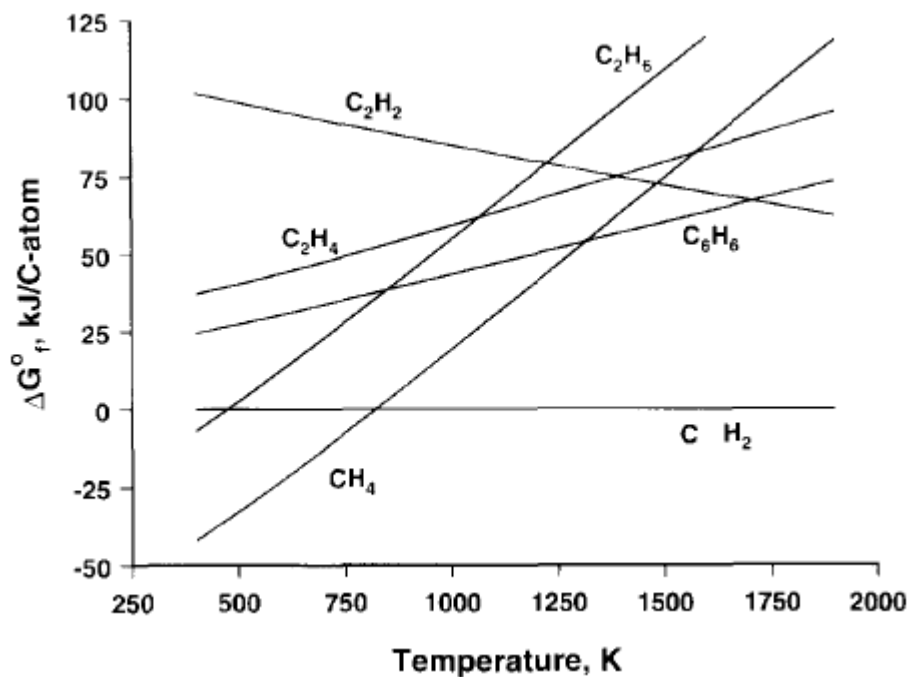


Figure IV.4. Standard free energy of formation ( $\Delta G_f^\circ$ ) of some hydrocarbons as function of temperature (K) (Holmen et al., 1995).

The kinetic rate equations for the above chain reactions of methane decomposition can thus be expressed as follows:

$$\frac{dn_{\text{CH}_4}}{dt} = -k_1 \frac{n_{\text{CH}_4}}{n_T} + k_{1r} \frac{n_{\text{H}_2}}{n_T} \left( \frac{n_{\text{C}_2\text{H}_4}}{n_T} \right)^{1/2} \quad (\text{IV.32a})$$

$$\frac{dn_{\text{C}_2\text{H}_4}}{dt} = \frac{1}{2n_T} \left[ k_1 n_{\text{CH}_4} - k_{1r} n_{\text{H}_2} \left( \frac{n_{\text{C}_2\text{H}_4}}{n_T} \right)^{1/2} \right] - \frac{1}{n_T} \left( k_3 n_{\text{C}_2\text{H}_4} - k_{3r} \frac{n_{\text{C}_2\text{H}_2} n_{\text{H}_2}}{n_T} \right) \quad (\text{IV.32b})$$

$$\frac{dn_{\text{C}_2\text{H}_2}}{dt} = \frac{1}{n_T} \left[ k_3 n_{\text{C}_2\text{H}_4} - k_{3r} \frac{n_{\text{C}_2\text{H}_2} n_{\text{H}_2}}{n_T} \right] - k_4 \frac{n_{\text{C}_2\text{H}_2}}{n_T} \quad (\text{IV.32c})$$

$$\frac{dn_{\text{C}}}{dt} = 2k_4 \frac{n_{\text{C}_2\text{H}_2}}{n_T} \quad (\text{IV.32d})$$

$$\frac{dn_{H_2}}{dt} = \frac{1}{n_T} \left[ k_1 n_{CH_4} - k_{1r} n_{H_2} \left( \frac{n_{C_2H_4}}{n_T} \right)^{1/2} \right] + \frac{1}{n_T} \left( k_3 n_{C_2H_4} - k_{3r} \frac{n_{C_2H_2} n_{H_2}}{n_T} \right) + k_4 \frac{n_{C_2H_2}}{n_T}$$

(IV.32e)

where  $n_i$  is the number of moles of component  $i$  in the product gas stream.  $n_T$  is the total moles of products. Residence time is indicated by the letter  $t$ .

In all the calculations that follow we will assume both the total pressure and the operating pressure will be 1 atm, so that the pressure terms will be cancelled out and will not appear in the differential equations IV.32 as shown above.

As mentioned previously, the overall reaction of the thermal decomposition of methane is quite endothermic. Temperature of the gas stream will continue to drop as the reactions advance along the reactor tube. To track the temperature change of the gas stream, we need to apply the energy balance equations. Based on identical reference states the overall balance equation is expressed as  $H_{in} = H_{out}$ , in which both the left-hand-side and right-hand-side terms can be broken into the enthalpy terms of each component present at the inlet or the outlet gas streams of the reactor. The molar enthalpy of the relevant components are given (based on identical reference state) as below:

$$H_{CH_4} = 14.15T + 0.03775T^2 - 6 \times 10^{-6}T^3 - 7481 \text{ kJ/mol} \quad (IV.33a)$$

$$H_{C_2H_6} = 9.40T + 0.07992T^2 - 15.4 \times 10^{-6}T^3 - 9597 \text{ kJ/mol} \quad (IV.33b)$$

$$H_{C_3H_8} = 10.085T + 0.11966T^2 - 24.46 \times 10^{-6}T^3 - 13135 \text{ kJ/mol} \quad (IV.33c)$$

$$H_{C_4H_{10+}} = 16.088T + 0.15346T^2 - 31.6 \times 10^{-6}T^3 - 17785 \text{ kJ/mol} \quad (IV.33d)$$

$$H_{H_2} = 27.01T + 0.001754T^2 - 69009/T - 8031 \text{ kJ/mol} \quad (IV.33e)$$

$$H_{H_2O} = 28.85T + 0.006028T^2 - 10^5/T - 8862 \text{ kJ/mol} \quad (IV.33f)$$

$$H_{\text{CO}_2} = 45.37T + 0.004344T^2 + 9.62 \times 10^5 / T - 17209 \text{ kJ/mol} \quad (\text{IV.33g})$$

$$H_{\text{CO}} = 28.07T + 0.002316T^2 + 2.577 \times 10^4 / T - 8715 \text{ kJ/mol} \quad (\text{IV.33h})$$

$$H_{\text{N}_2} = 27.27T + 0.002465T^2 - 33257 / T - 8292 \text{ kJ/mol} \quad (\text{IV.33i})$$

For the case of lean natural gas simulation, we will choose  $\text{CH}_4$  as our reference substance to calculate the heats of reactions when other components like  $\text{C}_2\text{H}_4$ ,  $\text{C}_2\text{H}_2$  and carbon appear in the product gas streams. At this time the following term needs to be added to calculate the term  $H_{\text{out}}$  :

$$217,000n_{\text{C}_2\text{H}_4} + 404,000n_{\text{C}_2\text{H}_2} + 90,200n_{\text{C}} \quad (\text{IV.33j})$$

The three numbers in the above expression are the molar heats of reactions from  $\text{CH}_4$  to the corresponding products ( $\text{C}_2\text{H}_4$ ,  $\text{C}_2\text{H}_2$  and  $\text{C}$ ).

As rich gas contains ethane, propane, butane and small amount of higher hydrocarbons, it is very complicated to accurately calculate the separate enthalpies of each minor component. Therefore for these hydrocarbons we will adopt a simplified method by converting them into equivalent amount of ethylene according to the elemental mass balance of carbon and hydrogen:

$$\Delta n_{\text{C}_2\text{H}_4}^0 = n_{\text{C}_2\text{H}_6}^0 + \frac{3}{2}n_{\text{C}_3\text{H}_8}^0 + 2n_{\text{C}_4\text{H}_{10}}^0 \quad (\text{IV.34})$$

$$\Delta n_{\text{H}_2}^0 = n_{\text{C}_2\text{H}_6}^0 + n_{\text{C}_3\text{H}_8}^0 + n_{\text{C}_4\text{H}_{10}}^0 \quad (\text{IV.35})$$

That means that in the simulation of rich gas we just add the above two terms to the original amount of ethylene and hydrogen to calculate the energy (but NOT material) balance.

In addition, we have to choose the same reference substance to calculate the heats of reactions for all the chain reactions from  $\text{CH}_4$  to  $\text{C}_2\text{H}_4$  to  $\text{C}_2\text{H}_2$  to carbon soot. Here we

choose ethylene as the reference substance as shown in Figure IV.5. Then following terms have to be added to the total enthalpy calculation on both sides of the equation

$$H_{in} = H_{out} :$$

$$108,820(n_{CH_4}^0 - n_{CH_4}) + 142,410n_{C_2H_6}^0 + 184,340n_{C_3H_8}^0 + 228960n_{C_4H_{10}}^0 + 187,070n_{C_2H_2} - 17,740n_C \quad (IV.36)$$

of which the first term is the energy to go from methane to ethylene, the second term is from ethane to ethylene which is assumed to be instantaneous conversion, and the same for the third and fourth terms above. The last two terms indicate the energy change from ethylene to acetylene and then to carbon soot. These changes can be better seen from Figure IV.5.

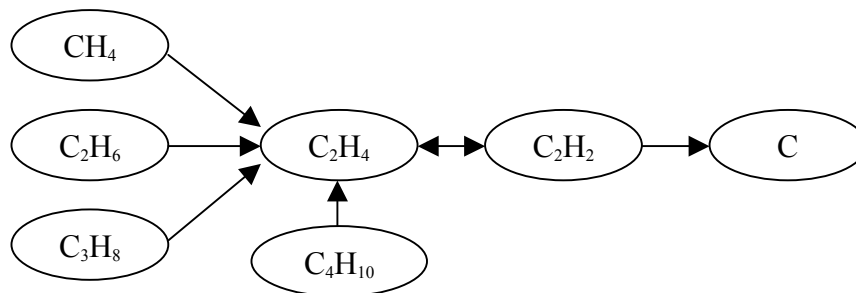


**Figure IV.5. Schematic diagram to show the reference substance and energy changes for energy balance calculation.**

By solving the above differential equations (for mass balance) and the energy balance equations we will then be able to find the amount of each component in the gas stream and the temperature at each point along the reactor tube. In the following sections we will follow this methodology to simulate the pyrolysis of methane under different process conditions.



To interpret the results the following definitions (Holmen et al., 1976) are used for methane conversion and the yields of the products of interest to our analysis:

$$\text{Conversion of methane} = \frac{n_{\text{CH}_4}^0 - n_{\text{CH}_4}}{n_{\text{CH}_4}^0} \times 100\% \quad (\text{IV.37})$$

$$\text{Yield of species } i = \frac{n_i - n_i^0}{\nu_i n_{\text{CH}_4}^0} \times 100\% , \quad (\text{IV.38})$$

of which  $\nu_i$  is the stoichiometric coefficient from  $\text{CH}_4$  to species  $i$ ,  $\nu_i = 1/2, 1/2$  & 1 for  $\text{C}_2\text{H}_4, \text{C}_2\text{H}_2$  & carbon, respectively.

In the literature numerous researchers did their simulation work based on an isothermal assumption (Kozlov et al., 1962; Palmer et al., 1968). This leads to very high carbon formation which is not in agreement with experimental results. Recent examination of the heat effect of the chain reactions revealed that there is an “autoquenching” effect along the reactor tube. It is thus more reasonable to assume the reactions to be adiabatic in terms of heat effect since the reaction time is normally very short. Our subsequent simulation will be carried out based on this assumption.

Figure IV.6 is a schematic diagram to show the reactor system for our simulation for potential industrial application. We divide the system into a preheating section and a reaction section. In the preheating section, fuel (stream B) of either natural gas or hydrogen recovered from the pyrolysis product gas stream is burned with air or pure oxygen (stream A), which releases large amounts of heat. The high-temperature flame (stream F) is mixed with the fresh natural gas feed (stream N) to heat it to a proper high temperature before the mixture stream enters the cracker. Then the feed goes through the

cracker within short residence time and is decomposed into final products (stream G) such as ethylene, acetylene and carbon (coke), etc.

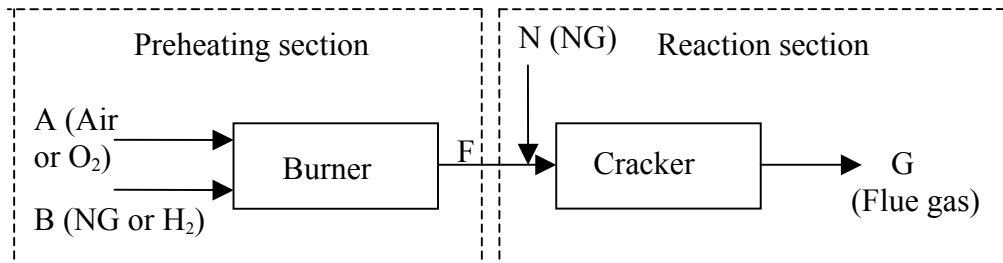


**Figure IV.6. Block diagram of the reaction system used in the current simulation work.**

In the following chapter we will consider first the cases only with the reaction section. Later we will take the preheating section into consideration for a more practical case.

**CHAPTER V**

**KINETIC SIMULATION OF NATURAL GAS PYROLYSIS**

**UNDER ADIABATIC CONDITIONS**

**Pure Methane Feed**

In this case we do not use the preheating section (combustion zone) to provide extra energy to the reaction zone. Thus the system considered here starts from methane entering the cracker and ends with the product gas leaving the cracker.

Here the total enthalpy balance is calculated as follows:

$$H_{in} = H_{CH_4}(T_{in})n_{CH_4}^0 \quad (V.1a)$$

$$H_{out} = H_{CH_4}(T_{out})n_{CH_4}^0 + 217,000n_{C_2H_4} + 404,000n_{C_2H_2} + 90,200n_C + H_{H_2}(T_{out})n_{H_2}^0 \quad (V.1b)$$

There is only one component ( $CH_4$ ) in the feed gas yet there are  $CH_4$ ,  $C_2H_4$ ,  $C_2H_2$ ,  $C$  and  $H_2$  in the product gas stream. Substituting the above expressions into  $H_{in} = H_{out}$  we get the energy balance equation. Combining this equation with the mass balance equations IV.32 we can solve for the amount of each component in moles and the temperature at the outlet of the cracker.

The following Figures V.1~5 are the results for the thermal decomposition of pure methane feed based on 1 mol  $CH_4$ . As explained in the previous chapter, the overall reaction is very endothermic and requires a large amount of energy to move forward. Thus it can be estimated that high temperatures will promote the decomposition of methane. This is indeed the case as seen from Figure V.1. At lower inlet temperature

(1600 K), methane conversion is very small (1.4% @ 1 ms and 4.8% @ 8 ms) and is almost negligible as also seen by other researchers (Yao et al., 2001); when the temperature increases to 2000 K, these two numbers rise to 19.2% and 23.4% respectively. This trend is better seen in Figure V.2a. Here it is very obvious that conversion of methane increases with the rise of the cracker's inlet temperature at identical residence times.

The increase of methane conversion with longer residence times at the same inlet temperature is self-evident. However, from Figure V.2b we can see that the conversion curves are basically leveled off when residence time is more than 4 ms for most inlet temperatures, indicating that most of the methane may have been decomposed within 4 ms. This was also confirmed by Mossaad (PhD dissertation, 2002) in his research work.

Figure V.3 shows the amount of the three main components –  $C_2H_4$ ,  $C_2H_2$  & carbon – in the product gas streams versus inlet temperature at selected residence times. From these figures it is seen that acetylene and ethylene are the major products of methane pyrolysis. It can also be found that the formation of acetylene increases sharply with higher inlet temperature of the thermal cracker at fixed residence times, while that of ethylene and carbon increases much slower under the same conditions. Figure V.3b~e shows that the formation of carbon may surpass that of ethylene at higher inlet temperatures and longer residence times.

Figure V.4 shows the yield of the above three main products versus residence times at selected temperatures. We can see that longer residence times lead to more acetylene and carbon formation but cause the ethylene formation to drop at fixed inlet

temperatures of 2000 K and below. This was also confirmed by other researchers (Anderson et al., 2002).

Figure V.5 shows the outlet temperatures of the thermal cracker versus residence times at selected inlet temperatures of the cracker. It is interesting to note from Figure V.5a that different  $T_{in}$  lead to almost the same  $T_{out}$  when the residence time is less than 1 ms, a fact which was confirmed by the experiments of a pilot plant. This phenomenon may be explained that different inlet temperatures to the thermal cracker cause different levels of methane conversion, with lower inlet temperatures corresponding to lower methane conversion and higher inlet temperatures corresponding to higher methane conversion; since the reaction of methane conversion is very endothermic, higher methane conversion leads to more consumption of the reaction system's energy, which then leads to sharper drop of the corresponding outlet temperature at the exit of the thermal cracker. The overall result is almost identical outlet temperatures for different inlet temperatures.

From the above analysis, it is concluded that higher inlet temperatures and shorter residence times are beneficial to attaining higher methane conversion and higher yields of desired products such as ethylene and acetylene.

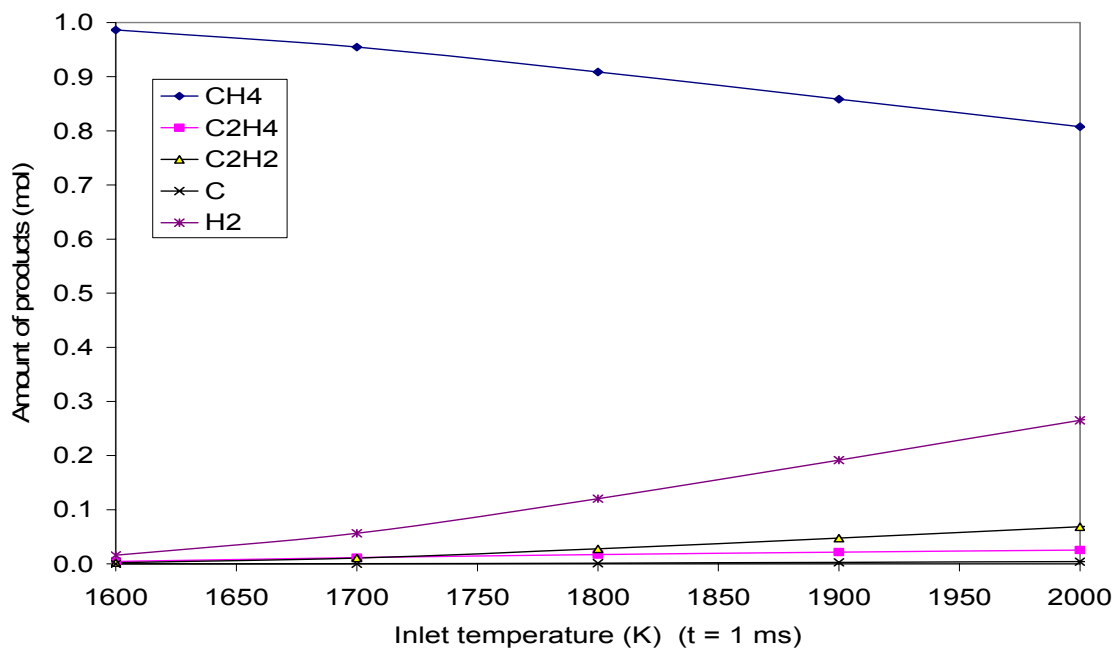


Figure V.1a. Amount of components in the product gas stream at various inlet temperatures. Resident time = 1 ms.  $n_{\text{CH}_4}^0 = 1 \text{ mol}$ ,  $P = 1 \text{ atm}$ .

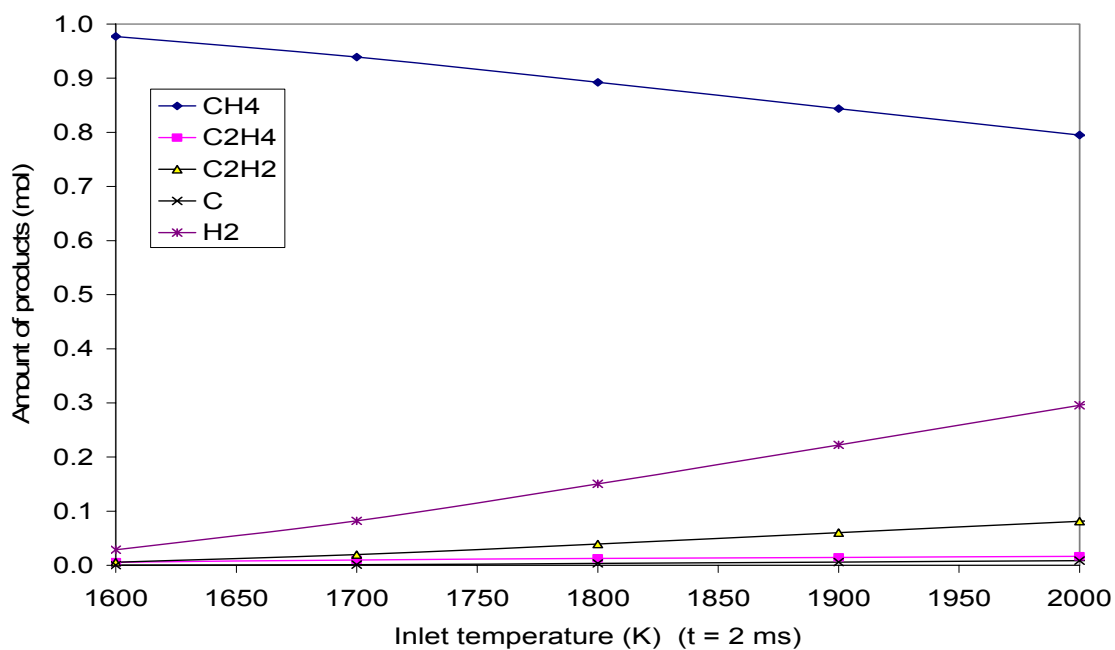


Figure V.1b. Amount of components in the product gas stream at various inlet temperatures. Resident time = 2 ms.  $n_{\text{CH}_4}^0 = 1 \text{ mol}$ ,  $P = 1 \text{ atm}$ .

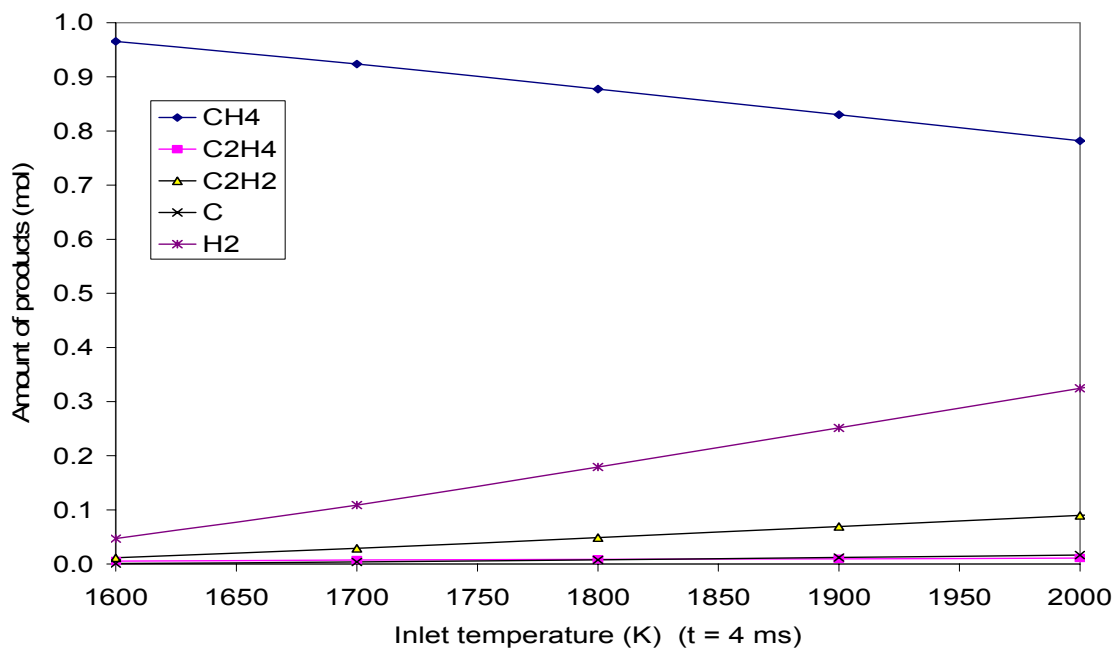


Figure V.1c. Amount of components in the product gas stream at various inlet temperatures. Resident time = 4 ms.  $n_{\text{CH}_4}^0 = 1 \text{ mol}$ ,  $P = 1 \text{ atm}$ .

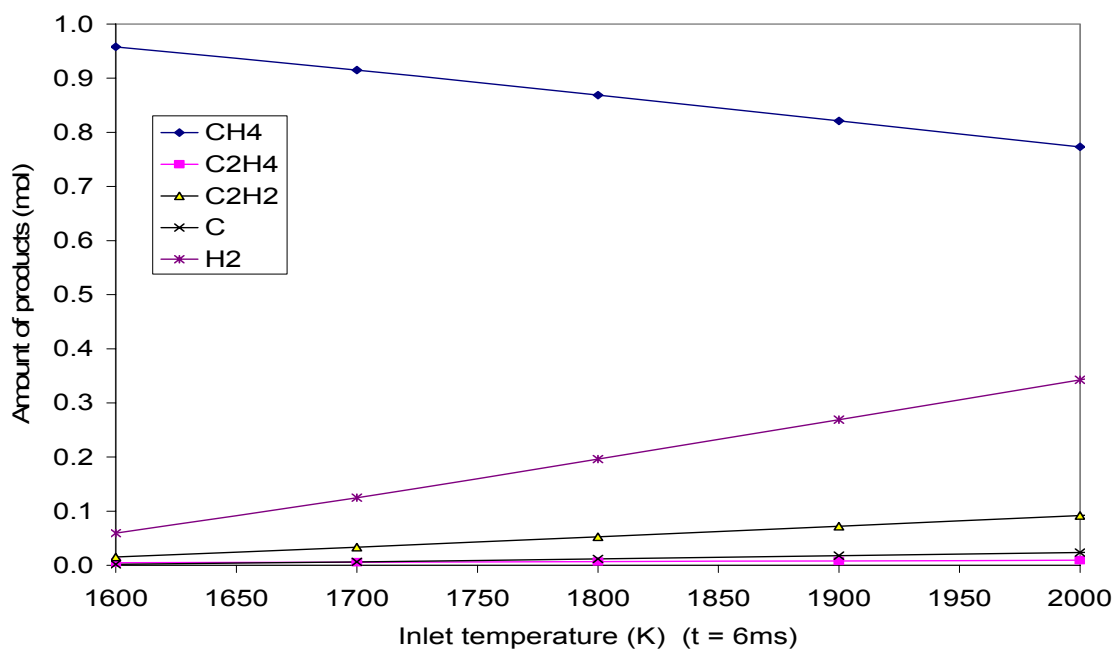


Figure V.1d. Amount of components in the product gas stream at various inlet temperatures. Resident time = 6 ms.  $n_{\text{CH}_4}^0 = 1 \text{ mol}$ ,  $P = 1 \text{ atm}$ .

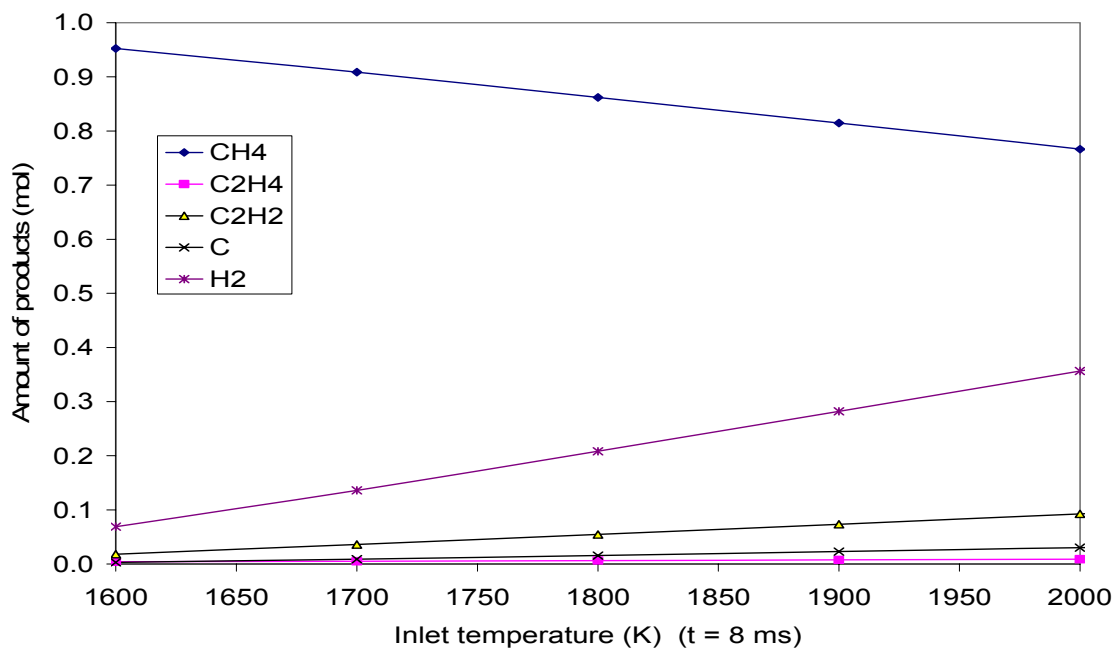


Figure V.1e. Amount of components in the product gas stream at various inlet temperatures. Resident time = 8 ms.  $n_{\text{CH}_4}^0 = 1 \text{ mol}$ ,  $P = 1 \text{ atm}$ .

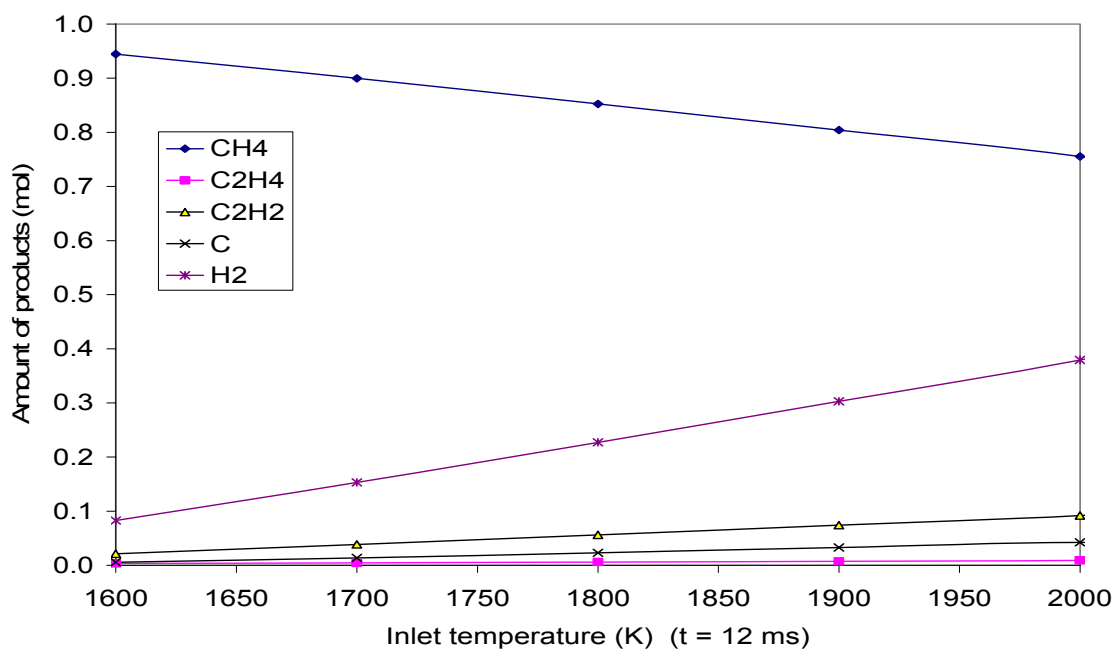


Figure V.1f. Amount of components in the product gas stream at various inlet temperatures. Resident time = 12 ms.  $n_{\text{CH}_4}^0 = 1 \text{ mol}$ ,  $P = 1 \text{ atm}$ .



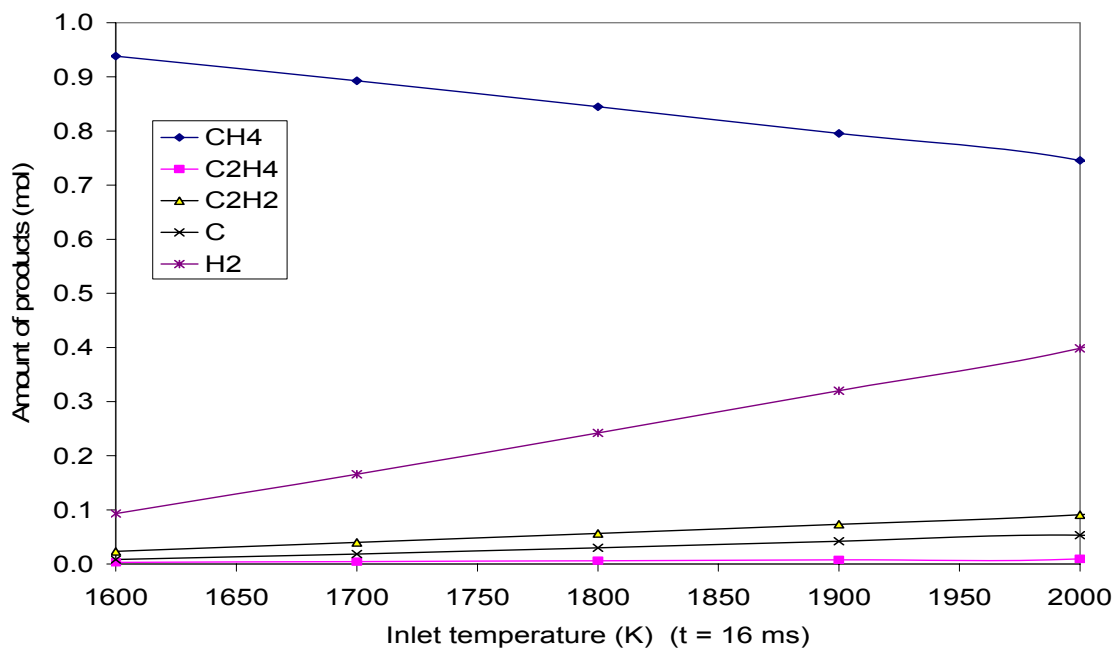


Figure V.1g. Amount of components in the product gas stream at various inlet temperatures. Resident time = 16 ms.  $n_{\text{CH}_4}^0 = 1 \text{ mol}$ ,  $P = 1 \text{ atm}$ .

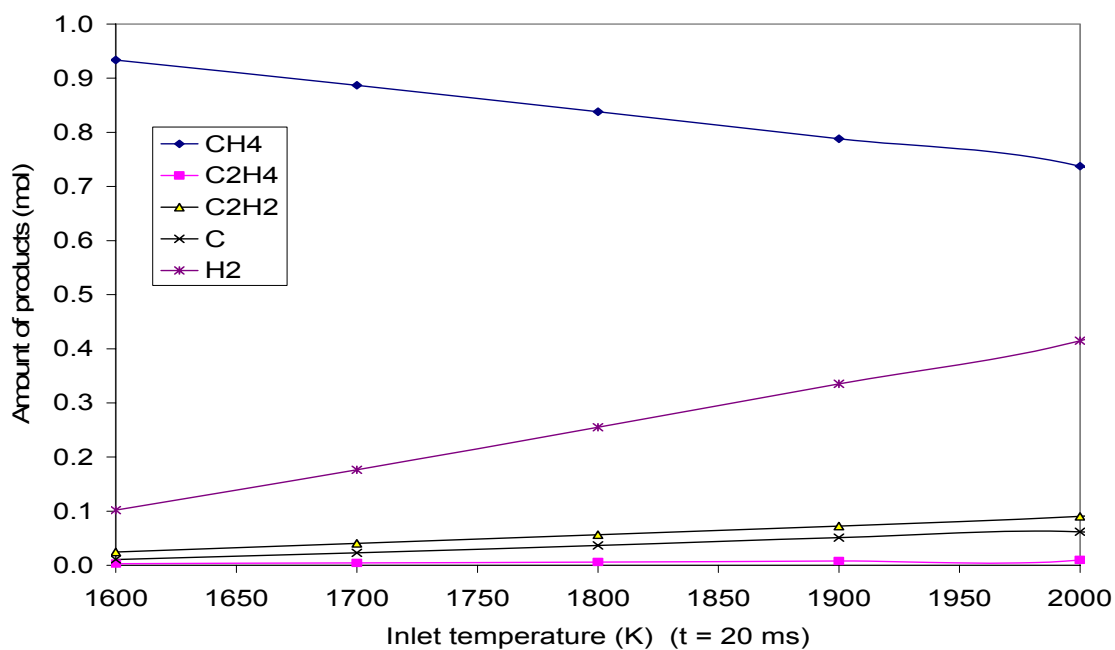


Figure V.1h. Amount of components in the product gas stream at various inlet temperatures. Resident time = 20 ms.  $n_{\text{CH}_4}^0 = 1 \text{ mol}$ ,  $P = 1 \text{ atm}$ .

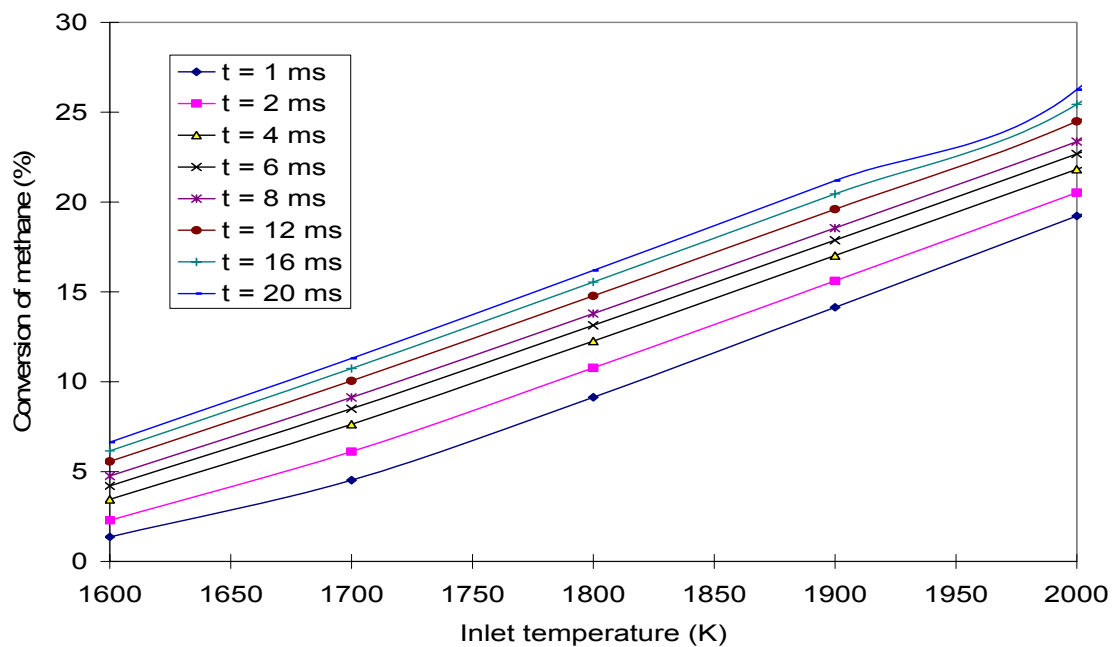


Figure V.2a. Conversion of methane versus temperature at various residence times.  
 $n_{\text{CH}_4}^0 = 1 \text{ mol}$ ,  $P = 1 \text{ atm}$ .

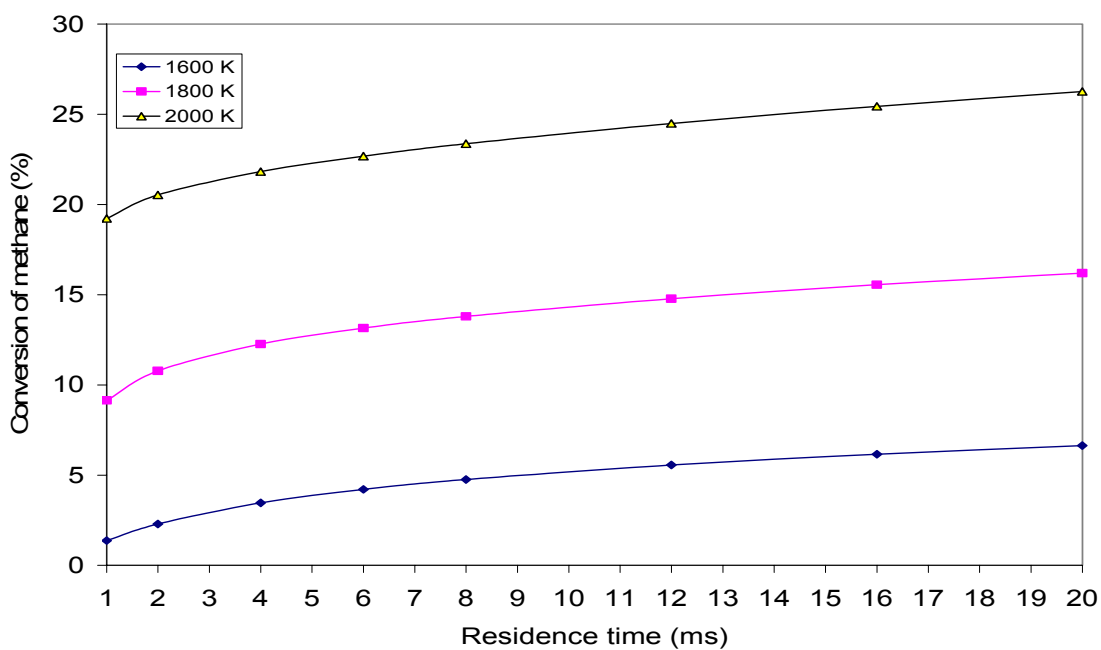
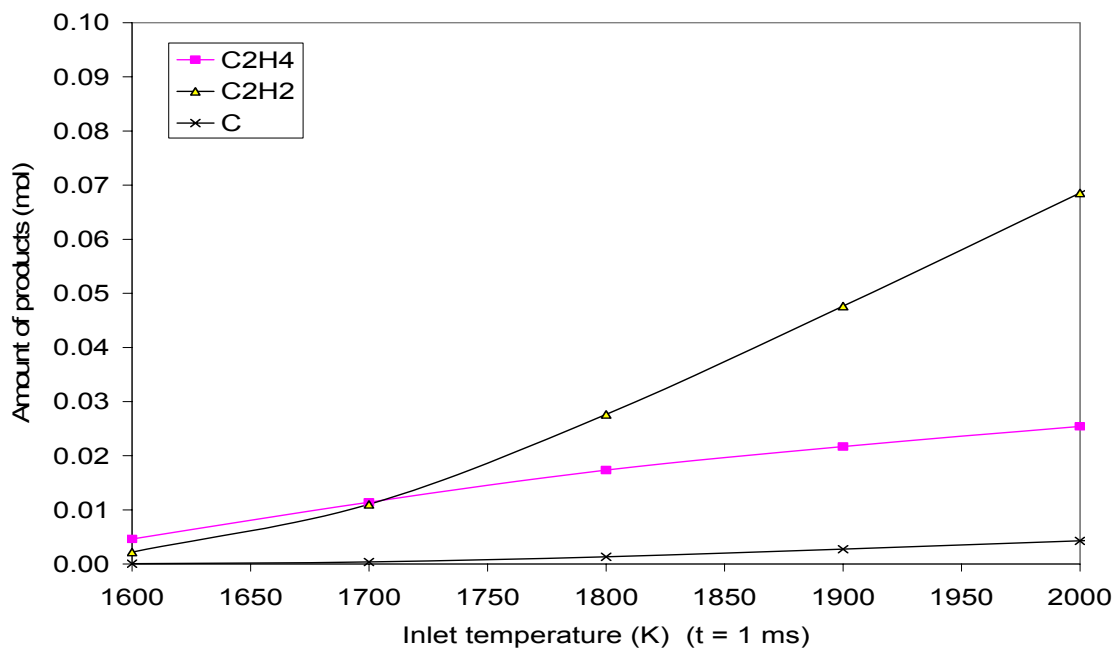
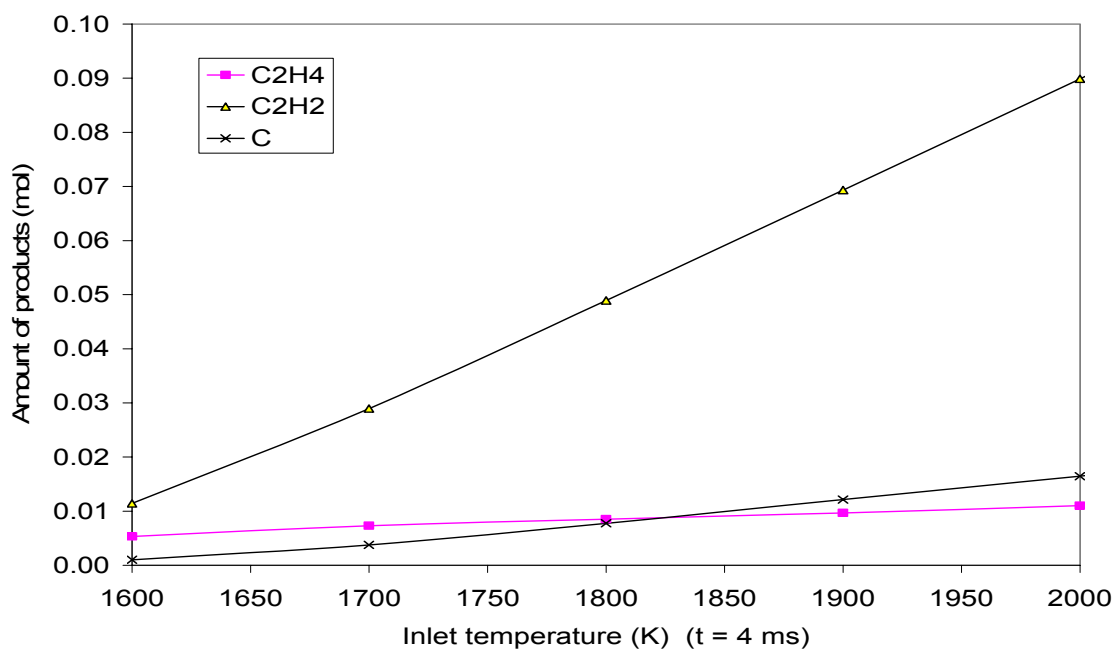


Figure V.2b. Conversion of methane versus residence time at selected inlet temperatures.  
 $n_{\text{CH}_4}^0 = 1 \text{ mol}$ ,  $P = 1 \text{ atm}$ .



**Figure V.3a. Amount of three main products at various inlet temperatures. Resident time = 1 ms.  $n_{\text{CH}_4}^0 = 1 \text{ mol}$ ,  $P = 1 \text{ atm}$ .**



**Figure V.3b. Amount of three main products at various inlet temperatures. Resident time = 4 ms.  $n_{\text{CH}_4}^0 = 1 \text{ mol}$ ,  $P = 1 \text{ atm}$ .**

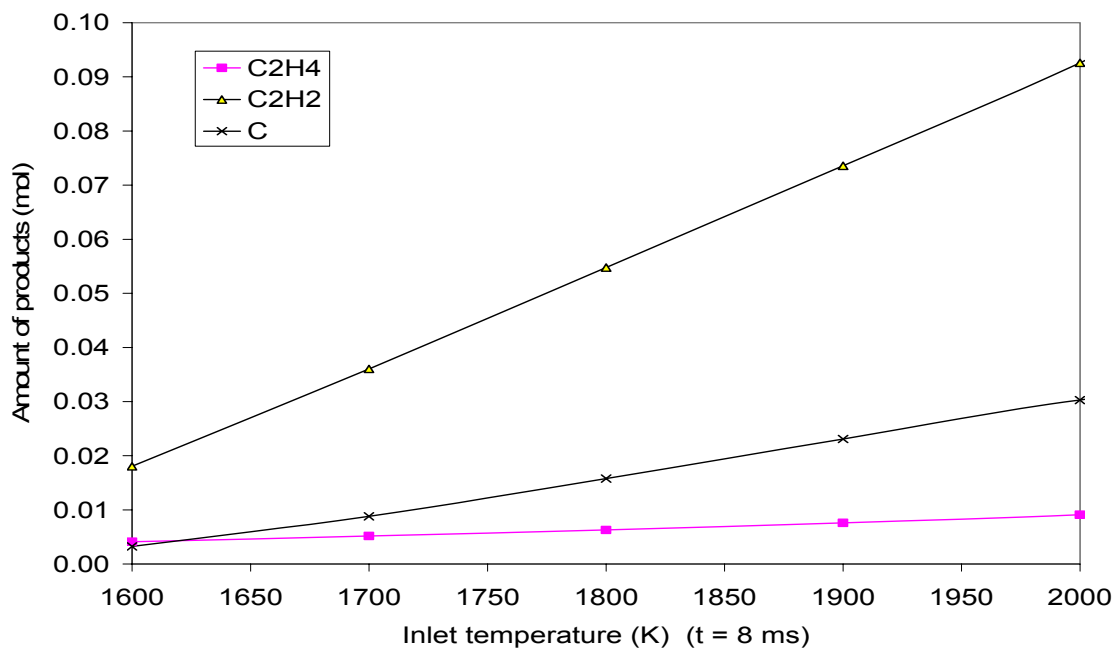


**Figure V.3c. Amount of three main products at various inlet temperatures. Resident time = 8 ms.  $n_{\text{CH}_4}^0 = 1 \text{ mol}$ ,  $P = 1 \text{ atm}$ .**

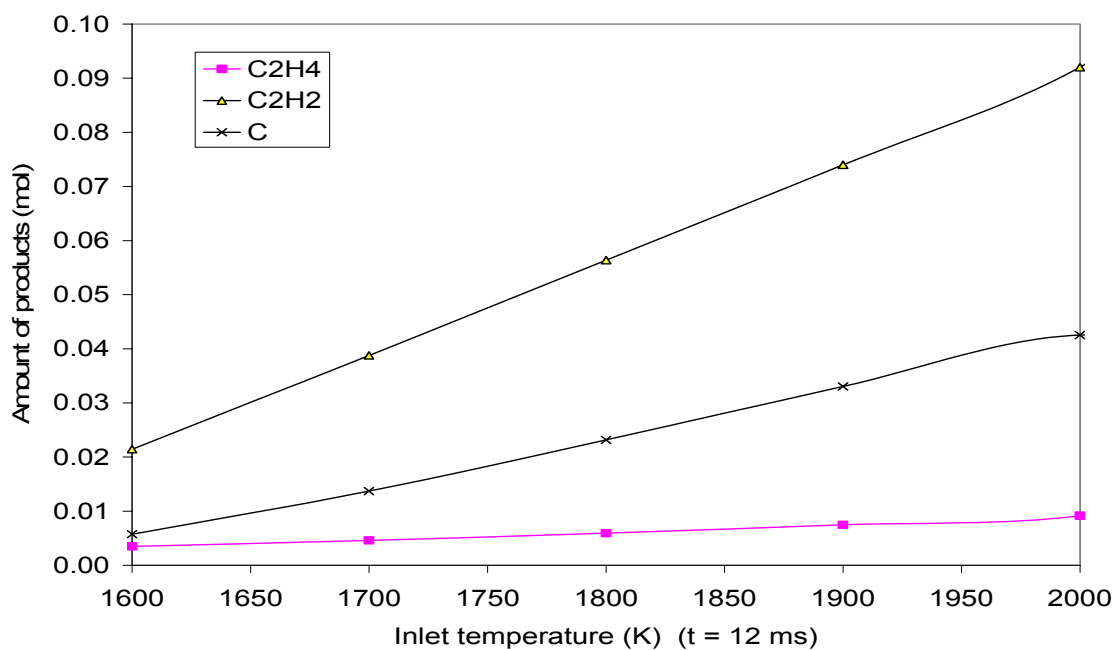


**Figure V.3d. Amount of three main products at various inlet temperatures. Resident time = 12 ms.  $n_{\text{CH}_4}^0 = 1 \text{ mol}$ ,  $P = 1 \text{ atm}$ .**

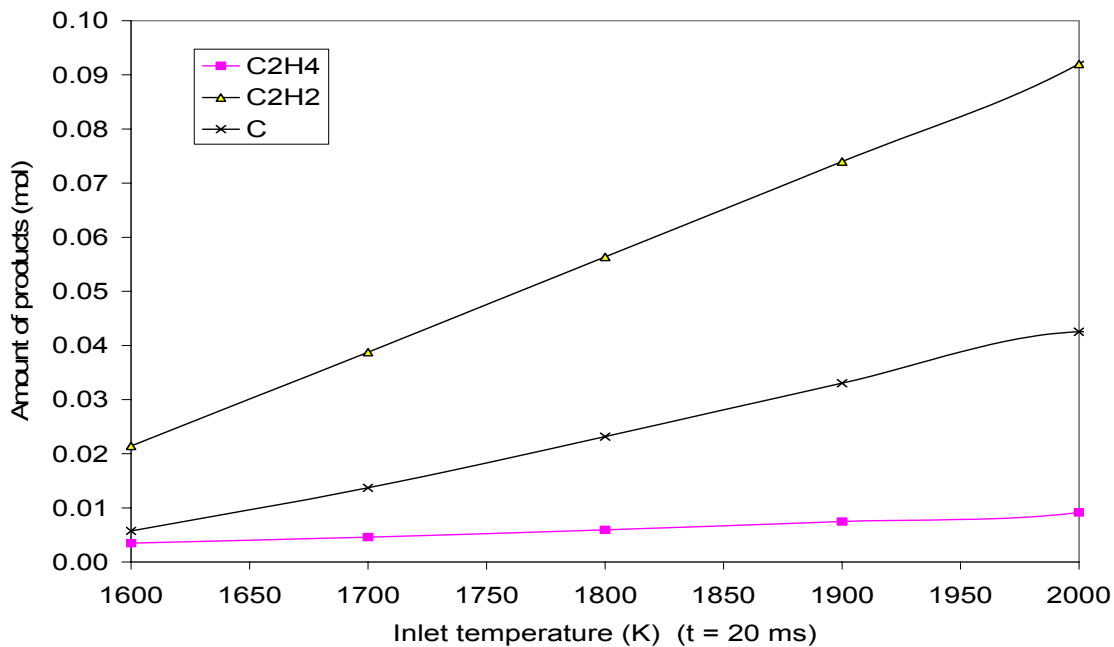


**Figure V.3e. Amount of three main products at various inlet temperatures. Resident time = 20 ms.  $n_{\text{CH}_4}^0 = 1 \text{ mol}$ ,  $P = 1 \text{ atm}$ .**

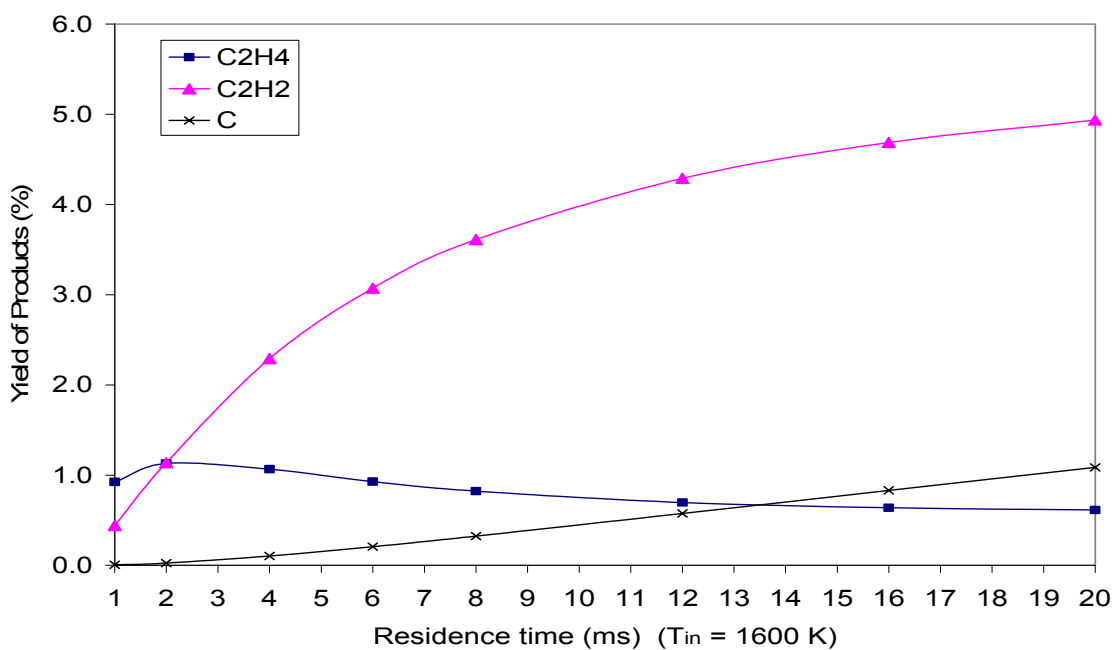


**Figure V.4a. Yield of three main products versus residence times at  $T_{\text{in}} = 1600 \text{ K}$ .  $n_{\text{CH}_4}^0 = 1 \text{ mol}$ ,  $P = 1 \text{ atm}$ .**

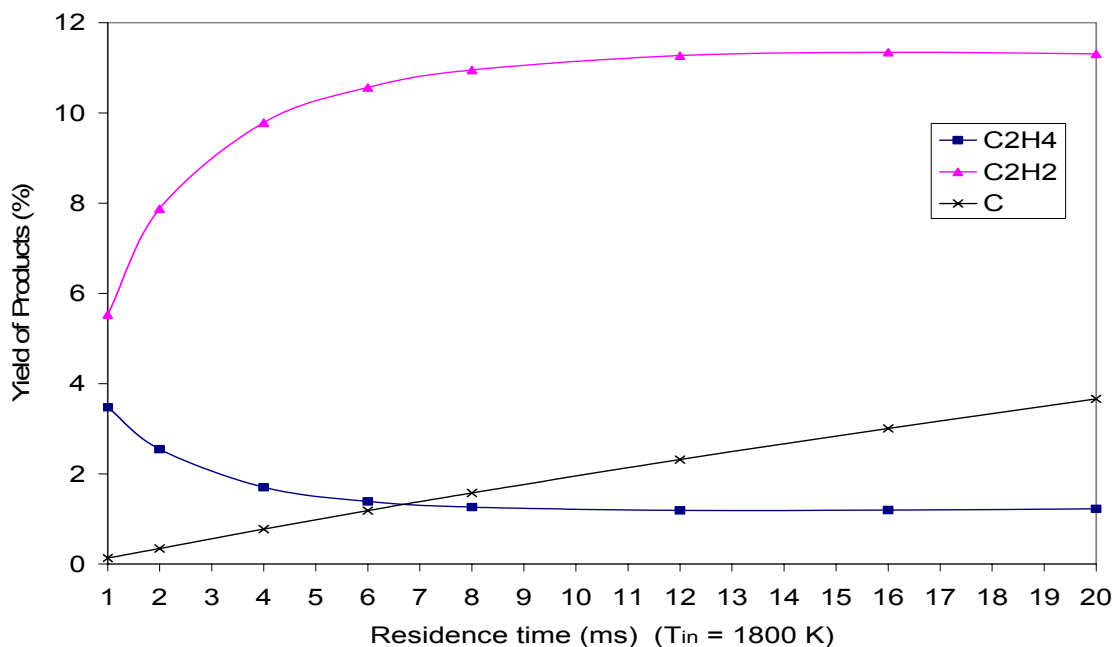


Figure V.4b. Yield of three main products versus residence times at  $T_{in} = 1800\text{ K}$ .  
 $n_{\text{CH}_4}^0 = 1\text{ mol}$ ,  $P = 1\text{ atm}$ .

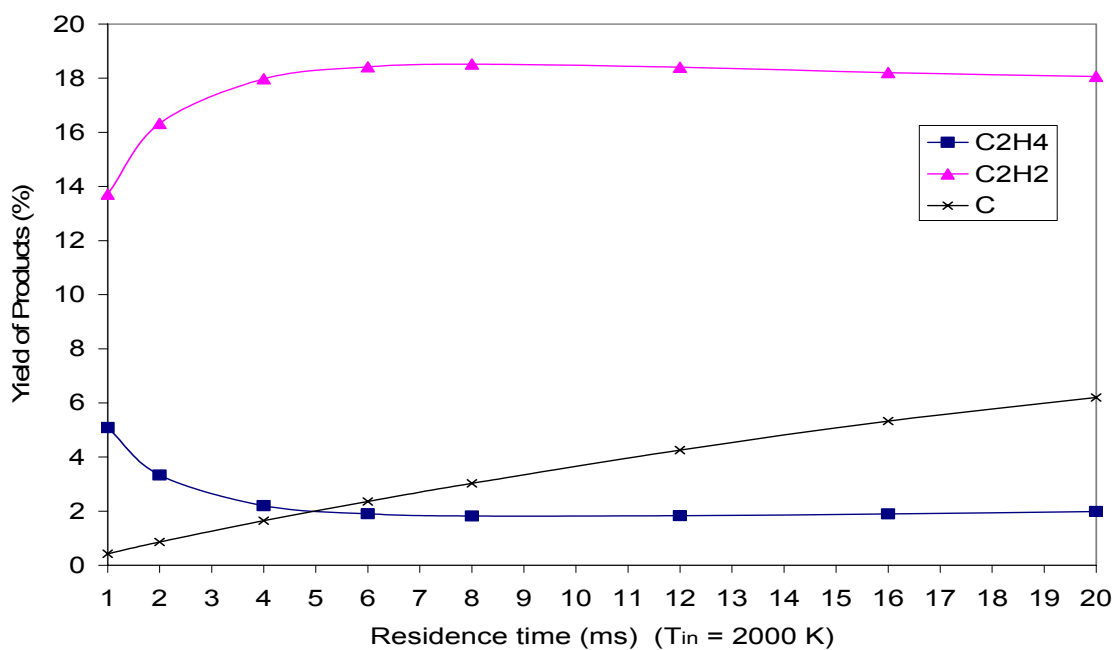
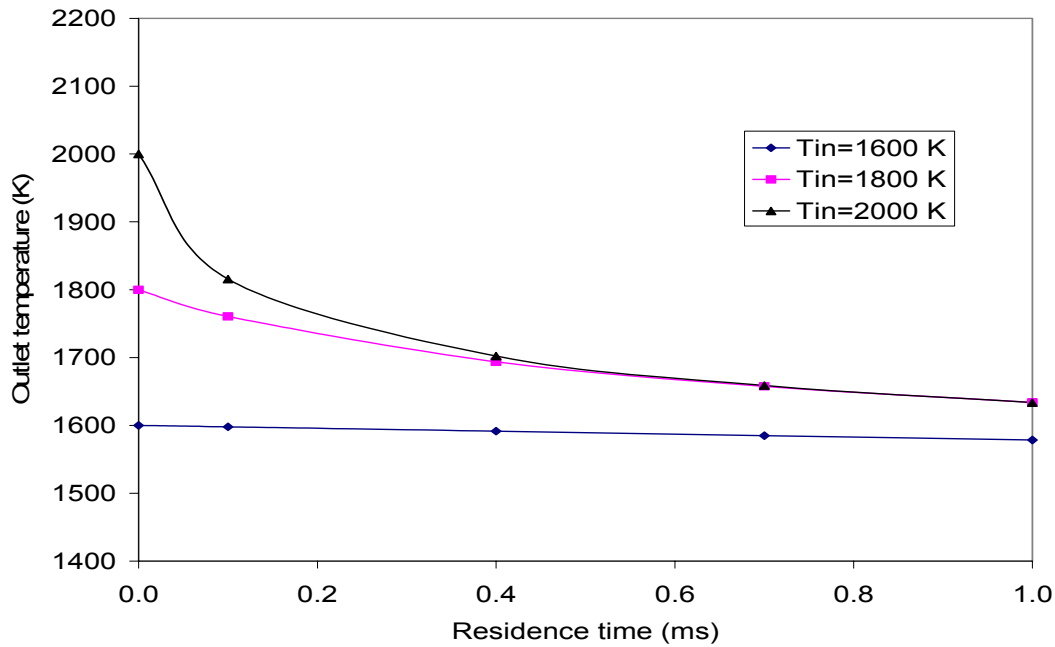
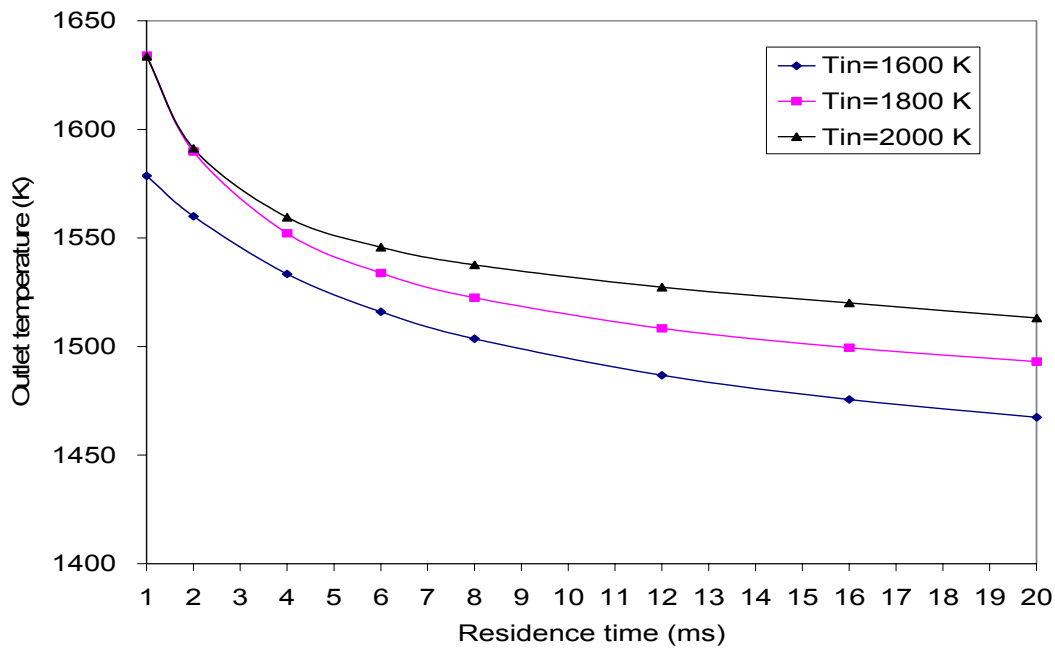


Figure V.4c. Yield of three main products versus residence times at  $T_{in} = 2000\text{ K}$ .  
 $n_{\text{CH}_4}^0 = 1\text{ mol}$ ,  $P = 1\text{ atm}$ .



**Figure V.5a. Outlet temperature profile of the thermal cracker versus residence time at various inlet temperatures.  $t = 0 \sim 1$  ms.**



**Figure V.5b. Outlet temperature profile of the thermal cracker versus residence time at various inlet temperatures.  $t = 1 \sim 20$  ms.**

### Effect of Hydrogen Dilution

A major product of the thermal pyrolysis of methane is hydrogen as seen from the stepwise decomposition reactions shown in Chapter IV. Thus the partial pressure of H<sub>2</sub> in the product gas stream has an important effect on the kinetics of methane pyrolysis. Since each step of methane decomposition produces hydrogen, it is reasonable to assume that addition of hydrogen to the methane feed will lower the conversion of methane from the kinetic point of view. This is really the case as shown by Holmen et al. (1995) and many other researchers (Li et al., 2001). However, it must be kept in mind that this conclusion is drawn under the assumption of *isothermal* reaction. The observation of hydrogen being able to suppress coke formation as shown by many previous researchers is also based on the assumption of isothermal reaction.

In our simulation we assume that hydrogen is mixed with methane at 1:1 ratio at the same temperature before the mixture is fed into the reactor. And as we mentioned previously, we assume that the methane pyrolysis reaction is *adiabatic* rather than *isothermal*. To calculate the energy balance, we need to add the enthalpy term of hydrogen into the H<sub>in</sub> expression as below:

$$H_{in} = H_{CH_4}(T_{in})n_{CH_4}^0 + H_{H_2}(T_{in})n_{H_2}^0 \quad (V.2)$$

H<sub>out</sub> is calculated by the same formula as given in the previous section.

The following figures show the results of our simulation based on the above assumptions and calculation methods.

Figures V.6a – V.6c show the moles of components in the product gas streams at various inlet temperatures and residence times. These results are based on a mixture feed of 1mol CH<sub>4</sub> to 1mol H<sub>2</sub>. The curve of H<sub>2</sub> is removed from the figures to keep the



ordinate scale at 1 mol. The general trend of the amount changes of each component is similar to the case of pure methane feed.

Figures V.7 a & b show the comparison of methane conversion between the case of pure  $\text{CH}_4$  feed and the case of  $\text{CH}_4 + \text{H}_2$  feed at the same residence time. It is seen that at lower inlet temperatures the dilution of hydrogen decreases the methane conversion, while at higher temperatures hydrogen actually increases methane conversion. This result is *different* from that for the isothermal reaction case reported in the literature. As mentioned above, this is due to our assumption that the methane pyrolysis is an adiabatic reaction but not an isothermal reaction. The results shown on these two figures can be explained as follows. On one side, addition of hydrogen can push the chain reactions toward the reverse direction according to the kinetic analysis given above, thus resulting in drop of methane conversion and carbon formation; on the other side, as we assume hydrogen is mixed with methane at the same high temperature before they enter the reactor, the addition of equivalent amount of hydrogen to methane actually brings a lot of energy into the reaction zone, causing the average temperature of the whole reaction zone to drop more slowly than in the pure methane feed case. Higher temperature always increases the values of the kinetic rate constants  $k_i$ , thus pushing the chain reactions to move forward, resulting in higher methane conversion and higher carbon formation. So we can say that in either of the two cases shown in Figure V.7, the first factor shown above dominates the reaction system in the lower temperature zone, causing the addition of hydrogen to lower the conversion of methane. However, in the higher temperature zone the second factor dominates the reaction system thus the addition of hydrogen will actually increase the methane conversion.

Figures V.8 a & b show the yield of carbon, i.e. coke formation at various temperatures and at selected residence times. From these curves we see that dilution of hydrogen can lower the formation of coke as reported in the literature. This can also be explained by the reasons as presented in the previous paragraph.

From the above analysis we see that the results of dilution of hydrogen to pure methane feed are not very comparative to those presented in the literature. The basic reason lies in the two completely different assumptions made about the reaction temperature of the whole pyrolysis. This should be given special attention when we try to interpret data from different sources.

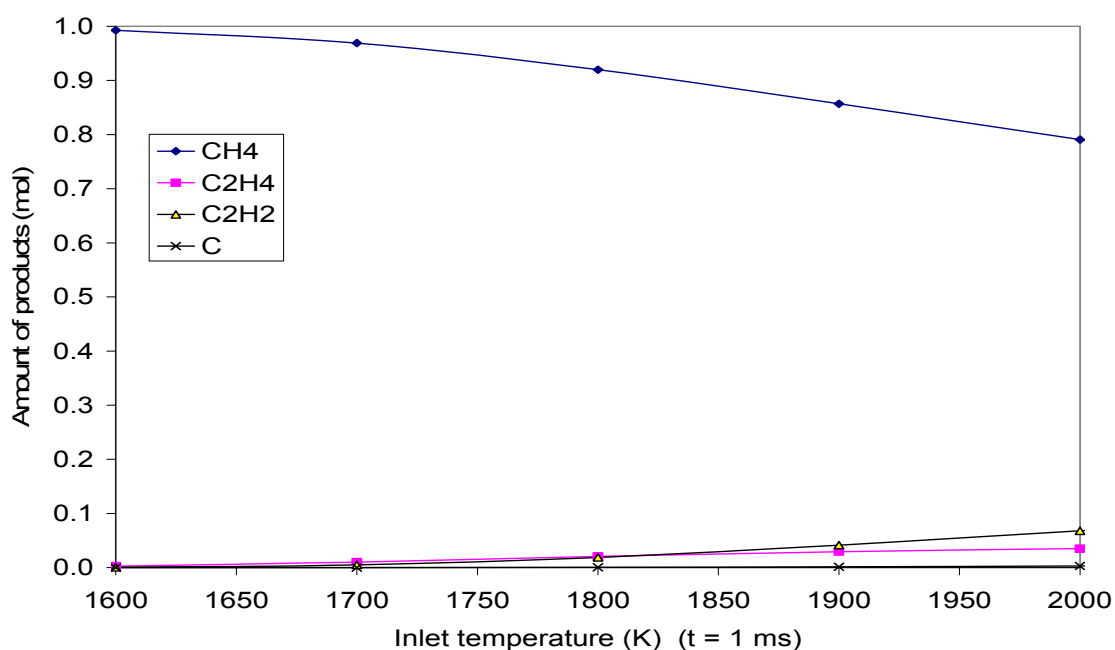


**Figure V.6a.** Amount of components in the product gas stream at various inlet temperatures. Residence time = 1 ms.  $\text{CH}_4:\text{H}_2 = 1\text{ mol} : 1\text{ mol}$ ,  $P = 1\text{ atm}$ .

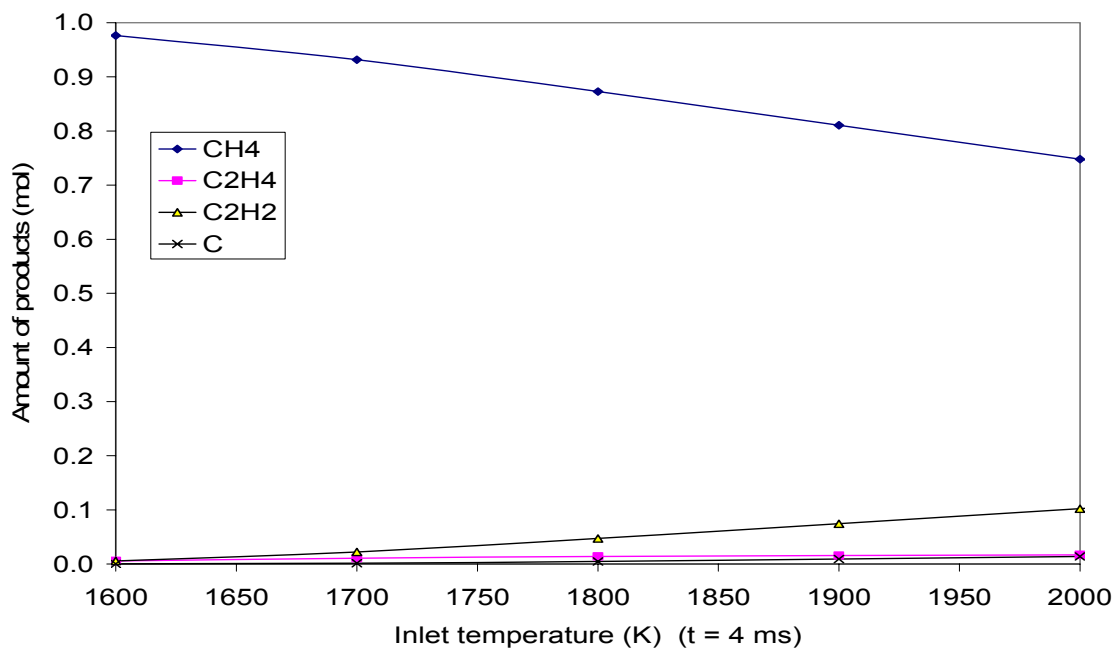


**Figure V.6b.** Amount of components in the product gas stream at various inlet temperatures. Residence time = 4 ms.  $\text{CH}_4:\text{H}_2 = 1\text{ mol} : 1\text{ mol}$ ,  $P = 1\text{ atm}$ .

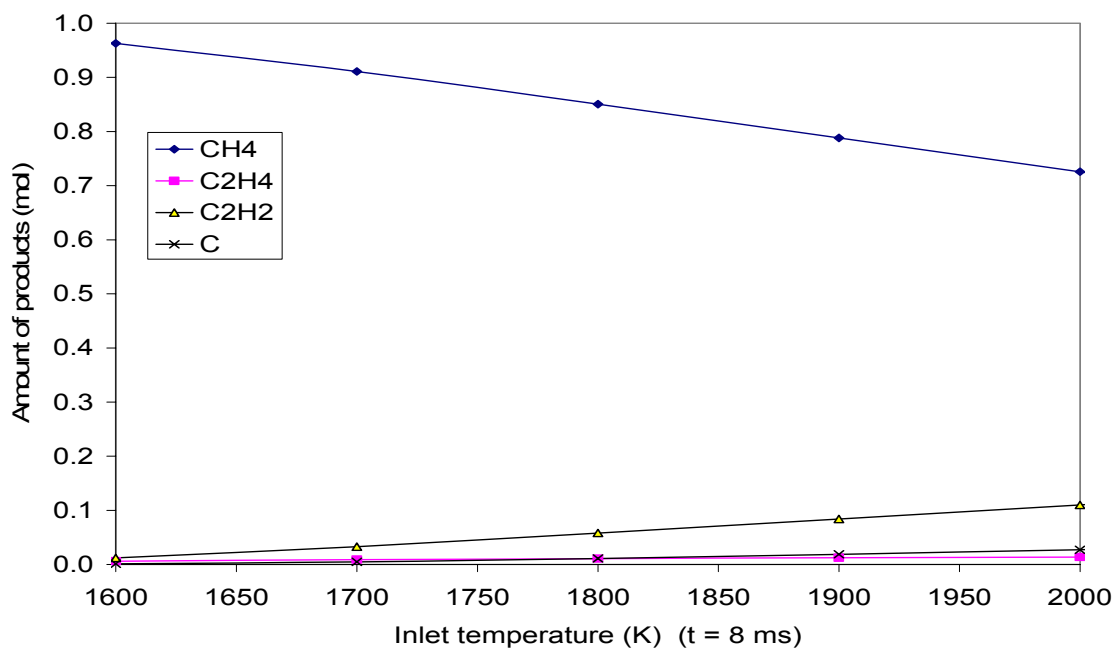


**Figure V.6c.** Amount of components in the product gas stream at various inlet temperatures. Residence time = 8 ms.  $\text{CH}_4:\text{H}_2 = 1\text{ mol} : 1\text{ mol}$ ,  $P = 1\text{ atm}$ .

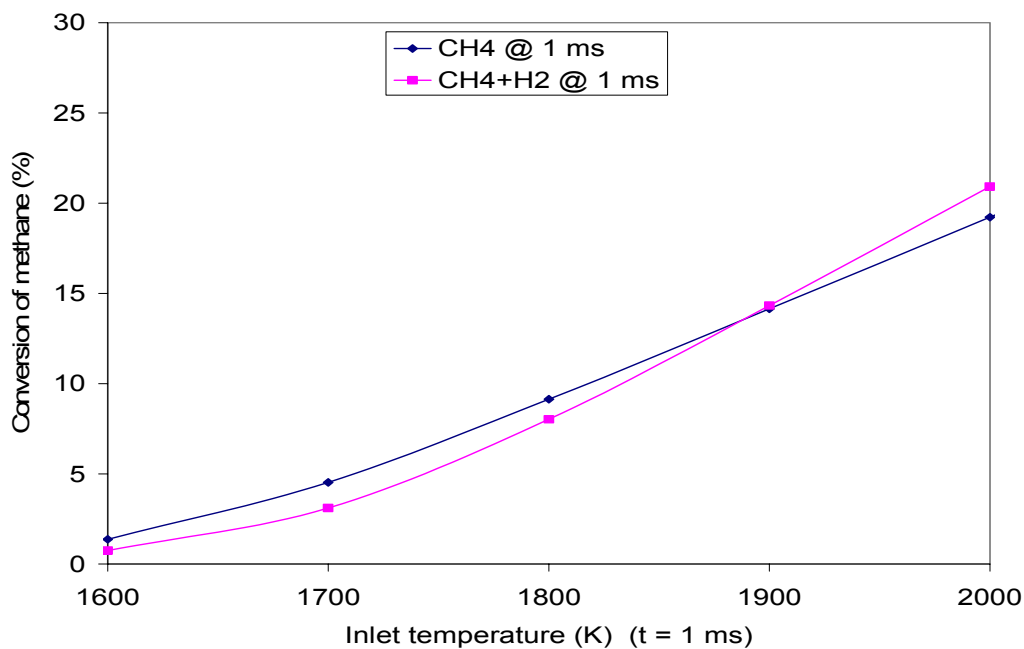


**Figure V.7a.** Comparison of methane conversion at various inlet temperatures. Residence time = 1 ms.  $\text{CH}_4:\text{H}_2 = 1\text{mol} : 1\text{mol}$  for the mixture feed case,  $P = 1\text{atm}$ .

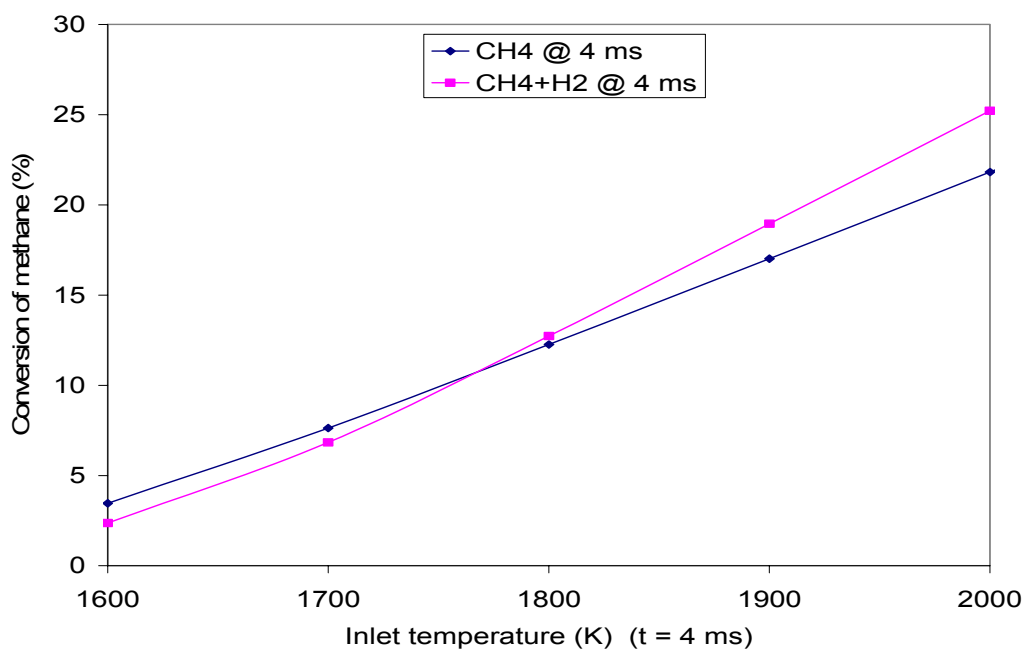


**Figure V.7b.** Comparison of methane conversion at various inlet temperatures. Residence time = 4 ms.  $\text{CH}_4:\text{H}_2 = 1\text{mol} : 1\text{mol}$  for the mixture feed case,  $P = 1\text{atm}$ .

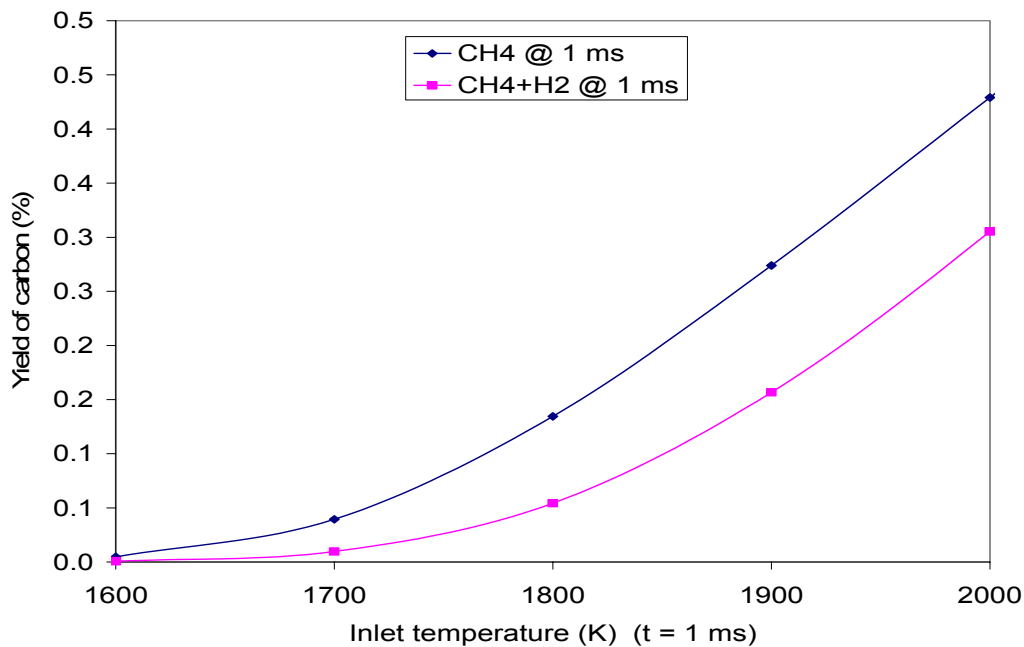


**Figure V.8a. Comparison of carbon formation at various inlet temperatures. Resident time = 1 ms. CH<sub>4</sub>:H<sub>2</sub> = 1 mol : 1 mol for the mixture feed case, P = 1 atm.**

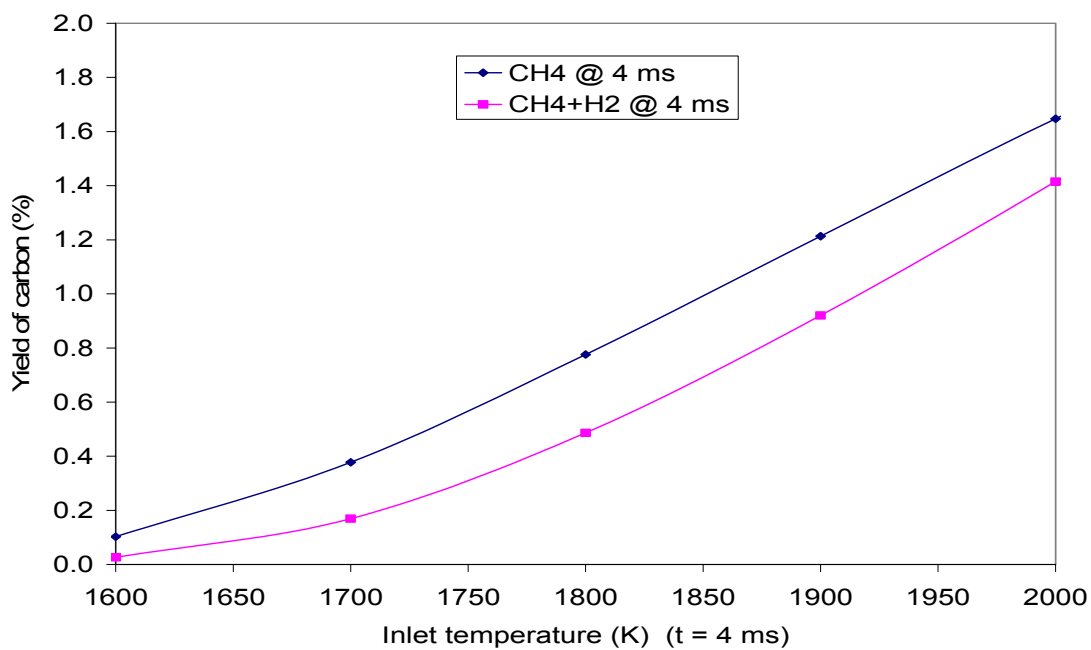


**Figure V.8b. Comparison of carbon formation at various inlet temperatures. Resident time = 4 ms. CH<sub>4</sub>:H<sub>2</sub> = 1 mol : 1 mol for the mixture feed case, P = 1 atm.**

## Rich Gas Feed

As we mentioned in Chapter I, methane is the major component of lean natural gas, yet rich natural gas may contain up to 30% of some other  $C_2+$  hydrocarbons. These hydrocarbons include ethane, propane, butane and very small amount of  $C_5+$  hydrocarbons. These higher hydrocarbons have much lower thermal stability than methane, thus they will quickly decompose at the high temperatures used for methane pyrolysis.

To simulate the pyrolysis of rich natural gas we use the gas composition similar to that from a gas field in Bryan, Texas. By neglecting the trace amounts of  $C_5+$  hydrocarbons and other impurities, we normalized the gas composition to be 71.59%  $CH_4$ , 14.10%  $C_2H_6$ , 10.29%  $C_3H_8$  and 4.02%  $C_4H_{10}$ , which add up to 100%.

Prior simulation results (Mossaad, 2002) have shown that the major products of rich gas pyrolysis are similar to those of methane pyrolysis, indicating that the ethane, propane and butane etc. will also decompose to form  $C_2$  hydrocarbon which is mainly ethylene. Thermodynamic analysis indicates the possibility of such decomposition reactions. It is also found that the conversion from ethane, propane and butane to ethylene is very fast. For example, the kinetic rate for conversion from ethane to ethylene is found 400 times that for methane conversion to ethylene. Thus in the following simulation we will assume that the rich components ( $C_2H_6$ ,  $C_3H_8$  &  $C_4H_{10}$ ) in the feed will decompose instantaneously into ethylene at the entrance of the cracker, while methane will go through the reactor for further pyrolysis.

Again our simulation will be based on 1 mol rich natural gas feed. Thus the amount of each component in the feed will be as follows:  $n_{CH_4}^0 = 0.7159$  mol,

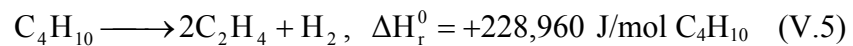
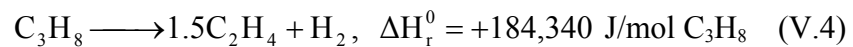
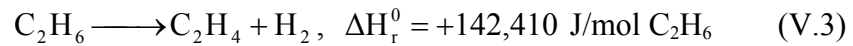
$n_{C_2H_6}^0 = 0.1410$  mol,  $n_{C_3H_8}^0 = 0.1029$  mol and  $n_{C_4H_{10}}^0 = 0.0402$  mol. As the three rich components are assumed to be converted to ethylene instantaneously at the entrance of the cracker, they will immediately produce ethylene and hydrogen whose amounts can be calculated by the following equations according to carbon and hydrogen elements balance:

$$n_{C_2H_4}^0 = n_{C_2H_6}^0 + 1.5n_{C_3H_8}^0 + 2n_{C_4H_{10}}^0 \quad (IV.34)$$

$$n_{H_2}^0 = n_{C_2H_6}^0 + n_{C_3H_8}^0 + n_{C_4H_{10}}^0 \quad (IV.35)$$

These two initial values will be used to solve the five differential equations for material balance.

The energy balance  $H_{in} = H_{out}$  can be calculated as follows. First, since the three rich components are assumed to decompose to ethylene immediately at the feed entrance of the reactor, a temperature drop should be expected due to the strong endothermic nature of the three decomposition reactions as shown below:



The  $\Delta H_r^0$  values here are for temperature of 300 K. However, their values change very little over a wide range of temperatures so they can be viewed as the same in our reaction temperature range. Thus for the gas feed before the rich components' conversion, the total enthalpy of the gas feed will be the sum of the separate enthalpies of all its components, i.e.

$$H_{in} = H_{CH_4}(T_{in})n_{CH_4}^0 + H_{C_2H_6}(T_{in})n_{C_2H_6}^0 + H_{C_3H_8}(T_{in})n_{C_3H_8}^0 + H_{C_4H_{10}}(T_{in})n_{C_4H_{10}}^0 \quad (V.6)$$

of which the molar enthalpies  $H_i$  ( $i = \text{CH}_4, \text{C}_2\text{H}_6, \text{C}_3\text{H}_8 \& \text{C}_4\text{H}_{10}$ ) are values calculated at the inlet temperature and their expressions are provided in Chapter IV.

Immediately after the rich components' conversion, the total enthalpy of the gas stream can be expressed as below:

$$H'_{\text{in}} = H_{\text{CH}_4}(T_0)n_{\text{CH}_4}^0 + H_{\text{C}_2\text{H}_6}(T_0)n_{\text{C}_2\text{H}_6}^0 + H_{\text{C}_3\text{H}_8}(T_0)n_{\text{C}_3\text{H}_8}^0 + H_{\text{C}_4\text{H}_{10}}(T_0)n_{\text{C}_4\text{H}_{10}}^0 \\ + (142,410)n_{\text{C}_2\text{H}_6}^0 + (184,340)n_{\text{C}_3\text{H}_8}^0 + (228,960)n_{\text{C}_4\text{H}_{10}}^0 \quad (\text{V.7})$$

where  $T_0$  is the temperature after the rich components conversion and it will be regarded as the “real” inlet temperature for the calculation of the kinetic rate constants for further pyrolysis reactions.

To calculate the exit temperature of the product gas stream leaving the cracker we calculate the term  $H_{\text{out}}$  by the following equation:

$$H_{\text{out}} = H_{\text{CH}_4}(T_{\text{out}})n_{\text{CH}_4}^0 + H_{\text{C}_2\text{H}_6}(T_{\text{out}})n_{\text{C}_2\text{H}_6}^0 + H_{\text{C}_3\text{H}_8}(T_{\text{out}})n_{\text{C}_3\text{H}_8}^0 + H_{\text{C}_4\text{H}_{10}}(T_{\text{out}})n_{\text{C}_4\text{H}_{10}}^0 \\ + (142,410)n_{\text{C}_2\text{H}_6}^0 + (184,340)n_{\text{C}_3\text{H}_8}^0 + (228,960)n_{\text{C}_4\text{H}_{10}}^0 \\ + (108,820)(n_{\text{CH}_4}^0 - n_{\text{CH}_4}) + (187,070)n_{\text{C}_2\text{H}_2} + (-17,740)n_{\text{C}} \quad (\text{V.8})$$

where the terms in the last line are the separate enthalpies using ethylene as the reference substance.

Based on the above considerations and assumptions we ran the simulator and obtained results as illustrated in the following figures.

Figures V.9 a & b show the change of amount of each component in the product gas stream at various inlet temperatures at selected residence times. Comparing them with the results for the pure methane feed as shown in Figure V.1, it is seen that the trend of change of each curve is similar. However, the conversion of methane for the rich gas



feed is much lower than for the pure methane feed case, and so the amount of each product is much smaller at the same temperature.

Figures V.10 a & b show the conversion of methane at various inlet temperatures at selected residence times. Comparing them with the corresponding figures for the case of pure methane feed, we also observe that the methane conversion for the rich gas case is much lower than the pure methane feed case at the same inlet temperature. This means that presence of the rich components like ethane, propane and butane, etc. has inhibited the conversion of methane. This may be explained by the strong endothermic effects of the conversion from these rich components to form ethylene as we assumed above. These reactions absorb a lot of energy from the gas feed thus greatly lower the temperature of the gas feed. This causes the kinetic rate constants for further methane conversion to drop by many orders of magnitude, leading to very low conversion of methane as compared to the pure methane feed situation.

We did not try to compare the yield of ethylene, acetylene and carbon due to the difficulty to define the yields here because of the presence of the rich components. However, it is obvious that the formation of these three products should be much lower than the pure methane feed case for the same reason given above.

In summary, the rich components in the natural gas can inhibit the conversion of methane and the yield of products. This conclusion is consistent with the findings of Holmen (1995) and Mossaad (2002), etc. in their research work.

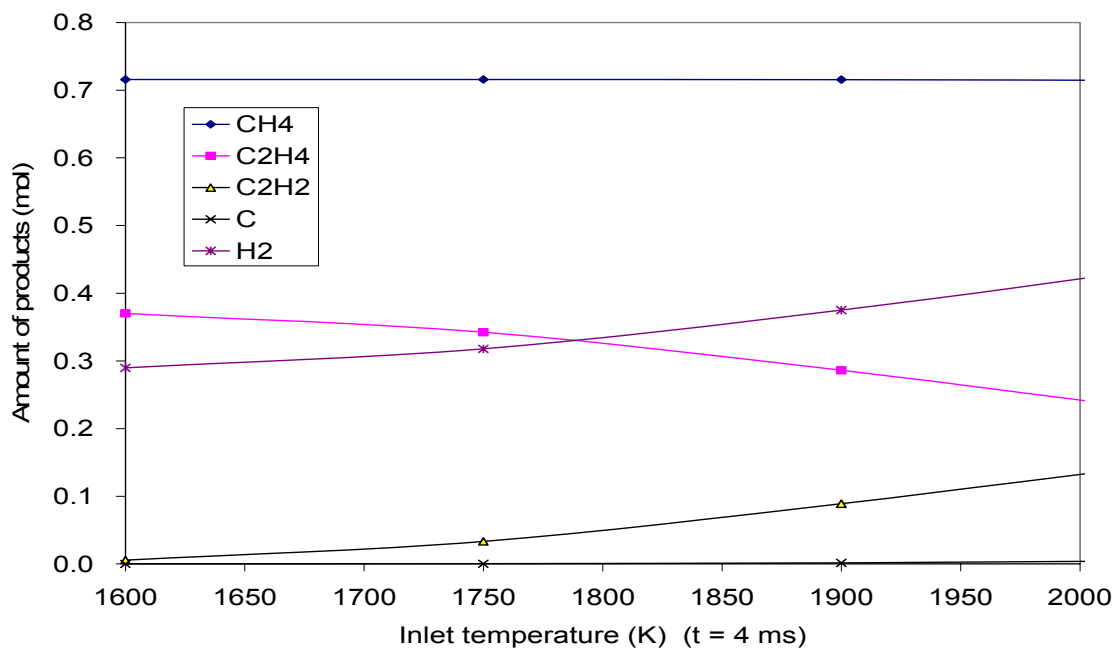


Figure V.9a. Amount of components in the product gas stream at various inlet temperatures. Residence time = 4 ms. P = 1atm.

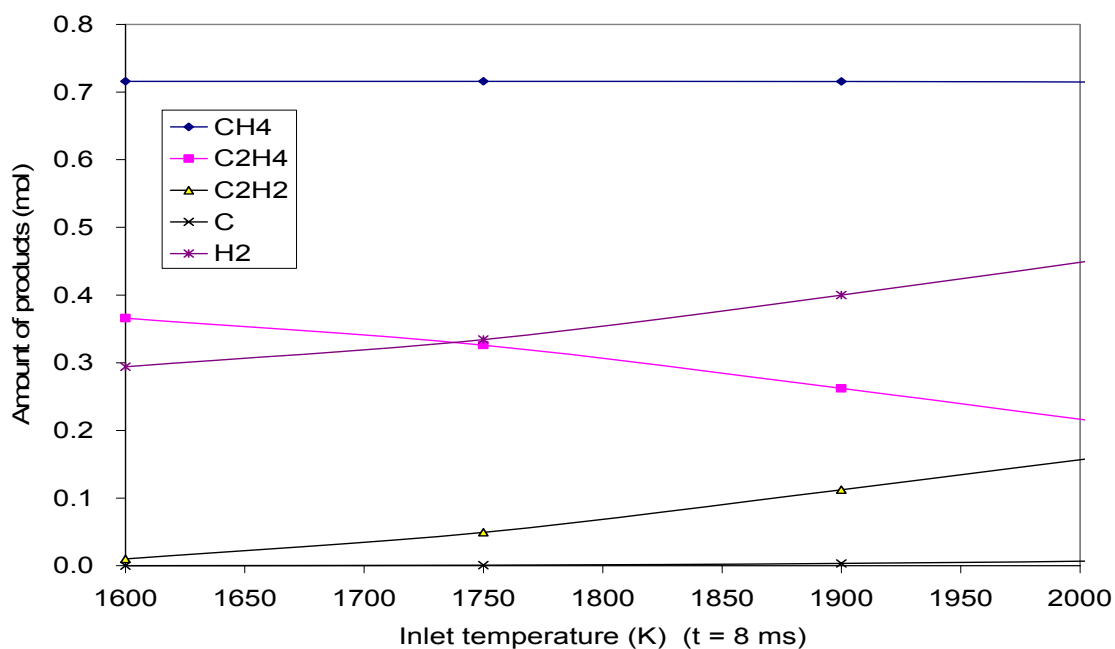
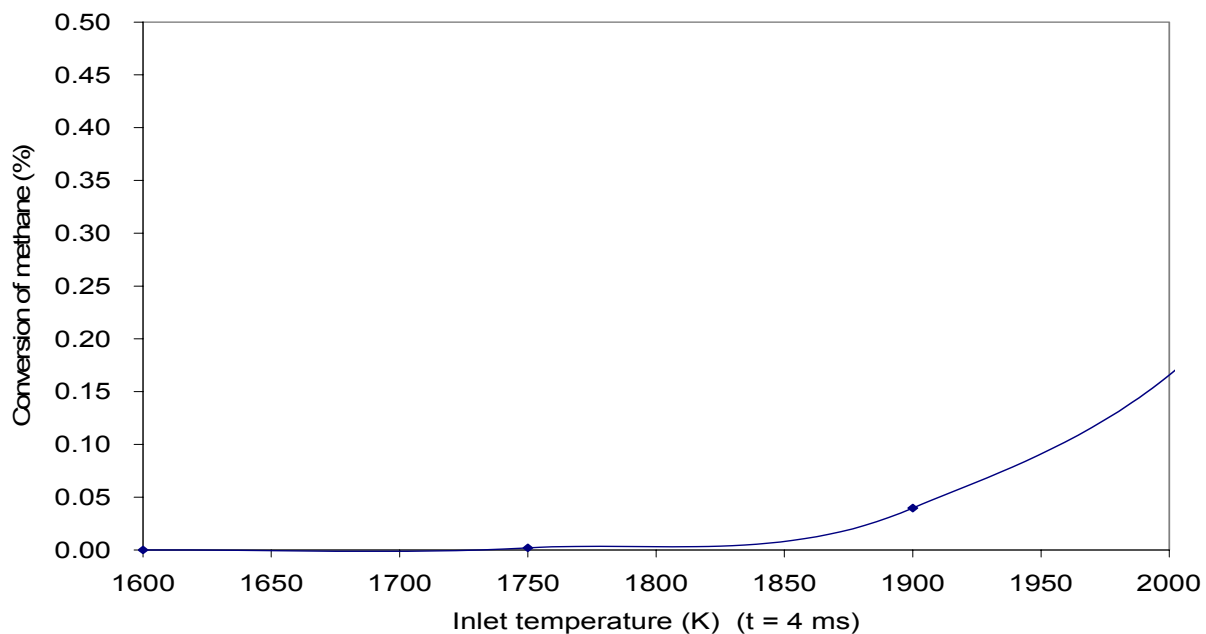
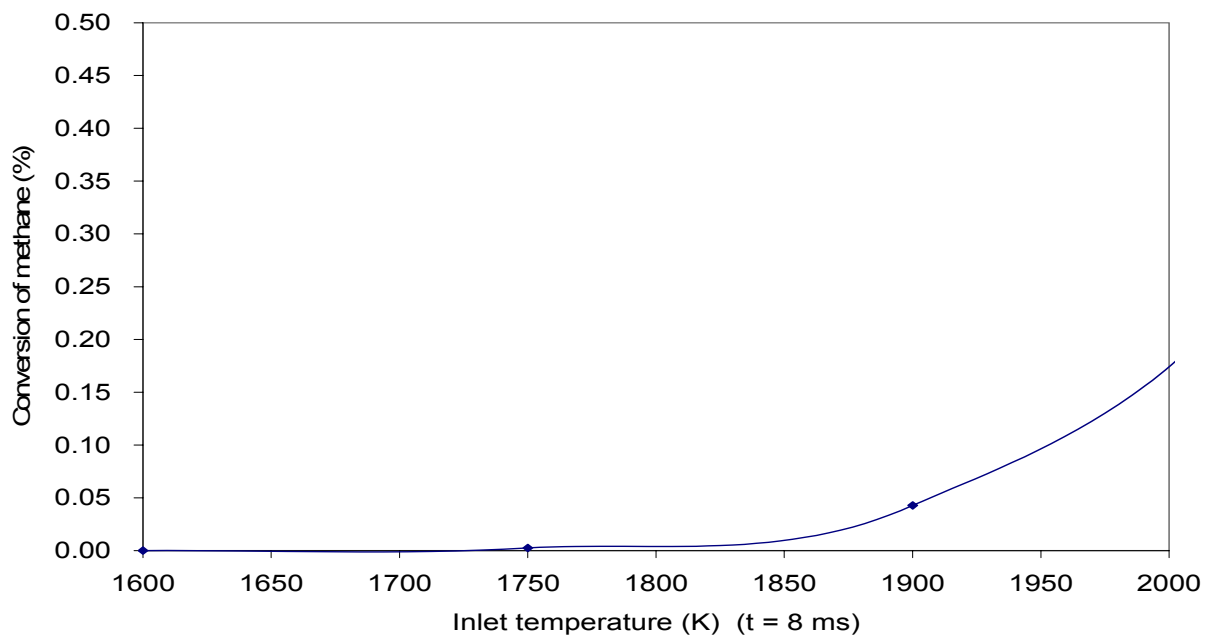


Figure V.9b. Amount of components in the product gas stream at various inlet temperatures. Residence time = 8 ms. P = 1atm.



**Figure V.10a. Conversion of methane at various inlet temperatures. Residence time = 4 ms. P = 1atm.**

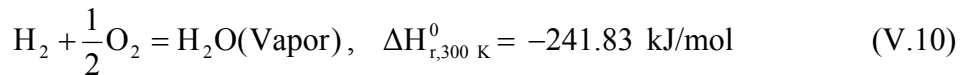
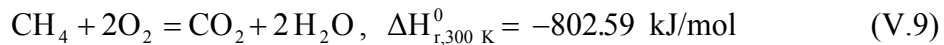


**Figure V.10b. Conversion of methane at various inlet temperatures. Residence time = 8 ms. P = 1atm.**

### Pure Methane Feed with a Combustion Zone

Now we include a combustion zone in the reaction system as shown in Figure IV.6. The burner is supposed to burn fuel in air or pure oxygen to provide enough energy to heat the fresh natural gas of the cracker up to the required high temperature for further pyrolysis. Two types of fuels may be used – either lean natural gas (methane) or hydrogen recovered from the pyrolysis reactions. The latter is more favorable for several reasons: 1) it is very plentiful as each stepwise decomposition of methane produces hydrogen, 2) burning of hydrogen does not produce any pollutants, the only product water may prove to be very precious in some dry places where huge remote gas reserves are often found such as in the big deserts in the middle east. Hydrogen can be separated from the cracker's product gas stream and recycled to the inlet of the burner for combustion purpose.

The reactions of burning methane and hydrogen can be expressed as below:



To calculate the moles of fuel  $n_B$  that must be burned per mol of natural gas feed to be cracked in the reactor, we take the procedures as follows. Assume that the complete combustion to occur at temperature  $T$  with stoichiometric oxygen. Then the effective heat of combustion can be calculated as  $\Delta H_c^E = \Delta H_c + \Delta H_s$ , in which  $\Delta H_c$  is the heat of combustion at  $T$  and  $\Delta H_s$  is the heat required to take the product from  $T$  to its final temperature equal to the inlet temperature to the cracker. This effective heat term  $\Delta H_c^E$  is

the amount of energy used to raise the temperature of the natural gas feed to its inlet temperature to the cracker.

To simulate the operations of the pilot plant, we only consider the burning in a pure oxygen environment. Assume the combustion starts at 300 K or 1000 K (with preheating) and we also choose the final temperature with two possible values – 1750 K or 2000 K, then six values for the  $\Delta H_c^E$  are shown in Table V.1.

**Table V.1. Excess Heat of Combustion of CH<sub>4</sub> and H<sub>2</sub> at Selected Initial and Final Temperatures**

Fuel type	Initial T (K)	Final T (K)	$\Delta H_c^E$ (kJ/mol)
CH <sub>4</sub>	300	1750	605.67
		2000	565.31
	1000	1750	690.87
		2000	650.52
H <sub>2</sub>	300	1750	181.55
		2000	168.86
	1000	1750	207.49
		2000	194.80

Then we need to calculate the sensible enthalpy change  $\Delta H_S^{NG}$  to heat one mole of natural gas from 300 K (or 1000 K with preheating) to the same final temperature (say 1750 K or 2000 K) using the TRC Tables. These values are listed in Table V.2.

Now we can calculate  $n_B$  by the equation  $n_B(\Delta H_c^E)E_B = \Delta H_S^{NG}$ , where  $E_B$  is the burner efficiency, here taken to be 70%. Depending upon the various options mentioned above, the values of  $n_B$  are listed in Table V.3.

If the burner efficiency is different from 70%, then multiply the above figures by the corresponding factor to calculate the required  $n_B$ .

**Table V.2. Sensible Heat Required to Heat One Mole of Natural Gas (Lean or Rich) from Selected Initial and Final Temperatures**

Feed to the Cracker	Initial T (K) (Before mixing with flame)	Final T (K) (After mixing with flame)	$\Delta H_S^{NG}$ (kJ/mol)
Lean Natural Gas (Methane)	300	1750	102.14
		2000	126.54
	1000	1750	63.73
		2000	88.13
Rich Natural Gas (JAB-Ranch)	300	1750	124.85
		2000	147.81
	1000	1750	74.6
		2000	97.56

**Table V.3. Amount of H<sub>2</sub> or CH<sub>4</sub> Fuel Required to Heat One Mole of Natural Gas (Lean or Rich) from Selected Initial and Final Temperatures**

Initial T (K)	Final T (K)	Hydrogen Fuel		Methane Fuel	
		Lean Gas	Rich Gas	Lean Gas	Rich Gas
300	1750	0.80	0.98	0.24	0.29
1000	1750	0.44	0.51	0.13	0.15
300	2000	1.07	1.25	0.32	0.37
1000	2000	0.65	0.72	0.20	0.22

Table V.4 lists the results corresponding to the amount of burned fuels in the above table. Case I & III are the results of lean gas pyrolysis when either hydrogen or methane fuel is combusted in the burner, Case II & IV are the results of rich gas (JAB-Ranch) pyrolysis with hydrogen or methane as the fuel in the burner.

From the results of Case I it is easily seen that for the same gas temperature to the cracker (say 1750 K or 2000 K), the case without preheating (i.e.  $T_{in, burner} = 300$  K) always has a higher methane conversion than the case with preheating (i.e.  $T_{in, burner} = 1000$  K). This is because it requires more fuel to reach the same final temperature without preheating compared to the case with preheating. More fuel produces more water; since

water has a high molar heat capacity, it can help to keep the reaction stream's temperature to drop more slowly during methane's pyrolysis. And as demonstrated in the simulation in previous sections, higher temperature always leads to higher methane conversion since the overall pyrolysis is an endothermic process.

It is obvious that methane conversion will be higher for higher gas inlet temperature to the cracker (comparing the lines with  $T_{\text{out, burner}} = 2000 \text{ K}$  &  $1750 \text{ K}$  respectively) due to the same reason given in the previous paragraph.

However, if we compare Case I with Case III or Case II with Case IV, we find that methane conversion are very close to each other as long as the gas inlet/outlet temperatures to the burner are the same, no matter which type of fuel ( $\text{CH}_4$  or  $\text{H}_2$ ) is burned. This is because identical inlet/outlet temperatures to the burner produce identical amount of energy supplied to the reaction zone, thus leading to approximately the same conversion of methane. The minor difference between the conversions is caused by the different amounts of combustion products ( $\text{H}_2\text{O}$  for hydrogen fuel or  $\text{H}_2\text{O} + \text{CO}_2$  for methane fuel) entering the reaction zone.

The analysis of the other three cases reveals similar results to that of Case I. Thus we conclude that a burner is beneficial to the natural gas pyrolysis by providing energy to the endothermic reaction system. The more energy is supplied to the reaction zone, the higher methane conversion can be achieved. In addition, steam produced in the burner can maintain the reaction system's temperature at a relatively high level due to its large molar heat capacity, thus also leading to higher conversion of methane.

**Table V.4. Results of Natural Gas Pyrolysis with Energy Provided from A Burner**

<b>Case I: Lean gas (CH<sub>4</sub>), H<sub>2</sub> fuel (H<sub>2</sub>+0.5 O<sub>2</sub> = H<sub>2</sub>O) (Basis: 1 mol CH<sub>4</sub>)</b>								
T <sub>in</sub> /T <sub>out</sub> for Burner (K)	Amount of Fuel n <sub>B</sub> (mol)	T <sub>out</sub> of Cracker (K)	Out of Cracker					CH <sub>4</sub> Conversion (%)
			CH <sub>4</sub>	C <sub>2</sub> H <sub>4</sub>	C <sub>2</sub> H <sub>2</sub>	C	H <sub>2</sub>	
300/1750	0.8	1559.2	0.6463	0.0244	0.1447	0.0157	0.5141	35.4
1000 /1750	0.44	1571.8	0.7703	0.0133	0.0949	0.0135	0.3381	23.0
300/2000	1.07	1338.4	0.1378	0.1949	0.2336	0.0054	1.1012	86.2
1000 /2000	0.65	1337.7	0.2438	0.2451	0.1314	0.0032	0.8908	75.6
<b>Case II: Rich gas, H<sub>2</sub> fuel (H<sub>2</sub> +0.5 O<sub>2</sub> = H<sub>2</sub>O) (Basis: 1 mol rich gas)</b>								
T <sub>in</sub> /T <sub>out</sub> for Burner (K)	Amount of Fuel n <sub>B</sub> (mol)	T <sub>out</sub> of Cracker (K)	Out of Cracker					CH <sub>4</sub> Conversion (%)
			CH <sub>4</sub>	C <sub>2</sub> H <sub>4</sub>	C <sub>2</sub> H <sub>2</sub>	C	H <sub>2</sub>	
300/1750	0.98	1397.0	0.6524	0.1635	0.2382	0.0117	0.5974	8.9
1000 /1750	0.51	1346.1	0.7124	0.2354	0.1401	0.0039	0.4316	0.5
300/2000	1.25	1256.6	0.1654	0.3120	0.3362	0.0054	1.1763	76.9
1000 /2000	0.72	1348.5	0.4041	0.2925	0.2351	0.0081	0.8392	43.6
<b>Case III: Lean gas (CH<sub>4</sub>), CH<sub>4</sub> fuel (CH<sub>4</sub> + 2O<sub>2</sub> = CO<sub>2</sub> + 2H<sub>2</sub>O) (Basis: 1 mol CH<sub>4</sub>)</b>								
T <sub>in</sub> /T <sub>out</sub> for Burner (K)	Amount of Fuel n <sub>B</sub> (mol)	T <sub>out</sub> of Cracker (K)	Out of Cracker					CH <sub>4</sub> Conversion (%)
			CH <sub>4</sub>	C <sub>2</sub> H <sub>4</sub>	C <sub>2</sub> H <sub>2</sub>	C	H <sub>2</sub>	
300/1750	0.24	1560.1	0.6525	0.0228	0.1428	0.0162	0.5064	34.7
1000 /1750	0.13	1570.5	0.7746	0.0129	0.0931	0.0135	0.3320	22.5
300/2000	0.32	1332.9	0.1431	0.1981	0.2278	0.0052	1.0899	85.7
1000 /2000	0.2	1334.8	0.2416	0.2458	0.1317	0.0032	0.8933	75.8



**Table V.4. (Continued)**

<b>Case IV: Rich gas, CH<sub>4</sub> fuel (CH<sub>4</sub> + 2O<sub>2</sub> = CO<sub>2</sub> + 2H<sub>2</sub>O) (Basis: 1 mol rich gas)</b>								
T <sub>in</sub> /T <sub>out</sub> for Burner (K)	Amount of Fuel n <sub>B</sub> (mol)	T <sub>out</sub> of Cracker (K)	Out of Cracker					CH <sub>4</sub> Conversion (%)
			CH <sub>4</sub>	C <sub>2</sub> H <sub>4</sub>	C <sub>2</sub> H <sub>2</sub>	C	H <sub>2</sub>	
300/1750	0.29	1394.2	0.6609	0.1640	0.2336	0.0114	0.5841	7.7
1000 /1750	0.15	1341.8	0.7130	0.2398	0.1356	0.0037	0.4263	0.4
300/2000	0.37	1268.2	0.1736	0.3254	0.3188	0.0053	1.1505	75.8
1000 /2000	0.22	1348.0	0.4069	0.2908	0.2353	0.0083	0.8367	43.2

### Effect of Methane Recycling

From the previous sections we see that conversion of natural gas (whether lean or rich) in a single pass is relatively low – only about 19% for the pure methane case at a residence time of 1 ms and 2000 K, and much lower for the rich gas feed. This is far too low to meet the requirement for process commercialization. Most methane just passes through the cracker without any decomposition. If this part of methane is vented into the air or flared as a waste gas, it is not only uneconomical but produces much pollution to the environment. Thus, it is necessary to recycle unreacted methane back to the inlet of the cracker for another pass of pyrolysis. Below we will investigate the effect of methane recycling.

Assume that methane is separated from flue gas of the cracker and reheated to the same temperature as the fresh natural gas feed before the two streams of gases are mixed at the entrance of the cracker. Define the reflux ratio as

$$R = \frac{\text{Amount of methane recycled}}{\text{Amount of fresh natural gas feed}} \quad (\text{V.11})$$

Then by changing the value of  $R$  in our simulator we will be able to see the change of methane conversion. For easy comparison with the case without methane recycling and with infinite recycling (i.e. pure methane feed case), we set the residence time at 4 ms and assume 1 mol fresh rich gas feed of the same composition as in the previous simulation cases.

The following Figures V.11a – V.11c show the amount of each component in the product gas streams versus temperature with reflux ratio  $R = 1, 2$  &  $3$  respectively. We see that the trend of change of each component is similar to the cases of pure methane pyrolysis and rich gas pyrolysis with no recycling in both cases. The results of rich gas pyrolysis with methane recycling lie between those for pure methane pyrolysis and for rich gas pyrolysis whose results were shown in the previous sections. This is better seen in Figure V.12 where we show the conversion of methane for different reflux ratios on the same graph. The lower dashed line with  $R = 0$  corresponds to the case of rich gas pyrolysis in a single pass, the upper dashed line with  $R = \infty$  corresponds to the case of pure methane pyrolysis in a single pass (when  $R$  approaches infinity the original fresh rich gas feed is negligible). From this figure it is clearly seen that higher reflux ratio increases methane conversion under the same reaction temperature. When the reflux ratio is very large (say  $R = 100$ ) the conversion curve is very close to that for pure methane feed, although this situation is only of theoretical significance.

The effect of reflux ratio on methane conversion can be explained as follows. As we saw in the section of rich gas pyrolysis, the decompositions of the rich components (ethane, propane and butane, etc.) are very endothermic reactions. They absorb large amount of energy during the pyrolysis leading to a very rapid drop of the reaction

temperature. This sharp drop of temperature quenches the reaction very fast since methane decomposition requires high temperatures to advance. When methane is recycled into the inlet of the cracker, it is mixed with the fresh feed of rich gas and thus dilutes the rich components in the feed, leading to lower concentration of rich components and higher concentration of methane. This reduces the relative quenching effect imposed by the decomposition of the rich components. Less quenching by the rich components' decomposition leads to higher exit temperature and higher methane conversion. Therefore, higher reflux ratio means lower concentration of rich components relative to methane in the feed to the cracker, thus leading to higher conversion of methane. The ultimate limit of increasing the reflux ratio is when  $R$  approaches infinity which is equivalent to the case of pure methane feed.

In summary, higher reflux ratio will be beneficial to the increase of methane conversion. However, reflux ratio can not be increased indefinitely. There are some other limiting factors that need to be taken into account when trying to increase the reflux ratio. First, the amount of methane in the flue gas which is available for recycling depends on the cracking efficiency of each single pass. Second, each of the separation, preheating and pumping processes of the to-be-recycled methane will consume energy and requires additional mechanical equipment. Higher reflux ratio means more investment on the operating and capital costs of this equipment. Thus economic factors must be considered to find the optimal reflux ratio for each specific facility in commercial applications.

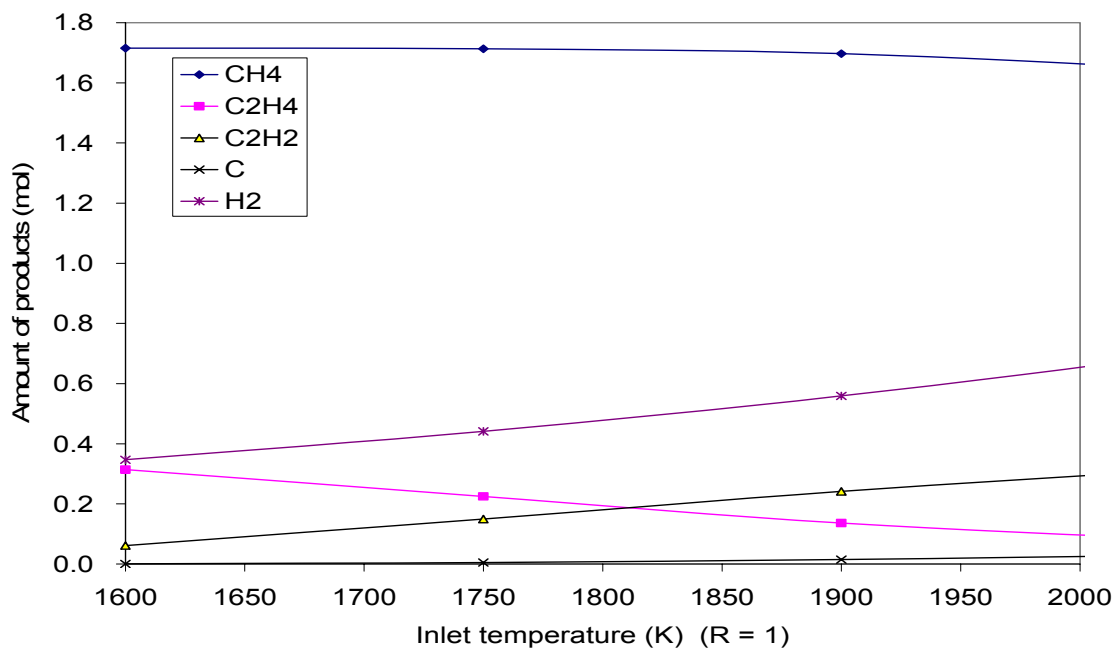


Figure V.11a. Amount of components in the product gas stream at various inlet temperatures. Residence time = 4 ms.  $P = 1\text{atm}$ , reflux ratio  $R = 1$ .

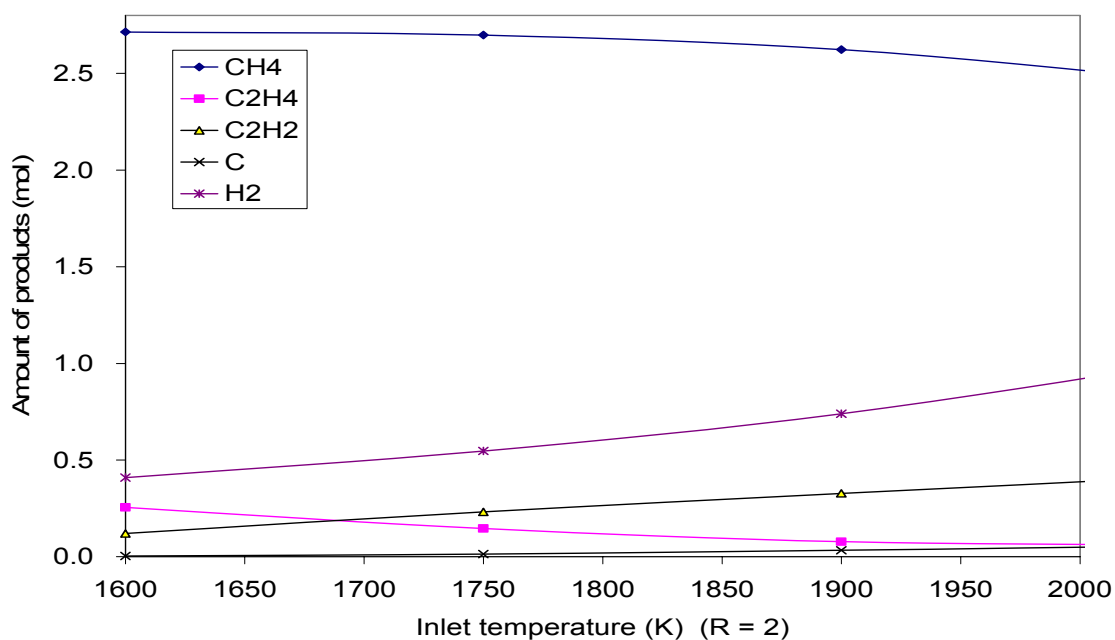


Figure V.11b. Amount of components in the product gas stream at various inlet temperatures. Residence time = 4 ms.  $P = 1\text{atm}$ , reflux ratio  $R = 2$ .

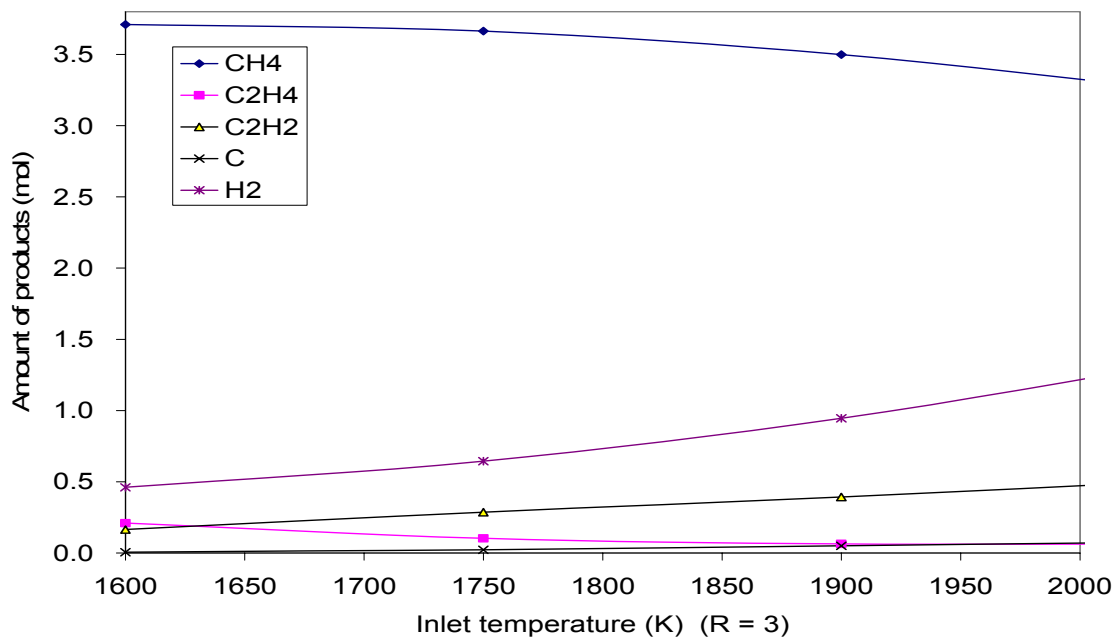


Figure V.11c. Amount of components in the product gas stream at various inlet temperatures. Residence time = 4 ms. P = 1atm, reflux ratio R = 3.

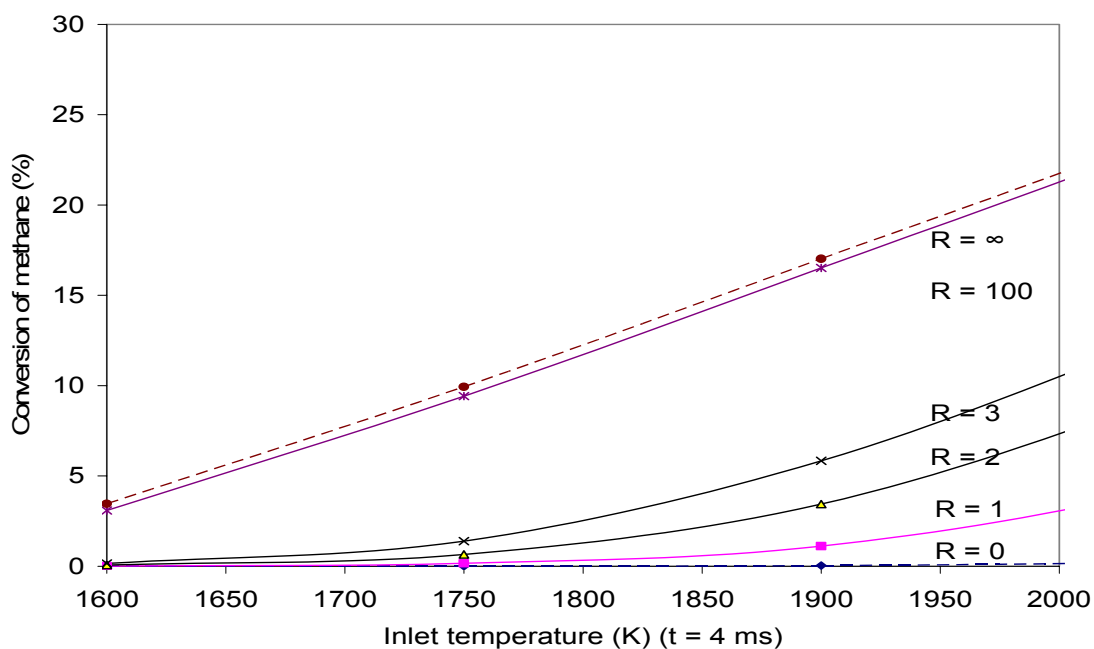
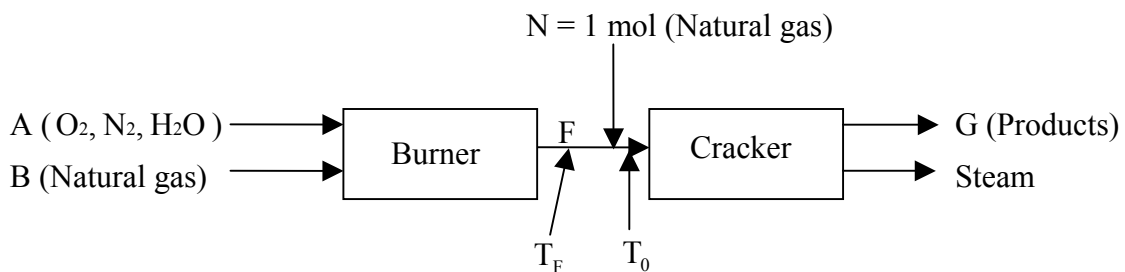


Figure V.12. Methane conversion versus temperature at various reflux ratios (t = 4 ms). The two dashed lines (R = 0 and R = ∞) are boundaries of the conversion curves.

### Simulation of Experimental Data from a Pilot Plant

A local pilot plant has done numerous experiments on rich gas pyrolysis in a thermal cracker. Their reaction conditions are as follows: residence time = 4 ms; reaction occurred without recycling of methane (only a single pass); a burner was used to supply energy to the fresh natural gas feed and raise its temperature for proper decomposition in the cracker (Figure V.13).



**Figure V.13. Schematic diagram of reaction system for simulation of the pilot plant data.**

The compositions of the natural gas feed, the gas streams to the burner and the product stream are show in Table V.5.

The temperature of each process stream is as follows:

Inlet gas (stream N) & fuel (stream B): 40 °F (277.55 K)

Air (stream A) & steam (mixed with air): 300 °F (422.05 K)

Cracked gas (stream G): 1800 °F (1255 K)

The fuel was burned together with air with unknown compositions of oxygen and nitrogen. Steam was also added to the air by a ratio of  $n_{\text{H}_2\text{O}} = 2.75 n_{\text{O}_2}$ . Assume 1 mol fresh natural gas was fed to the cracker ( $N = 1 \text{ mol}$ ). Then according to the volumetric

flowrates of stream N and B provided in the above table the amount of fuel fed to the burner should be

$$B = 1 \text{ mol} \times (12/26) = 0.4615 \text{ mol.}$$

**Table V.5. Compositions of Feedstock and Product Gas Streams of a Pilot Run**

Components	Inlet Gas (mol%) (N)	Fuel (mol) (B)	Cracked Gas (mol%) (G) (On a dry basis)
Hydrogen	0.650	0.650	24.329
Carbon dioxide	2.650	2.650	20.156
Oxygen/Argon	0.007	0.007	0.340
Methane	76.478	76.478	25.802
Nitrogen	1.392	1.392	13.265
Ethane	11.450	11.450	0.207
Ethylene	0.000	0.000	3.047
Propane	6.099	6.099	0.006
Propylene	0.000	0.000	0.074
Acetylene	0.000	0.000	4.178
Isobutane	0.394	0.394	0.059
n-butane	0.769	0.769	0.001
C <sub>4</sub> olefins	0.000	0.000	0.000
Carbon monoxide	0.000	0.000	8.323
Isopentane	0.054	0.054	0.109
n-pentane	0.036	0.036	0.000
1-3-butadiene	0.000	0.000	0.025
C <sub>5</sub> 's	0.000	0.000	0.018
C <sub>6</sub> 's	0.022	0.022	0.061
Flowrate (MSCFD)	26.000	12.000	

Now let us carry out material balance to calculate the molar amount of the other gas streams.

We assume 1 mol fresh natural gas feed ( $N = 1 \text{ mol}$ ) as our basis of calculation. Then the amount of fuel required is  $B = 0.4615 \text{ mol}$ . Assume there were  $m$  mol oxygen and  $n$  mol nitrogen in the air at the inlet of the burner, then the amount of steam fed to the

burner was  $2.75m$  mol. We also assume that the product gas stream G to be  $x$  mol on a dry basis and the steam leaving the cracker to be  $y$  mol.

The compositions of the process streams by elements are summarized in Table V.6.

**Table V.6. Compositions of Process Streams Based on 1 mol Rich Gas Feed**

Process stream (1 mol basis)	Carbon (mol)	Hydrogen (mol)	Oxygen (mol)	Nitrogen (mol)
N	1.25559	4.37722	0.05314	0.02784
B	1.25559	4.37722	0.05314	0.02784
G	0.70726	1.77272	0.49315	0.2653

Thus by making material balance of each of the above elements according to the schematic diagram Figure V.12, we obtain the following equations:

$$\text{Carbon balance: } 1.25559 * (1 + 0.4615) = 0.70276x \quad (\text{V.12})$$

$$\text{Hydrogen balance: } 4.37722 * (1 + 0.4615) + 2.75m * 2 = 1.77272x + 2y \quad (\text{V.13})$$

$$\text{Oxygen balance: } 0.05314 * (1 + 0.4615) + 2.75m + 2m = 0.49315x + y \quad (\text{V.14})$$

$$\text{Nitrogen balance: } 0.02784 * (1 + 0.4615) + 2n = 0.2653x \quad (\text{V.15})$$

Solving the above four equations we get  $m = 1.05039$ ,  $n = 0.32383$ ,  $x = 2.59458$  and  $y = 3.78748$ . Thus the amount of each process stream is as follows:

Inlet natural gas to the cracker (N): 1 mol

Fuel gas fed to the burner (B): 0.4615 mol

O<sub>2</sub> fed to the burner: 1.05039 mol

N<sub>2</sub> fed to the burner: 0.32383 mol

Steam fed to the burner: 2.88857 mol



Cracked gas (G) (dry basis): 2.59458 mol

Steam out from the cracker: 3.78748 mol

Further analysis of material balance reveals that the fuel is not completely combusted in the burner to form  $\text{CO}_2$ , but some CO is also formed. Through careful calculation we obtained the composition of the flame (stream F) as follows:

Composition of flame F:

$\text{H}_2\text{O}$ : 3.89882 mol

$\text{N}_2$ : 0.330254 mol

$\text{CO}_2$ : 0.483319 mol

CO: 0.096131 mol

$\text{O}_2$ : 0.00864 mol

Summing up both streams N & F we obtain the composition of the real gas fed to the cracker as follows:

$\text{CH}_4$ : 0.76478 mol

$\text{C}_2\text{H}_6$ : 0.1145 mol

$\text{C}_3\text{H}_8$ : 0.06099 mol

$\text{C}_4+$ : 0.01275 mol

$\text{CO}_2$ : 0.51 mol

CO: 0.09613 mol

$\text{H}_2$ : 0.0065 mol

$\text{N}_2$ : 0.344174 mol

$\text{O}_2$ : 0.00871 mol

$\text{H}_2\text{O}$ : 3.89862 mol

The amount of components in the product gas stream leaving the cracker can now be calculated and the results for the major components of interest are shown below:

CH<sub>4</sub>: 0.669454 mol

C<sub>2</sub>H<sub>4</sub>: 0.079507 mol

C<sub>2</sub>H<sub>2</sub>: 0.108402 mol

Carbon: N/A

H<sub>2</sub>: 0.631235 mol

CO: 0.215947 mol

CO<sub>2</sub>: 0.522964 mol

H<sub>2</sub>O: 3.78748 mol

Now let us take on the energy balance to calculate the flame temperature  $T_f$  and the mixture gas temperature  $T_0$  at the inlet of the cracker.

As in the fuel to the burner (stream B) the amount of CO<sub>2</sub>, CH<sub>4</sub>, C<sub>2</sub>H<sub>6</sub> & C<sub>3</sub>H<sub>8</sub> add up to approximately 97% of the total composition, it is reasonable to neglect all the other minor components in the fuel for simplicity of further heat balance calculations. Let us normalize the composition of the fuel (stream B) to contain only the following components:

CH<sub>4</sub>: 79.11%

C<sub>2</sub>H<sub>6</sub>: 11.84%

C<sub>3</sub>H<sub>8</sub>: 6.31%

CO<sub>2</sub>: 2.74%

First we calculate the mixture temperature  $T_{\text{mix}}$  of streams A & B before they enter the burner. According to the temperature data from the pilot plant, stream A was 422.05 K and stream B was only 277.55 K before mixing at the inlet of the cracker. Thus upon mixing stream A would release some energy to be used to raise the temperature of stream B to a common value  $T_{\text{mix}}$ . The energy balance equation for this mixing process is as follows:

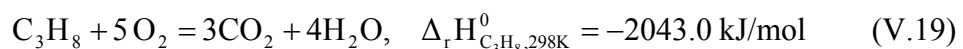
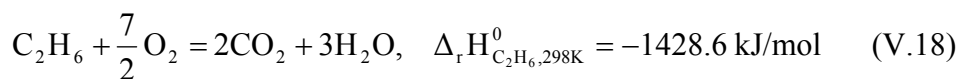
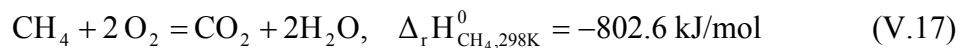
$$\begin{aligned} & (n_{\text{O}_2} C_{p,\text{O}_2} + n_{\text{N}_2} C_{p,\text{N}_2} + n_{\text{H}_2\text{O}} C_{p,\text{H}_2\text{O}}) (422.05 - T_{\text{mix}}) \\ & = (n_{\text{CH}_4} C_{p,\text{CH}_4} + n_{\text{C}_2\text{H}_6} C_{p,\text{C}_2\text{H}_6} + n_{\text{C}_3\text{H}_8} C_{p,\text{C}_3\text{H}_8} + n_{\text{CO}_2} C_{p,\text{CO}_2}) (T_{\text{mix}} - 277.05) \end{aligned} \quad (\text{V.16})$$

We can use the data of  $C_{p,298\text{K}}^*$  for each component to replace the  $C_{p,i}$  data in the above equation since this parameter does not change much in the temperature range from 298 K to  $T_{\text{mix}}$  for the above components. Thus after substitution of the  $C_{p,298\text{K}}^*$  data of each component found in Smith et al. (2001) and the molar data to solve the above equation, we obtain:

$$T_{\text{mix}} = 405.4 \text{ K}$$

Second we continue to calculate the flame temperature as follows.

From the TRC Tables we find the heats of reaction for the following three combustion reactions:



Again we find that the above heats of reaction change very little within the temperature range from 298 K to 405.4 K. So the total heat released from the combustion of the fuel (stream B) can be calculated as follows:

$$\Delta H_{\text{total}} = n_{\text{CH}_4} \Delta_r H_{\text{CH}_4, 298\text{K}}^0 + n_{\text{C}_2\text{H}_6} \Delta_r H_{\text{C}_2\text{H}_6, 298\text{K}}^0 + n_{\text{C}_3\text{H}_8} \Delta_r H_{\text{C}_3\text{H}_8, 298\text{K}}^0 \quad (\text{V.20})$$

Substitution of the data of the number of moles and the heats of reaction for each component then provides the total energy released from the combustion (based on 1 mol rich gas feed):

$$\Delta H_{\text{total}} = -430.58 \text{ kJ}$$

This energy is used to raise the temperature of the flue gas of the burner from 405.05 K to the final flame temperature  $T_F$  :

$$\eta(\Delta H_{\text{total}}) = \int_{405.05}^{T_F} (n_{\text{CO}} C_{p,\text{CO}} + n_{\text{CO}_2} C_{p,\text{CO}_2} + n_{\text{H}_2\text{O}} C_{p,\text{H}_2\text{O}} + n_{\text{N}_2} C_{p,\text{N}_2} + n_{\text{O}_2} C_{p,\text{O}_2}) dT \quad (\text{V.21})$$

Here  $\eta$  is the heat transfer efficiency of the burner and is assumed to be 80% for a conservative calculation. Substitution of the relevant data and by solving the above equation we get

$$T_F = 2036 \text{ K} .$$

Now we can calculate the temperature  $T_0$  of the mixture gas of stream N and stream F. Since stream N is only 277.55 K and stream F is 2036 K, it is obvious that the heat balance should be like this:

$$\int_{277.55}^{T_0} \sum_{\text{Stream N}} n_i C_{p,i} dT = \int_{T_0}^{T_F} \sum_{\text{Stream F}} n_i C_{p,i} dT ,$$

$i$  = each component in either stream N or F. (V.22)

Substitute relevant data into Eq. V.22 and solve it to obtain the mixture temperature at the inlet of the cracker

$$T_0 = 1609 \text{ K}$$

based on a burner efficiency of 80%. From the simulation results in the previous sections we know that natural gas would barely be decomposed at such a low temperature. Thus the plant's actual inlet temperature to the cracker should be much higher than the above value. Indeed, it is dubious that the temperature of the fresh natural gas can be as low as 277.55 K (40 °F) as given by the pilot plant. This might be the temperature during the transportation of natural gas from an external source to the pilot plant. It must have been preheated to a much higher temperature before it was fed to the cracker and the burner. Unfortunately this temperature is unavailable. Thus in the following simulation work we assume a number of values for this inlet temperature, and see if we can obtain gas composition to match that of the product stream G.

Substitute the moles and heat enthalpy data of all the components in the mixture of stream N and stream F into our simulator and by changing the inlet temperature, we obtain results as shown in Table V.7.

From Table V.7 we see that results of the row with the cracker's inlet temperature of 1948 K are very close to the plant data with respect to the compositions of methane and ethylene in the product gas stream, so is the methane conversion. But there is a very large positive error in the simulation result of acetylene, indicating that the moles of acetylene in the simulated case is much more than the amount obtained from the pilot plant experiment. This implies that some potential reaction involving consumption of acetylene may have actually occurred which resulted in the reduction of the amount of

acetylene in the product gas stream. This prediction will be proven to be somewhat reasonable in the next section.

**Table V.7. Results of Simulating Pilot Plant Data (Residence time = 4 ms)**

<b>T<sub>0</sub> (K)</b>	<b>CH<sub>4</sub> (mol)</b>	<b>C<sub>2</sub>H<sub>4</sub> (mol)</b>	<b>C<sub>2</sub>H<sub>2</sub> (mol)</b>	<b>Carbon (mol)</b>	<b>H<sub>2</sub> (mol)</b>	<b>CH<sub>4</sub> conversion (%)</b>
1600	0.7640	0.1929	0.0388	0.0003	0.2347	0.10
1750	0.7551	0.1378	0.0975	0.0020	0.3040	1.27
1900	0.7036	0.0850	0.1736	0.0071	0.4366	8.01
1948	0.6689	0.0746	0.2000	0.0096	0.5002	12.53
2050	0.5657	0.0615	0.2612	0.0166	0.6716	26.03
2200	0.3815	0.0476	0.3603	0.0305	0.9687	50.11
<b>Plant data</b>	0.6695	0.0791	0.1084	-	0.6312	12.46
<b>Error (%)</b>	-0.08	-5.60	84.46		-20.76	

Of which the relative error of the simulation results is defined as

$$\text{Error} = \frac{n_i(\text{simulation}) - n_i(\text{pilot plant})}{n_i(\text{pilot plant})} \times 100\%, \quad i = \text{CH}_4, \text{C}_2\text{H}_4 \dots$$

(V.23)

### **Simulation of Experimental Data from a Pilot Plant – Trying One New Reaction**

From the previous section it is assumed that a reaction involving the consumption of acetylene may have occurred in the cracker. Indeed, engineers in the pilot plant and our research group have been guessing what kind of reaction may have occurred. A close analysis of change of the compositions of the non-hydrocarbon components in both process streams entering and leaving the cracker revealed that such a potential reaction should also involve the participation of steam and carbon monoxide. Let's take a look at

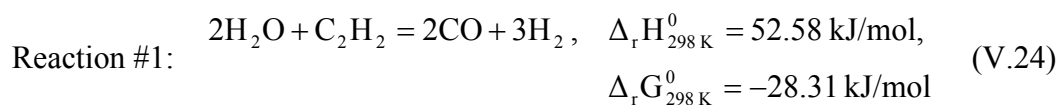
the composition changes of the non-hydrocarbon components in the inlet and outlet process streams shown in Table V.8.

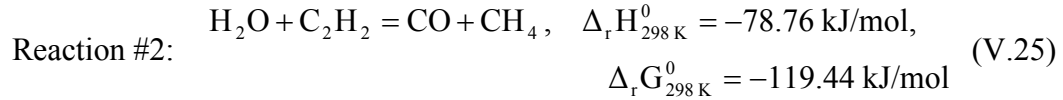
**Table V.8. Comparison of Compositions of Inlet and Outlet Process Streams to the Cracker**

Components	Moles in the inlet stream	Moles in the outlet stream	Change of Moles (Outlet – Inlet)
H <sub>2</sub>	0.0065	0.63124	0.62474
CO <sub>2</sub>	0.51	0.523	0.013
O <sub>2</sub> /Ar	0.0087	0.00882	0.00012
H <sub>2</sub> O	3.89862	3.78748	-0.11114
N <sub>2</sub>	0.34417	0.34417	0
CO	0.09613	0.21595	0.11982

From the above table we see that the reduction of steam (-0.00004 mol) is very close to the increase of carbon monoxide (0.11982 mol) between the two process streams, implying a reaction which consumes steam and produces carbon monoxide with a ratio of H<sub>2</sub>O:CO = 1:1 may have occurred in the cracker. To further explore the possibility of such a reaction we continue our simulation by adding one more reaction to our simulator as follows.

By searching the website of National Institute of Standards and Technology (NIST) ([www.nist.gov](http://www.nist.gov)), we found two reactions which involve the three species mentioned above, namely consuming H<sub>2</sub>O and C<sub>2</sub>H<sub>2</sub> and producing CO with a 1:1 ratio of H<sub>2</sub>O:CO. These two reactions are:





Literature ( Miller et al., 1989) indicated that both the above reactions are second order, and their rate constants are similar and can be expressed as

$$k_6 = c * 5.9 \times 10^{-6} T^3 \exp(1010/T) \text{ sec}^{-1}$$

in which  $c$  is a constant which will be fine-tuned to fit our simulator. For the following simulation results with reaction #1, we use  $c = 0.063$  and for reaction #2 we use  $c = 0.049$ .

To track the change of amount of steam we add another material balance equation to the simulator as below:

$$\frac{dn_{\text{H}_2\text{O}}}{dt} = -a * k_6 \frac{n_{\text{H}_2\text{O}} n_{\text{C}_2\text{H}_2}}{n_T^2} \quad (\text{V.26})$$

Here we ignore the reverse reaction and also do some fine tuning to the constant  $a$  to better simulate the results of the pilot plant. Some modifications were also made to the material balance equations for acetylene and hydrogen and to the energy balance equations in order to reflect the addition of the new reaction as shown above.

Table V.9 shows the results of simulation after adding the above reaction #1 & #2 respectively to our simulator using the original data from the local pilot plant.

From Table V.9 we see that the after adding Reaction #1, the amount of all the components except ethylene in the product gas stream are very close to the pilot plant data. The amount of ethylene is about 10% less than in the pilot plant result. While by adding Reaction #2 instead of reaction #1, the amount of all the components in the product gas stream is within 5% close to the pilot plant data, which should be deemed to



be in very good match with the plant results. Thus we think Reaction #2 rather than #1 might have occurred in the cracker in the pilot plant run.

**Table V.9. Results of Simulating Pilot Plant Data – One New Reaction Added  
(Residence time = 4 ms)**

<b>1. Results by adding Reaction #1 (<math>2\text{H}_2\text{O} + \text{C}_2\text{H}_2 = 2\text{CO} + 3\text{H}_2</math>):</b>							
$T_0$ (K)	CH <sub>4</sub> (mol)	C <sub>2</sub> H <sub>4</sub> (mol)	C <sub>2</sub> H <sub>2</sub> (mol)	Carbon (mol)	H <sub>2</sub> (mol)	H <sub>2</sub> O (mol)	CH <sub>4</sub> conversion (%)
1600	0.7639	0.1921	0.0268	0.0003	0.2496	3.89	0.11
1750	0.7542	0.1350	0.0610	0.0016	0.3518	3.86	1.38
1900	0.6962	0.0810	0.0967	0.0054	0.5446	3.81	8.96
1948	0.6571	0.0710	0.1078	0.0073	0.6335	3.80	14.08
2050	0.5424	0.0584	0.1338	0.0126	0.8662	3.75	29.07
2200	0.3453	0.0432	0.1734	0.0234	1.2581	3.69	54.85
Plant data	0.6695	0.0791	0.1084	-	0.6312	3.79	12.46
Error (%)	-1.84	-10.21	-0.54		0.36	0.22	
<b>2. Results by adding Reaction #2 (<math>\text{H}_2\text{O} + \text{C}_2\text{H}_2 = \text{CO} + \text{CH}_4</math>):</b>							
$T_0$ (K)	CH <sub>4</sub> (mol)	C <sub>2</sub> H <sub>4</sub> (mol)	C <sub>2</sub> H <sub>2</sub> (mol)	Carbon (mol)	H <sub>2</sub> (mol)	H <sub>2</sub> O (mol)	CH <sub>4</sub> conversion (%)
1600	0.7640	0.1937	0.0278	0.0003	0.2592	3.89	0.10
1750	0.7564	0.1428	0.0615	0.0014	0.3683	3.86	1.10
1900	0.7158	0.0938	0.0967	0.0044	0.5566	3.82	6.41
1948	0.6887	0.0835	0.1076	0.0059	0.6400	3.80	9.95
2050	0.6056	0.0702	0.1324	0.0096	0.8595	3.76	20.81
2200	0.4463	0.0595	0.1741	0.0165	1.2497	3.71	41.65
Plant data	0.6695	0.0791	0.1084	-	0.6312	3.79	12.46
Error (%)	2.88	5.62	-0.76		1.38	0.34	

In summary, by analyzing the change of amount of relevant components we found another reaction not identified in our previous simulation might have occurred in the pilot plant experiments. Trying the two reactions involving steam and acetylene found from

NIST's website we found that Reaction #2 above fit the pilot plant data very well. Therefore we assume Reaction #2 is the one that must have occurred in the cracker of the pilot plant. Certainly, more sets of real experimental data need to be obtained and run on our simulator to confirm this assumption.

## CHAPTER VI

### CONCLUSIONS AND RECOMMENDATIONS

### FOR FUTURE RESEARCH

Vapor-liquid, liquid-liquid and vapor-liquid-liquid mixtures are three types of important phase equilibria usually seen in chemical engineering research and industrial applications. The calculations of these phase equilibria have important theoretical and practical significance to both thermodynamic researchers and engineers. Equations of state (EOS) combined with proper mixture combining rules (MCR) are often used to calculate the phase equilibrium of a mixture if such EOS and MCR are available for the targeted mixture. However, liquid phases in a mixture are normally very difficult to be described by currently available equations of state. Therefore, activity coefficient models are often used to describe such liquid phases in mixtures and calculate the corresponding phase equilibria.

Saturation Properties for Fluids: Although modern multi-constant equations of state bear good accuracy in describing relatively complicated mixtures, they have the problem of requiring too many constants. For example, to use the Benedict-Webb-Rubin (BWR) EOS to describe a vapor-liquid mixture would require a total of 155 parameters (Barrufet, 1987). To make life easier people tend to use cubic equations of states to describe the VLE as these EOS require only two parameters which are available for a lot of mixture components. However, typical cubic EOS has the limitations of being not accurate enough, especially at high temperature and pressure conditions. Thus, tuning of

these cubic equations of state to higher accuracy can have important implications to their wider applications in the VLE calculations.

In Chapter II we developed a new identity (Eq. II.3)) for the heat of vaporization as an integral of the isochoric slope across the two-phase region between the volume of the saturated liquid and the saturated vapor. The identity is thermodynamic and so can be applied to any EOS. Based on this new identity we have developed improved tuning techniques for several commonly used cubic equations of state, namely the van der Waals EOS, the Redlich-Kwong EOS, the Soave-Redlich-Kwong EOS and the Peng-Robinson EOS.

Four equations (II.14~17) for tuning the constants in the above four EOS are derived by combining the new identity and the respective equation of state. These reasonably simple equations allow one to tune the cubic parameters  $a$  &  $b$  to experimental vapor pressures and heats of vaporization for a set of subcritical isotherms for each pure component. The resultant curves of  $a(T)$  &  $b(T)$  will converge to the usual values of  $a^c$  and  $b^c$  given in Chapter I at the critical temperature. Eqs. II.14~17 should be used with real saturation volumes, preferably from experiment, consistent with the experimental vapor pressures and heats of vaporization with consideration of the Clapeyron identity. When experimental volumes are not available, the procedure given in the section *The Volume Problem* can be used.

In general, this procedure can be applied to any compound found in the property database of Poling et al. (2001) with the addition of at least one other value of the heat of vaporization. Poling et al. provide the heat of vaporization at the normal boiling point (1.01325 bar), critical constants including  $Z_c$ , and the Wagnerian constants  $W_i$  for the

vapor pressure and its slope. For the heat of vaporization, Eq. II.18 is not recommended for use to temperatures as low as the normal boiling point, so we must use Eq. II. 19, which has three constants. However, one can use  $B = \beta' = 0.38 \pm 0.03$  and tune Eq. II.19 to the normal boiling point value from Poling et al. (2001) plus another value at a different temperature. For many reasonably common compounds, compilations such as Majer & Svoboda (1985) and Christensen et al. (1982) provide numerous experimental values for heats of vaporization at temperatures other than the normal boiling point.

The results in Tables (II.1~3) show that the new tuning procedures provide good results with simple cubic EOS such as Redlich-Kwong. They should provide even better results with the Peng-Robinson EOS. This should be further explored in the future. We have shown that these procedures with the Redlich-Kwong EOS provide better results than the Peng-Robinson EOS with conventional procedures. In commercial practice, the Peng-Robinson attraction constant  $a$  is always tuned to the experimental vapor pressures as done in *Case I* in Table II.1. Further tuning of the repulsion constant  $b$  to the experimental heats of vaporization should provide improved results for mixture VLE and distillation design keeping in mind that the saturation volumes will always pose a problem.

Activity Coefficient Models: As mentioned above, simple cubic equations of state are not accurate for describing the liquid phases in a mixture. Instead, various activity coefficient models (excess Gibbs energy models) are normally used to describe liquid solutions. In Chapter III we examined the application of four typical activity coefficient models to the prediction of three phenomena: (1) extremum and inflection points on the popular  $\ln \gamma_i$  vs  $x_1$  diagram for binary solution, (2) liquid-liquid phase

splitting for binary solution, and (3) homogeneous azeotropes. The four models examined here are (a) the symmetric solution model, (b) the two-constant Margules model, (c) the van Laar model, and (d) the three-constant NRTL model.

Prior to this dissertation use of the activity coefficient models to predict the three phenomena listed above require considerable mathematical manipulations which are complicated and time-consuming. For example, to foresee if a phase splitting can occur to a liquid mixture would require one to carry out detailed calculations such as a Gibbs energy minimization. In Chapter III we developed new mathematical procedures to tackle these problems. We first reviewed the symmetric solution model and found that it can be used to predict the above-mentioned phenomena. Then by rationing the two constants in the Margules and van Laar models, we presented a series of graphs which allows one to immediately identify whether the above three phenomena will occur given the value of the two constants. As expected, we were only partially successful with the three-constant NRTL model. Here we provided graphs for phase splitting and equations for extremum and inflection points but found no way to represent the results in a two-dimensional graphical form neither for homogeneous azeotropes nor for extremum and inflection points.

The value of these graphs and equations is that they allow one to quickly and easily see if the phenomena (1)~(3) mentioned above will occur given the value of the constants for a particular liquid solution model. Especially for the last two phenomena is considerable time and effort saved by using these results. For example, why go through a Gibbs energy minimization calculation only to find the liquid does not split since this can be easily done from our graphs? The same can be said for the homogeneous azeotrope. In

both of these examples where the particular phenomena is found to exist, from the results one should then perform the more detailed calculations to see for (2) the composition of the two liquid phases and for (3) the azeotropic composition and pressure.

Remote Natural Gas: Natural gas is playing a more and more important role in meeting the ever increasing energy demand of the world. It is estimated that the total amount of remote natural gas occupies about one-half to two-thirds of all known gas reserves in the world. To convert this huge amount of remote gas into liquid fuels for easy transportation, various technologies and processes have been explored and developed through the years. Chapter IV reviewed the currently available technologies for natural gas conversion to liquid fuels. These technologies can basically be classified into two categories: one is to directly crack natural gas into higher hydrocarbons at high temperatures, and the other is to first convert natural gas to synthesis gas as an intermediate and then convert syngas to the desired final products through catalytic reactions. Following the literature review we explained the methodology to be used for our kinetic simulation of natural gas pyrolysis to liquid fuels. The central idea of this simulation is to establish a proper kinetic model to describe the reaction system under *adiabatic* operating conditions. This includes selection of the reasonable reaction pathway and kinetic rate constants for the reactions, calculation of material and energy balances, optimization of the operating conditions, etc.

There are two major sections in our desired natural gas pyrolysis process – in the first section natural gas is cracked into  $C_2$  hydrocarbons (acetylene & ethylene) at elevated temperatures, and in the second section these  $C_2$  hydrocarbons are converted into higher hydrocarbons (around  $C_5 \sim C_7$ ) via high-selectivity catalysts. Our simulation work

focuses on the reactions in the first section of this process. Chapter V exhibits the simulation results under various feed and reaction conditions. In the first case of lean gas (pure methane) feed, we showed that methane conversion increases with higher reaction temperature and longer residence time. Interesting simulation results were found for methane conversion, ethylene & acetylene production and carbon formation as functions of inlet cracker temperature and residence time. Later we examined the effect of hydrogen dilution to the natural gas feed. Our results confirmed previous findings by other researchers that hydrogen can both inhibit methane decomposition and reduce coke formation. The rich components ( $C_2H_6$ ,  $C_3H_8$  &  $C_4H_{10}$ , etc.) in the natural gas are found to decompose very fast in the cracker and they have a vast quenching effect on the whole reaction system, which means that much higher temperature is required for the rich gas pyrolysis to move on compared with the case of lean gas feed. Following this we reexamined the effect of high temperature on methane conversion by adding a combustion zone with/without steam in the burner prior to the cracker. This again confirms that higher temperature is beneficial to achieving higher methane conversion. Recycling methane from the flue gas to the feed also increases the overall conversion of methane. Finally we entered the original data from a pilot plant to our simulator. With some fine tuning to the simulator we found the results were in very good agreement with those from the pilot plant. This demonstrates that our simulator has reasonably correct coding and thus has the potential to be further improved and commercialized for larger-scale industrial application.

In summary, our results showed that this simulation work is basically successful. However, due to the complicated nature of the natural gas pyrolysis, much more work



needs to be done to find the exact mechanism of such reactions and to obtain the accurate expressions of the kinetic rate constants. Only then can we establish a more accurate kinetic model to describe the pyrolysis process of natural gases and produce much better results for *adiabatic* simulation of both the burner and the cracker.

## LITERATURE CITED

- Aasberg-Petersen, K., J. H. Bak Hansen, T. S. Christensen, I. Dybkjaer, P. Seier Christensen, C. Stub Nielsen, S. E. L. Sinter Madsen and J. R. Rostrup-Nielsen, "Technologies for Large-scale Gas Conversion", *Applied Catalysis A: General*, **221**, 379 (2001).
- Abbott, M. M. and J. M. Prausnitz, "Chapter I: Modeling the Excess Gibbs Energy", *Models for Thermodynamic and Phase Equilibria Calculations*, S. I. Sandler, ed., Marcel Dekker, New York (1994).
- Adachi, Y. and H. Sugie, "Derivative Method to Develop a Cohesion Parameter of a Cubic Equation of State", *J. Chem. Eng. Japan*, **20**, 190 (1987a).
- Adachi, Y. and H. Sugie, "The Controlling Quantity in Cubic Equation of State for Heat of Vaporization Calculation", *J. Chem. Eng. Japan*, **20**, 190 (1987b).
- Alternative Energy, "Non-renewable: Natural Gas", [www.altenergy.org](http://www.altenergy.org) (Accessed June 2003).
- Anderson, R. P., J. R. Fincke and C. E. Taylor, "Conversion of Natural Gas to Liquids via Acetylene as an Intermediate", *Fuel*, **81**, 909 (2002).
- Arnold, K. and M. Stewart, *Surface Production Operations: Design of Gas-Handling Systems and Facilities (Vol. 2)*, 2<sup>nd</sup> ed., Gulf Publishing Co., Houston, TX (1999).
- Aulia, M., *Plasma Process Applications II: Conversion of Methane to Acetylene Using a Plasma Reactor*, Ph.D. Dissertation, Texas A&M University, College Station (2000).
- Barrufet, M. A., "Studies on Criticality Phenomena and Collinearity Constraints", Ph.D. Dissertation, Texas A&M University, College Station (1987).
- Barrufet, M. A. and P. T. Eubank, "Generalized Saturation Properties of Pure Fluids via Cubic Equation of States", *J. Chem. Eng. Ed.*, Summer issue, 168 (1989).
- Bharadwaj, S. S. and L. D. Schmidt, "Catalytic Partial Oxidation of Natural Gas to Syngas", *Fuel Processing Technology*, **42**, 109 (1995).
- Billaud, F. and C. Gueret, "Thermal Decomposition of Pure Methane at 1263 K: Experiments and Mechanistic Modeling", *Thermochimica Acta*, **211**, 303 (1992).
- Bistolfi, M., G. Fornasari, M. Molinari, and S. Palmery, "Kinetic Model for Methane Oxidative Coupling Reactors", *Chem. Eng. Sci.*, **47** (9-I.1), 2647 (1992).
- Christensen, J. J., R. W. Hanks and R. M. Izatt, *Handbook of Heats of Mixing*, John Wiley & Sons, New York (1982).

Collins, C., *Composition of Natural Gases Found Throughout the World*, Undergraduate Research Report, Dept. of Chemical Engineering, Texas A&M University, College Station (2003).

Deiters, U. K., "Calculation of Densities from Cubic Equation of States", *AIChE J.*, **48**, 882 (2002).

Dymond, J. H. and E. B. Smith, *The Virial Coefficient of Pure Gases and Mixtures*, Oxford Univ. Press: Oxford (1980).

Energy Information Administration of DOE, "International Energy Outlook 2003", [www.eia.doe.gov](http://www.eia.doe.gov) (Accessed June 2003).

Eubank, P. T., "A Review of Volumetric, Thermodynamic and Other Physical Properties for Methanol", *Chem. Engr. Sym. Ser.*, **66**(98), 16 (1970).

Eubank, P. T. and M. A. Barrufet, "A Simple Algorithm for Calculation of Phase Separation", *J. Chem. Eng. Ed.*, Winter Issue: 36 (1988).

Eubank, P. T. and K. R. Hall, "An Equal Area Rule and Algorithm for Determining Phase Compositions", *AIChE J.*, **41**, 924 (1995).

Eubank, P. T., B. G. Lamonte and F. F. J. Alvarado, "Consistency Tests for Binary VLE Data", *J. Chem. & Eng. Data*, **45**, 1040 (2000).

Eubank, P. T., G.-S. Shyu and N. S. M. Hanif, "New Procedures for Application of the Wong-Sandler Mixing Rules to the Prediction of Vapor-Liquid Equilibria", *Ind. & Eng. Chem. Res.*, **34**, 314 (1995).

Eubank, P.T. and X. Wang, "Characteristics of Activity Coefficient Models for Liquid Solutions", *AIChE Journal*, in press.

Eubank, P.T. and X. Wang, "Saturation Properties from Equations of State", *Ind. & Eng. Chem. Res.*, **42**(16), 3838 (2003).

Foster, N. R., "Direct Catalytic Oxidation of Methane to Methanol – A Review", *Applied Catalysis*, **19**, 1 (1985).

Fouda, S. A., "Liquid Fuels from Natural Gas", *Scientific American*, **278**, 92 (1998).

Global Technoscan, "INEEL, California Groups Unveil Unique Natural Gas Liquefaction Facility", [www.globaltechnoscan.com](http://www.globaltechnoscan.com) (Accessed in June 2003).

Gmehling, J. and U. Onken, "Vapor Liquid Equilibrium Data Composition: Aqueous-Organic Systems", *DECHEMA Data Series*, **1**(1): 1 (1990).

Goodwin, R. D., "Benzene Thermophysical Properties from 279 to 900 K at Pressures to 1000 Bar", *J. Phys. & Chem. Ref. Data*, **17**, 1541 (1988).

Gulyaev., G. V. and L. S. Polak, "The Kinetics of the Thermal Decomposition of Methane", Institute of Petrochemical Synthesis, Academy of Sciences, USSR, **6**, 352 (1965).

Hall, K. R. and P. T. Eubank, "Empirical Description of Liquid-Vapor Critical Region Based upon Coexistence Data", *Ind. Eng. Chem. Fundam.*, **15**, 323 (1976).

Hernandez-Garduza, O., F. Garcia-Sanchez, D. Apam-Martinez and R. Vazquez-Roman, "Vapor Pressures of Pure Compounds Using the Peng-Robinson Equation of State with Three Different Attractive Terms", *Fluid Phase Equil.*, **198**, 195 (2002).

Hidaka, Y., T. Nakamura, H. Tanaka, K. Inami and H. Kawano, "High Temperature Pyrolysis of Methane in Shock Waves. Rates for Dissociative Recombination Reactions of Methyl Radicals and for Propyne Formation Reaction", *Intl. J. of Chem. Kinet.*, **22**, 701 (1990).

Hidaka, Y., K. Sato, Y. Henmi, H. Tanaka and K. Inami, "Shock-tube and Modeling Study of Methane Pyrolysis and Oxidation", *Combustion and Flame*, **118**, 340 (1999).

Holmen A., O. Olsvik, and O. A. Rokstad, "Pyrolysis of Natural Gas: Chemistry and Process Concepts", *Fuel Processing Technology*, **42**, 249 (1995).

Holmen, A., O. A. Rokstad and A. Solbakken, "High-Temperature Pyrolysis of Hydrocarbons. 1. Methane to Acetylene", *Ind. Eng. Chem., Proc. Des. Dev.*, **15** (3), 439 (1976).

Huff, G. A., and I. A. Vasalos, "Oxidative Pyrolysis of Natural Gas in a Spouted-bed Reactor: Reaction Stoichiometry and Experimental Reactor Design", *Catalysis Today*, **46**, 223 (1998).

Kennedy, J. L., *Oil and Gas Pipeline Fundamentals*, 2<sup>nd</sup> ed., PennWell Publishing Co., Tulsa, OK (1993).

Khoshnoodi, M. and Y. S. Lim, , "Simulation of Partial Oxidation of Natural Gas to Synthesis Gas Using ASPEN PLUS", *Fuel Processing Technology*, **50**, 275 (1997).

Kozlov, G. I. and V. G. Knorre, "Single-pulse Shock Tube Studies on the Kinetics of the Thermal Decomposition of Methane", Institute of Energetics, USSR, **6**, 253 (1962).

Kruggel-Emden, H., *The Accuracy of Fugacities, Enthalpies and Compressibility Factors of Truncated Virial Equations of State for Steam*, Research Report: Dept. of Chemical Engineering, Texas A&M University, College Station (2002).

Kumar, S., *Gas Production Engineering*, Gulf Publishing Co., Houston, TX (1987).

Kunugi, T., T. Tamura and T. Naito, "New Acetylene Process Uses Hydrogen Dilution", *Chem. Eng. Progress*, **57** (11), 43 (1961)

Li, L., R. W. Borry, and E. Iglesia, "Reaction-transport Simulation of Non-oxidative Methane Conversion with Continuous Hydrogen Removal – Homogeneous-heterogeneous Reaction Pathways", *Chem. Eng. Sci.*, **56**, 1869 (2001).

Majer, V. and V. Svoboda, "Enthalpies of Vaporization of Organic Compounds", *IUPAC Chem. Data Series 32*, Blackwell Scientific Pub., Oxford (1985).

Miller, J. A. and C. F. Melius, "A Theoretical Analysis of the Reaction between Hydroxyl and Acetylene", *Symp. Int. Combust. Proc.*, **22**, 1031 (1989).

Mossaad, E., *Kinetic Simulation and Heat Transfer Coefficient Estimation for Natural Gas Conversion to C<sub>2</sub> Hydrocarbons*, Ph.D. Dissertation, Texas A&M University, College Station (2002).

Okumoto, M. and A. Mizuno, "Conversion of Methane for Higher Hydrocarbon Fuel Synthesis Using Pulsed Discharge Plasma Method", *Catalysis Today*, **71**, 211 (2001).

Palmer, H. B., J. Lahaye, K. C. Hou, "On the Kinetics and Mechanism of the Thermal Decomposition of Methane in a Flow System", *J. Phys. Chem.*, **72** (1), 348 (1968).

Parkyns, N. D., C. L. Warburton and J. D. Wilson, , "Natural Gas Conversion to Liquid Fuels and Chemicals: Where Does It Stand?", *Catalysis Today*, **18**, 385 (1993).

Periana, R. A., D. J. Taube, S. Gamble, H. Taube, H. Fuji, "A New Method for Converting Methane to Methanol", in E.G. Derouane et al. (eds.), *Catalytic Activation and Functionalization of Light Alkanes*, Kluwer Academic Publishers, Dordrecht, The Netherlands (1998).

Poling, B. E., J. M. Prausnitz, and J. P. O'Connell, *The Properties of Gases and Liquids*, 5<sup>th</sup> Ed., McGraw-Hill, New York (2001).

Prausnitz, J. M., R. N. Lichtenhaler and E. Gomes de Azevedo, *Molecular Thermodynamics of Fluid-Phase Equilibria*, 3<sup>rd</sup> ed., Prentice Hall, Upper Saddle River, NJ (1999).

Quinlan, M., "Gas-to-liquids Processes Approaching Commercial Viability", *Petroleum Economist*, **64**, 18 (1997).

Rackett, H. G., "Equation of State for Saturated Liquids", *J. Chem. Eng. Data*, **15**, 514 (1970).

Reimesme, G., J. Saint-Just and Y. Muller, "Transportation Fuels and Chemicals Directly from Natural Gas : How Expensive ?", *Catalysis Today*, **13**, 371 (1992).

Renon, H. and J.M. Prausnitz, "Estimation of Parameters for the NRTL Equation for Excess Gibbs Energies of Strongly Nonideal Liquid Mixtures", *I&EC Proc. Des. & Dev.*, **8**, 413 (1969).

Rostrup-Nielsen, J. R., I. Dybkjaer, K. Aasberg-Petersen, "Natural Gas Conversion via Low-temperature Fischer-Tropsch Process", *Petr. Chem. Div.*, **45**, 186 (2000).

Rowlinson, J. S. and F.L. Swinton, *Liquids and Liquid Mixtures*, 3<sup>rd</sup> ed., Butterworths, London (1982).

Salim, P. H, and M. A. Trebble, "A Modified Trebble-Bishnoi Equation of State: Thermodynamic Consistency Revisited", *Fluid Phase Equil.*, **65**, 59 (1991).

Sandler, S. I., *Chemical and Engineering Thermodynamics*, 3<sup>rd</sup> Ed., John Wiley & Sons, New York (1999).

Satterfield, C. N., *Heterogeneous Catalysis in Industrial Practice.*, McGraw-Hill, New York (1991).

Setzmann, U. W. and W. Wagner, "A New Equation of State and Tables of Thermodynamic Properties for Methane Covering the Range from the Melting Line to 625 K at Pressures up to 100 MPa", *J. Phys. & Chem. Ref. Data*, **20**, 1061 (1991).

Smith, J. M., H. C. Van Ness and M. M. Abbott, *Chemical Engineering Thermodynamics*, 6<sup>th</sup> Ed., McGraw-Hill, New York (2001).

Sokolnikoff, I. S. and E. S. Sokolnikoff, *Higher Mathematics for Engineers and Physicists*, 2<sup>nd</sup> Ed., McGraw-Hill, New York (1941).

Stiegel, G. J. and R. D. Srivastava, "Natural Gas Conversion Technologies", *Chemistry and Industry*, **21**, 854 (1994).

Stryjek, R. and J. H. Vera, "An Improved Peng-Robinson Equation of State for Pure Compounds and Mixtures", *Can. J. Chem. Eng.*, **64**, 323 (1986).

Synfuels International, Inc., "Markets: The Challenge", [www.synfuels.com](http://www.synfuels.com) (Accessed June 2003).

Tester, J. W. and M. Modell, *Thermodynamics and Its Applications*, 3<sup>rd</sup> ed., Prentice Hall, Upper Saddle River, NJ (1996).

TRC *Thermodynamic Tables* – Thermodynamics Research Center, Texas A&M University, College Station (1982).

Twigg, M. V. (ed.), *Catalyst Handbook*, Wolfe Publishing Ltd., London (1989).

Van der Zwet, G. P., P. A. J. M. Hendriks and R. A. Van Santen, "Pyrolysis of Methane and the Role of Surface Area", *Catalysis Today*, **4**, 365 (1989).

Van Konynenburg, P. H., *Critical Lines and Phase Equilibria in Binary Mixtures*, Ph.D. dissertation, UCLA, Los Angeles, CA (1968).

Vuddagiri, S. R. and P. T. Eubank, "The Condensation of Mixed Vapors and Thermodynamics", *AIChE J.*, **44**, 2526 (1998).

Wollan, J. J., G. W. Swift, S. Bachhaus and D. L. Gardner, "Development of a Thermoacoustic Natural Gas Liquefier", AIChE New Orleans, LA Meeting (April 2002).

Yang, W., H. Xiang, Y. Li and Y. Sun, "Micro-kinetic Analysis and Monte Carlo Simulation in Methane Partial Oxidation into Synthesis Gas", *Catalysis Today*, **61**, 237 (2000).

Yao, S., A. Nakayama and E. Suzuki, "Acetylene and Hydrogen from Pulsed Plasma Conversion of Methane", *Catalysis Today*, **71**, 219 (2001).

## VITA

Xiaonian Wang was born to Mingze Wang and Quanying Zhang in Jiangxi, China on March 2, 1970. He entered Zhejiang University in September 1988 and graduated with a B.S. in chemical engineering in July 1992. He then worked for Sinopec Beijing Design Institute as a chemical process engineer until December 1994. Starting January 1995, he joined Shell (China) Limited and worked as a project engineer until July 2000. In the fall of 2000 he enrolled in the doctorate program in chemical engineering of Texas A&M University, and received his Ph.D. in May 2004.

The permanent address for Mr. Xiaonian Wang is:

Rm. 1034, Bldg. 10, Shi You Da Yuan,  
20 Xue Yuan Lu, Haidian District,  
Beijing, China 100083